**Atmospheric
Chemistry
and Physics
Discussions**

Radiative forcing in the ACCMIP historical and future climate simulations

D. T. Shindell[1], J.-F. Lamarque[2], M. Schulz[3], M. Flanner[4], C. Jiao[4], M. Chin[5],
P. Young[6], Y. H. Lee[1], L. Rotstayn[7], G. Milly[1], G. Faluvegi[1], Y. Balkanski[8],
W. J. Collins[9], A. J. Conley[2], S. Dalsoren[10], R. Easter[11], S. Ghan[11], L. Horowitz[12],
X. Liu[11], G. Myhre[10], T. Nagashima[13], V. Naik[14], S. Rumbold[9], R. Skeie[10],
K. Sudo[15], S. Szopa[8], T. Takemura[16], A. Voulgarakis[1, 17], and J.-H. Yoon[11]

[1]NASA Goddard Institute for Space Studies and Columbia Earth Institute, New York, NY, USA
[2]National Center for Atmospheric Research (NCAR), Boulder, CO, USA
[3]Meteorologisk Institutt, Oslo, Norway
[4]Department of Atmospheric, Oceanic and Space Sciences, University of Michigan, Ann Arbor, MI, USA
[5]NASA Goddard Space Flight Center, Greenbelt, MD, USA
[6]Cooperative Institute for Research in Environmental Sciences, University of Colorado and NOAA Earth System Research Laboratory, Boulder, Colorado, USA
[7]Centre for Australian Weather and Climate Research, CSIRO Marine and Atmospheric Research, Aspendale, Vic, Australia
[8]Laboratoire des Sciences du Climat et de l'Environnement LSCE-IPSL, France
[9]Met Office, Hadley Centre, Exeter, UK
[10]Center for International Climate and Environmental Research Oslo (CICERO), Oslo, Norway

ACPD

12, 21105–21210, 2012

Radiative forcing in the ACCMIP

D. T. Shindell et al.

Title Page

Abstract	Introduction
Conclusions	References
Tables	Figures

◄ ►

◄ ►

Back Close

Full Screen / Esc

Printer-friendly Version

Interactive Discussion

[11]Pacific Northwest National Laboratory, Richland, WA, USA
[12]NOAA Geophysical Fluid Dynamics Laboratory, Princeton, NJ, USA
[13]National Institute for Environmental Studies, Tsukuba-shi, Ibaraki, Japan
[14]UCAR/NOAA Geophysical Fluid Dynamics Laboratory, Princeton, NJ, USA
[15]Department of Earth and Environmental Science, Graduate School of Environmental Studies, Nagoya University, Nagoya, Aichi, Japan
[16]Research Institute for Applied Mechanics, Kyushu University, Fukuoka, Japan
[17]Department of Physics, Imperial College London, London, UK

Correspondence to: D. T. Shindell (drew.t.shindell@nasa.gov)

Title Page

Abstract | Introduction

Conclusions | References

Tables | Figures

◄ | ►

◄ | ►

Back | Close

Full Screen / Esc

Printer-friendly Version

Interactive Discussion

Abstract

A primary goal of the Atmospheric Chemistry and Climate Model Intercomparison Project (ACCMIP) was to characterize the short-lived drivers of preindustrial to 2100 climate change in the current generation of climate models. Here we evaluate historical
5   and future radiative forcing in the 10 ACCMIP models that included aerosols, 8 of which also participated in the Coupled Model Intercomparison Project phase 5 (CMIP5).

The models generally reproduce present-day climatological total aerosol optical depth (AOD) relatively well. They have quite different contributions from various aerosol components to this total, however, and most appear to underestimate AOD over East
10   Asia. The models generally capture 1980–2000 AOD trends fairly well, though they underpredict AOD increases over the Yellow/Eastern Sea. They appear to strongly underestimate absorbing AOD, especially in East Asia, South and Southeast Asia, South America and Southern Hemisphere Africa.

We examined both the conventional direct radiative forcing at the tropopause (RF)
15   and the forcing including rapid adjustments (adjusted forcing; AF, including direct and indirect effects). The models' calculated all aerosol all-sky 1850 to 2000 global mean annual average RF ranges from -0.06 to $-0.49\,\mathrm{W\,m^{-2}}$, with a mean of $-0.26\,\mathrm{W\,m^{-2}}$ and a median of $-0.27\,\mathrm{W\,m^{-2}}$. Adjusting for missing aerosol components in some models brings the range to -0.12 to $-0.62\,\mathrm{W\,m^{-2}}$, with a mean of $-0.39\,\mathrm{W\,m^{-2}}$. Screen-
20   ing the models based on their ability to capture spatial patterns and magnitudes of AOD and AOD trends yields a quality-controlled mean of $-0.42\,\mathrm{W\,m^{-2}}$ and range of -0.33 to $-0.50\,\mathrm{W\,m^{-2}}$ (accounting for missing components). The CMIP5 subset of AC-CMIP models spans -0.06 to $-0.49\,\mathrm{W\,m^{-2}}$, suggesting some CMIP5 simulations likely have too little aerosol RF. A substantial, but not well quantified, contribution to histori-
25   cal aerosol RF may come from climate feedbacks (35 to -58%). The mean aerosol AF during this period is $-1.12\,\mathrm{W\,m^{-2}}$ (median value $-1.16\,\mathrm{W\,m^{-2}}$, range -0.72 to $-1.44\,\mathrm{W\,m^{-2}}$), indicating that adjustments to aerosols, which include cloud, water vapor and temperature, lead to stronger forcing than the aerosol direct RF. Both negative

aerosol RF and AF are greatest over and near Europe, South and East Asia and North America during 1850 to 2000. AF, however, is positive over both polar regions, the Sahara, and the Karakoram. Annual average AF is stronger than 0.5 W m^{-2} over parts of the Arctic and more than 1.5 W m^{-2} during boreal summer. Examination of the regional
5 pattern of RF and AF shows that the multi-model spread relative to the mean of AF is typically the same or smaller than that for RF over areas with substantial forcing.

Historical aerosol RF peaks in nearly all models around 1980, declining thereafter. Aerosol RF declines greatly in most models over the 21st century and is only weakly sensitive to the particular Representative Concentration Pathway (RCP). One model,
10 however, shows approximate stabilization at current RF levels under RCP 8.5, while two others show increasingly negative RF due to the influence of nitrate aerosols (which are not included in most models). Aerosol AF, in contrast, continues to become more negative during 1980 to 2000 despite the turnaround in RF. Total anthropogenic composition forcing (RF due to well-mixed greenhouse gases (WMGHGs) and ozone plus
15 aerosol AF) shows substantial masking of greenhouse forcing by aerosols towards the end of the 20th century and in the early 21st century at the global scale. Regionally, net forcing is negative over most industrialized and biomass burning regions through 1980, but remains strongly negative only over East and Southeast Asia by 2000 and only over a very small part of Southeast Asia by 2030 (under RCP8.5). Net forcing
20 is strongly positive by 1980 over the Sahara, Arabian peninsula, the Arctic, Southern Hemisphere South America, Australia and most of the oceans. Both the magnitude of and area covered by positive forcing expand steadily thereafter.

There is no clear relationship between aerosol AF and climate sensitivity in the CMIP5 subset of ACCMIP models. There is a clear link between the strength of
25 aerosol+ozone forcing and the global mean historical climate response to anthropogenic non-WMGHG forcing (ANWF). The models show ~20–35 % greater climate sensitivity to ANWF than to WMGHG forcing, at least in part due to geographic differences in climate sensitivity. These lead to ~50 % more warming in the Northern Hemisphere in response to increasing WMGHGs. This interhemispheric asymmetry is

enhanced for ANWF by an additional 10–30 %. At smaller spatial scales, response to ANWF and WMGHGs show distinct differences.

1   Introduction

While well-mixed greenhouse gases are the largest single driver of climate change
since the preindustrial, aerosols and ozone are also important contributors. They are also distributed unevenly in the atmosphere, and their distinct patterns of radiative forcing (RF) contribute to the regional pattern of climate change. Despite their clear importance, large-scale model intercomparisons of climate have traditionally neglected to characterize the temporal and spatial evolution of aerosol and ozone forcing.
   For example, the simulations performed for the Climate Model Intercomparison Project (CMIP) phase 3 activity in support of the IPCC AR4 provided a tremendously useful resource for exploring issues of climate sensitivity, historical climate and climate projections. However, the CMIP3 archive does not include diagnostics of radiative forcing from aerosols or ozone. This is important since the radiative forcings imposed in
both the simulations of the 20th century and the future projections varied from model to model due to varying assumptions about emissions, differences in the behavior of physical processes affecting short-lived species that were included, and differences in which processes and constituents were included at all (e.g. only 8 of 23 CMIP3 models included black carbon (BC) while less than half included future tropospheric ozone
changes). Hence it is not straightforward to understand how much of the variation between simulated climate in the models results from internal climate sensitivity and how much results from differences in the forcings.
   The CMIP5 project (Taylor et al., 2012) similarly will have little information on radiative forcing by aerosols or by ozone. As models progress to a more Earth System
approach including more interactions with the biosphere, a larger number of climate-sensitive emissions are also being incorporated into models, which leads to diversity in the projected emissions even though anthropogenic emissions should be quite uniform

across models. Hence there is a need for characterization of the forcings imposed in the CMIP5 historical and future simulations, and for diagnostics to allow us to understand the causes of the differences in forcings from model to model. ACCMIP attempts to meet these various needs through a set of coordinated simulations, diagnostics and evaluations against observations (Lamarque et al., 2012b). Here we present a description of the ACCMIP models' aerosol simulations, including an evaluation of simulated optical properties against a variety of observations and a description of the resulting radiative forcing. We then combine the aerosol forcings with ACCMIP analyses of ozone and well-mixed greenhouse gas (WMGHG) forcing to provide estimates of the total anthropogenic forcing through time.

2 ACCMIP model descriptions and experimental design

A large number of models participated in the ACCMIP. While intended primarily to provide understanding of the anthropogenic drivers of climate change in CMIP5, ACCMIP was open to the wider modeling community, and several groups participated that were not also participants in CMIP5. We include both types of models, providing analyses of the CMIP5 subset of ACCMIP models when appropriate. As here we focus on aerosols, we include only those ACCMIP models that provided aerosol simulations (some models provided only gas-phase diagnostics). Some of the key information about the aerosols included in the models and the experiments performed is presented in Table 1. More detailed information on each model can be found in the ACCMIP overview paper of Lamarque et al. (2012b). We note that the GISS-E2-R-TOMAS and NCAR-CAM5.1 models include representations of aerosol sizes, while all other models use a bulk approach in which the size distribution is prescribed and only aerosol mass is computed.

All models used time-varying anthropogenic and biomass burning emissions of aerosol and tropospheric ozone precursors from Lamarque et al. (2010) for the historical period. Future anthropogenic and biomass burning emissions were created by four separate integrated assessment modeling (IAM) groups aiming to provide emissions

that would lead to a prescribed amount radiative forcing in 2100 relative to 1850. The scenarios are called "representative concentration pathways" (RCPs) and are named by their nominal 2100 forcing relative to 1750: RCP2.6, 4.5, 6.0 and 8.5 (van Vuuren et al., 2011). However, emissions were modified in two models, with GISS-E2-R scaling the biomass burning emissions of BC and organic aerosol (OA) by 1.4, and CSIRO-Mk3.6 scaling all BC by 1.25 and all OA by 1.5. Natural emissions varied across the models, and in many cases varied as climate changed. Further information on how emissions were implemented in each model can be found in Lamarque et al. (2012b). Concentrations of well-mixed greenhouse gases (CO_2, CH_4, N_2O and halocarbons) were prescribed according to the RCP projections which are based on calculations with the reduced-complexity coupled carbon cycle climate model MAGICC 6.3 to estimate mixing ratios that would result from the IAM RCP emissions (Meinshausen et al., 2011).

ACCMIP simulations were typically performed as timeslices using emissions from a particular point in time, prescribed SSTs and sea-ice from CMIP5 simulations driven by the same forcings, and free-running atmospheric models. All models included changes in the ocean, and hence meteorology, except NCAR-CAM5.1, CICERO-OsloCTM2 and CSIRO-Mk3.6. Several historical and future times were selected (Table 1). The exceptions to this are the simulations with the GISS-E2-R model, for which the CMIP5 runs included interactive chemistry and aerosols and hence the ACCMIP diagnostics were saved directly from the CMIP5 transient simulations, and the LMDzORINCA which also archived many diagnostics from transient simulations (Szopa et al., 2012). Values in all analyses are averaged over the available years of the timeslice (generally 5–10 years), or in the GISS-E2-R and LMDzORINCA cases the 11 years centered on the timeslice (except for 1850, for which 1850-1859 was used), and are area-weighted for global or regional means.

The ACCMIP simulations from all models thus include both the effects of changing emissions and changing climate. These include not only the impacts of climate change on aerosols of primarily anthropogenic origin via processes such as altered wet or

dry removal or oxidation, but also changes in both emissions and lifetimes of dust and sea-salt aerosols in many of the models (Table 1). In order to separate these, additional simulations with fixed climate but altered emissions, or vice-versa, were also performed. In these simulations, "climate conditions" refers to sea surface temperatures

5   and sea-ice cover and concentrations of WMGHGs. These were maintained at 1850 while anthropogenic and biomass burning emissions were set to various future time periods, for example. This analysis also allows us to clearly separate out the influence of climate changes, which affect not only anthropogenic aerosols but in some models also dust and sea-salt aerosols. We nonetheless include any changes in those natural

10 aerosols in our aerosol forcing estimates when they were included in the groups' CMIP5 simulations.

3   Evaluation of present-day aerosols

The most comprehensive and highest quality data has become available in the past decade, so we begin by evaluating the present-day aerosol climatology. We use the

15 ACCMIP 2000 timeslice as the nearest in time to most available datasets.

Radiative forcing is the end result of a path from emissions to concentrations to aerosol optical properties to forcing. As RF is not directly observed, we examine the earlier stages, presenting emissions and burdens but primarily focusing on aerosol optical depth (AOD) as the nearest observed quantity to RF. Analysis of BC surface

20 concentrations in the ACCMIP models is presented elsewhere (Lee et al., 2012).

3.1   Satellite AOD

Many aspects of the geographic and temporal variability of aerosols could be analyzed. We start by examining the spatial distribution of annual mean AOD in the models. We compare the models with observations from the MODIS and MISR satellite instruments

25 averaged over 2004–2006. We note that there may be slight differences geographically

Full Screen / Esc

Printer-friendly Version

Interactive Discussion

Printer-friendly Version

Interactive Discussion

between the year 2000 and the 2004–2006 period, but as the emissions are meant to represent mean conditions around 2000 changes should be fairly small. Though the ACCMIP experiment protocol did not request separate all-sky and clear-sky AOD diagnostics, these were available from a few models, and hence both were analyzed,

5 though we concentrate on clear-sky model output when both are available since that is more comparable to observations.

The multi-model mean of the 10 ACCMIP models providing AOD clearly captures many of the broad features seen in the satellite measurements (Fig. 1). High aerosol loadings over desert regions in and near Africa, the Arabian Peninsula and central

10 Asia associated with mineral dust stand out in both models and observations, as does the band of locally enhanced AOD over the Southern Ocean associated with sea-salt. Areas with large amounts of anthropogenic aerosol emissions also stand out as having high AOD, especially those over East Asia and the Indo-Gangetic plain. The multi-model mean appears to underestimate both the magnitude and extent of AOD in these

15 areas, however. Similarly, AOD in tropical South America, Africa and Indonesia, where biomass burning emissions are large, appears to be underpredicted.

While the multi-model mean is consistent with measurements in having broadly lower AOD levels in Europe and North America than in developing Asia, it shows a local maximum over the Balkans that is not seen in observations, while failing to reproduce the

20 local maximum observed over the Po Valley. The multi-model mean does not capture local maxima seen by MODIS over the Valley of Mexico or the Mojave Desert either, though these are not recorded by MISR. Over Australia, the multi-model mean is similar to MISR, and does not show the extreme lows or highs seen by MODIS. The model also underpredicts AOD over Arctic land areas and over the Southern Ocean.

25 We performed quantitative comparisons between the models and the satellite data, evaluating spatial correlations and biases. For these analyses, all calculations use re-gridded 1° × 1° annual mean fields and the models are sampled only where the satellite instruments report observations. We examined both the all-sky and clear-sky model output (Table 2). Differences are generally fairly small for the CSIRO-Mk3.6 and GISS-

E2-R-TOMAS models, but are quite large for GISS-E2-R. In this case, large positive biases versus observations were found when using all-sky AODs which are replaced by small negative biases using clear-sky values. The incorporation of large aerosol water uptake in cloudy regions, which causes strong non-linearities in optical properties at

5 very high relative humidity (RH) values, seems to have a large influence on the all-sky values in this model. In support of this hypothesis, we note that GISS-E2-R all-sky are much larger than clear-sky values for sulfate, moderately larger for sea-salt and nitrate, and quite similar for other components, and hence follow the relative solubility of the different species. GISS-E2-R calculates clear-sky AOD by including only AOD values

10 calculated in model locations where clouds are not present, rather than performing a global calculation with clouds removed from the model. This technique is more comparable to the sampling of the satellites, but leads to spatial and temporal differences in sampling compared with all-sky calculations in addition to the role of the clouds themselves. It appears that in GISS-E2-R, there is in general substantially more AOD when

15 and where clouds are present. In contrast, for CSIRO-Mk3.6, AOD is less where clouds are present. Several competing factors are at work, including increased wet removal rates and cloud scavenging in cloudy areas leading to lower AOD but increased in-cloud oxidation rates and RF in cloudy areas leading to higher AOD, so it is perhaps not surprising that clear-sky versus all-sky differences can be of either sign. For other

20 models, HadGEM2 reports that its AOD is clear-sky, MIROC-CHEM reports that all-sky RH is used but that AOD is not much different for clear-sky, CICERO-OsloCTM2 reports all-sky but notes that it doesn't make much difference. In addition to the issue of sampling that could bias RH if all-sky rather than only clear-sky areas are sampled, the RH used in calculation of water uptake is also important and diverges between models.

25 For example, LMDzORINCA uses the clear-sky humidity to compute aerosol growth, while NCAR-CAM5.1 reports that all-sky grid cell mean RH is used.

Correlations between the models and the two satellite datasets are generally similar. The models show a substantial diversity in their ability to capture the observed spatial distribution of AOD. Biases also show a large spread, with values versus MODIS or

MISR ranging between 30 % underestimates to 30 % overestimates, with the majority of models being too low.

A portion of the negative bias seen in comparison with observations in many models is likely due to the models not including some components, especially nitrate and SOA. We compare global mean AOD in the models both based on the aerosol represented by each model and based on adjustment to account for the missing components (for which mean AODs from the other models were added; Fig. 2). Inclusion of missing components improves model agreement with observed global mean total AOD in most cases, though not always. Mean absolute value biases decrease from their 19–20 % range without adjustment to 15–16 % with adjustments.

Though global mean total AOD biases in the models tend to be ∼0.03 or less (within 20 % of the observations), models find a realistic total AOD with a very diverse partitioning among the various aerosol types (Fig. 3). Both the absolute AOD and the fraction of the total contributed by primarily natural dust and sea-salt vary by more than a factor of 2 across models. Primarily anthropogenic aerosols show similarly large variations, with AOD from individual components varying by as much as a factor of 4 across models, despite having nearly identical sources in most models.

Unfortunately, satellite observations cannot readily distinguish between different aerosol types. However, a MODIS data product for the fine-mode fraction is available (Remer et al., 2005). We compare that product with the modeled sum of all aerosols except sea-salt and dust, as these are predominantly large particles. Researchers have attempted to remove the dust and sea-salt components from the MODIS fine mode product to evaluate the anthropogenic portion of the total AOD over the oceans, but there is considerable uncertainty associated with separating out small particles of sea-salt, smoke and mineral dust and thus far no consensus on an observationally-constrained anthropogenic AOD (Bellouin et al., 2008; Yu et al., 2009).

Models should therefore be biased low as some of the sea-salt and dust particles are small and are included in the MODIS fine mode product. Over the oceans, this is the case for all models except GFDL-AM3 and NCAR-CAM5.1, though the magnitude of

the low bias varies greatly between models (Table 3). Spatial correlations are fairly consistent across all models except MIROC-CHEM and NCAR CAM5.1, for which they are quite low. Looking at the entire globe, half the models now show positive biases, and correlations are generally poor. However, the MODIS fine mode product itself shows

5 abrupt changes across coastlines that seem unphysical. Hence we place greater value on the comparison over ocean regions, where MODIS data is more reliable.

To obtain some idea of how well the models do in representing aerosols of different types, we perform an analysis where locations in each model are sorted according to the dominant mass type (as in Lee and Adams, 2010) and then compared against ob-

10 served annual AODs (Table 4). Note that the locations with dominant mass type are different from model to model. We evaluate biases, log-mean normalized bias defined as the sum of the log (base 10) of the modeled to observed AOD ratio at each point divided by the number of points, and the log-mean normalized error defined similarly except using the absolute value of the ratio log. Looking at the top decile (10 %) of

15 sulfate mass density, AOD has moderate positive biases in CICERO-OsloCTM2 and GFDL-AM3, and a moderate negative bias in MIROC-CHEM. Some models have comparable magnitude biases against one satellite dataset, but little bias against the other (GISS-E2-R-TOMAS, NCAR-CAM5.1). Examining global mean sulfate AOD, indeed CICERO-OsloCTM2 and GFDL-AM3 have values substantially higher than any of the

20 other models, but the other models' totals do not correspond closely to their biases in sulfate-rich areas. In particular, the GISS-E2-R-TOMAS model is among the lowest for global mean sulfate AOD despite its positive biases in sulfate-rich areas versus MISR, while MIROC-CHEM is mid-range in global mean despite it's negative bias.

In OA-rich locations, several models appear to have too little AOD (NCAR-CAM3.5,

25 NCAR-CAM5.1, MIROC-CHEM and GISS-E2-R) while GFDL-AM3 appears to have too much. Biases in OA-rich areas have no clear relationship to global mean OA AOD values other than GFDL-AM3 having the largest OA AOD. Dust and sea-salt are primarily naturally occurring aerosols, and thus their absolute amount tells us little about their contribution to forcing. In areas with high dust loading, the GISS-E2-R-TOMAS model

overestimates AOD (and has the highest global mean dust AOD by far), while MIROC-CHEM underestimates. The latter may be part of the reason that model has the lowest global mean AOD of any of the models in ACCMIP (though it is only marginally lower than some others). Note that differences in model/observations AOD comparisons between the two satellite datasets are particularly large for dusty areas as MODIS provides little coverage in most desert regions (Fig. 1). The AOD in sea-salt rich regions tends to be fairly well simulated, though there are moderate positive biases in NCAR-CAM5.1 and CICERO-OsloCTM2 and negative biases in NCAR-CAM3.5. Sea-salt biases do correspond fairly well with global mean sea-salt AOD values.

3.2 AeroNet AOD

The most quantitatively reliable large-scale network of AOD observations stems from AeroNet sun photometers. We compare the year 2000 model simulations with a monthly Aeronet climatology spanning 2000–2009. This climatology is based on measurements from 388 stations located below 1000 m in altitude, though coverage is largely limited to continental areas (other than a few island stations) and is quite sparse in some areas. Comparisons are made only in months with data available (roughly 10 months per year on average).

Correlations are calculated against all the AeroNet data, and thus reflect the models' ability to capture both the spatial pattern of AOD and its seasonal cycle. Values range from 0.44 to 0.69 for the ACCMIP models (Table 2). For comparison, the Aero-Com phase I models had correlations with AeroNet ranging from about 0.29 to 0.77, with 6 of the 7 model having values between 0.52 and 0.77 (Textor et al., 2006). The AeroCom phase II models, using meteorology nudged to observations, report correlations from about 0.26 to 0.78, with 8 of the 10 models having values between 0.60 and 0.78 (Schulz et al., 2012). In the ACCMIP set, 7 of the 9 models have correlations between 0.54 and 0.69. The slightly lower correlations seen in the ACCMIP models relative to the 8 best AeroCom phase II models could reflect either the use of meteorological reanalyses in AeroCom rather than free-running models in ACCMIP, or the use

of somewhat less sophisticated aerosol models in the CMIP5 GCMs in some cases, the use of daily data in AeroCom as opposed to monthly mean data in ACCMIP, or a combination of these factors. Biases in the models tend to be smaller with respect to AeroNet than in comparison with satellite datasets, perhaps indicating that primarily anthropogenic aerosols over land are better simulated than aerosols over remote oceans, or indicating there are remaining biases in the satellite data. Overall, evaluation against ground-based and satellite datasets is fairly consistent, however.

Looking regionally, we find that the spatial correlations in the models are highest for North Africa (0.46–0.80), with North America second (0.48–0.67 in all but one model). Spatial correlations vary widely across models for East Asia (0.09–0.57), but are consistently low over Europe (0.31–0.45 in all but one model). The models all do a generally good job of capturing the seasonal cycle of AOD in all continental-sized regions, with nearly all correlations between 0.6 and 0.8. There is no relationship between the quality of the seasonality in the models and the quality of the spatial structure, however.

Biases in the models tend to be comparatively small over North Africa, Europe and North America in most of the models (Fig. 4). Nearly all models show large negative biases over East Asia, however. Interestingly, the two models that do not show a large negative bias over East Asia show the largest positive biases over both Europe and North America. Similarly, root-mean-square differences relative to AeroNet are typically fairly small for Europe and North America, and substantially larger for North Africa and especially East Asia. This indicates that the models have difficulty capturing the spatial distribution of AOD within those regions as well as the overall negative bias over East Asia. Biases over remote island stations in the central Pacific and Indian Oceans, over the southern tip of South America, and over Australia and New Zealand are nearly always positive (Fig. 5). In contrast, biases over the Russian and especially the Western Hemisphere Arctic are typically negative.

Examining the zonal mean AOD by component (Fig. 6), we see that sulfate is the largest contributor to AOD in much of the NH mid-latitudes in all models except NCAR-CAM5.1. Dust AOD peaks around 20° N in most models, and the largest dust

contribution is in HadGEM2 and GISS-E2-R-TOMAS (the breadth and magnitude of the peak). The GISS-E2-R-TOMAS model's dust AOD is in fact larger than the total observed AOD around 15° N, indicating that there is too much dust in that model and accounting for the positive bias in North African total AOD (Fig. 4; though that model actually has the highest spatial correlation with AeroNet in that region). This positive bias in dust is consistent with the analysis against satellites in dust-rich regions as well (Table 4). AOD from OA peaks at low Southern latitudes in the two GISS models, LMD-zORINCA, and CICERO-OsloCTM2, and is low elsewhere, while the values are very, very low at all latitudes in HadGEM2, NCAR-CAM3.5 and MIROC-CHEM. In contrast, organic AOD is high in NCAR-CAM5.1 across a broad area of the tropics and even into the extratropics in both hemispheres, and is also broadly distributed in GFDL-AM3 though with a smaller magnitude than in NCAR-CAM5.1. We note that OA is the only component that typically exhibits a local peak AOD at 20° S, where the observations also show a local maximum, suggesting that the strong influence of OA on AOD at this latitude in some models is likely realistic. Most models exhibit a noticeable peak in sea-salt at around 50° S.

3.3 Satellite and AeroNet AAOD

While both scattering and absorbing aerosols contribute to AOD, they have very different effects on RF. Scattering aerosols exert a negative RF, while absorbing aerosols can cause positive RF depending on their single scattering albedo. Hence it is important to separate the absorbing component of aerosols. We therefore analyzed the absorbing aerosol optical depth (AAOD) in the ACCMIP models, again comparing with available satellite and ground-based observations. Note that there appeared to be a problem with the HadGEM2 AAOD diagnostic, so it was not included in this analysis.

We first compared the ACCMIP models' 2000 timeslice with observations from the Ozone Monitoring Instrument (OMI) (Torres et al., 2007) averaged over 2005–2007 (Fig. 7). The multi-model mean shows maximum values over central and northern Africa, the Arabian peninsula, South and East Asia, and tropical South America. OMI

measurements show a somewhat similar pattern. However, the OMI data also suggest large AAOD values in the Arctic that are not seen in the models, although satellite AAOD retrievals are especially challenging over bright surfaces (e.g. no data is available over Greenland, Antarctica or the Tibetan plateau) so these observations are less reliable than those elsewhere. Even at lower latitudes, the OMI values are generally much larger than those in the models in areas with substantial AAOD. The model values seem especially low over tropical South America, the Persian Gulf, and much of South and Southeast Asia. In addition, the observations suggest substantial transport of absorbing aerosol over the ocean from South America, southern Africa and southeast Australia, which is not captured in the models. This might indicate that absorbing aerosol lifetimes are too short in the models, though distributions seem reasonable in the Northern Hemisphere. Statistical evaluations show that the models generally have fairly poor spatial correlations with OMI, and that they are consistent with one another (mean R 0.34, range 0.28 to 0.40). The models generally underestimate AAOD by roughly a factor of two (mean 52 %, range 29 to 85 %).

We quantitatively evaluate AAOD on a regional basis against both OMI and AeroNet observations. We calculate the ratio of regionally averaged modeled AAOD to regionally averaged observed AAOD. The ratio values using OMI data are calculated including land-area locations only to be more comparable with AeroNet. For comparison, we show similar ratios calculated from the earlier AeroCom model intercomparison (Koch et al., 2009) (though that study did not include Northern Hemisphere Africa or South and Southeast Asia). Models underestimate AAOD in general compared with AeroNet (Fig. 8). This is especially the case for South and Southeast Asia, South America, and Southern Hemisphere Africa, where the model average AAOD is less than half the observed, but also for East Asia. Note, however, that these four areas have very limited coverage of AeroNet sites. Model performance is generally better for North America, Europe and Northern Hemisphere Africa. In comparison with OMI land-area AAOD, the models show similar biases to AeroNet except over North America, where underestimations relative to OMI are much larger. In comparison with either set of observations,

the GFDL-AM3 model shows the smallest overall underestimate of present-day AAOD, with the largest underestimates in GISS-E2-R-TOMAS and MIROC-CHEM. Biases in different regions tend to be systematic for a given model. For the four regions with the most pronounced low biases (South and Southeast Asia, South America, Southern

5 Hemisphere Africa and East Asia), every model examined is biased low in comparison with either AeroNet or OMI. High biases are seen most commonly for Northern Hemisphere Africa, where 2 of 9 models are high relative to OMI and 3 are high relative to AeroNet. The AAOD in this region, which includes the Sahara and Arabian deserts, is dominated by mineral dust aerosols rather than BC (which contributes less than 5 %

10 of total BC+dust AOD), suggesting that dust loading or absorption may be too high in these models (though biases are comparatively small). We note that calculations of the regionally averaged ratios of modeled to observed AAOD at individual locations always show larger values. This indicates that the model biases are most pronounced at locations with large AAOD.

15   Biases in the ACCMIP models are often fairly similar to those in the 2009 AeroCom analysis, though typically somewhat larger in comparison with AeroNet. Comparisons with OMI for Europe are very different, however, with the very large overestimate in the AeroCom models replaced by a smaller but still large underestimate in the ACCMIP models. Comparison of the models against OMI over the full land and ocean areas

20 reduces the model biases in all regions. In particular, multi-model mean ratios increase by 0.06 for East Asia, 0.07 for North America, and 0.08 for South and Southeast Asia. This accounts for a good portion of the difference for North America relative to the 2009 AeroCom analysis, which did not remove oceanic areas, though only a small portion of the East Asia difference.

25   Overall, the comparison with AeroNet reinforces the conclusion from examination of the OMI and multi-model mean global maps (Fig. 7) that the models severely underestimate AAOD over South and Southeast Asia, South America, Southern Hemisphere Africa and East Asia. Note that dust dominates the total BC+dust AOD over the central United States, Southern Europe, South Asia and parts of East Asia, so that part of the

low biases in regions such as South and East Asia could conceivably by due to under-estimates of dust loading as well as BC. The very large low biases in modeled AAOD over South America and Southeast Asia occur in areas where BC's contribution to total AAOD is quite large, however (as does the apparent underprediction of AAOD in the Arctic, though ground-based observations are not available to validate the satellite data in this region).

4 AOD trends

Long-term data on aerosol AOD is fairly limited. From satellites, the most complete longer-term record is the observations from the Advanced High-Resolution Radiometer that extend back to 1981. We average monthly mean AVHRR data produced by the Global Aerosol Climatology Project (GACP) (Geogdzhayev et al., 2005) and by NOAA (Zhao et al., 2008) over 1981–1986, excluding March 1982–December 1983 to avoid the effects of the El Chichon volcanic eruption on aerosol loading, and 1997–2003 and compare the difference between these two periods with the ACCMIP difference between the 1980 and 2000 timeslices. We analyze data over oceans and lakes, where the AVHRR retrievals are considered most reliable for trend analysis. Both versions of the AVHRR dataset show substantial decreases over most of the globe (Fig. 9). Decreasing trends in AOD are most pronounced around Europe, especially in the NOAA product, and off of eastern North America and over the Great Lakes (though the GACP product shows large decreases throughout much of the Northern Hemisphere). AOD also decreases off West Africa, though as interannual variability in dust emissions is very large, the relatively short averaging periods used here may not be representative for long-term trends.

The ACCMIP models show pronounced decreases in AOD over continental Europe and smaller decreases over eastern North America. These extend out over the nearby oceans. Quantitative comparison of the regional trends averaged over oceanic and lake areas were made by sampling the models where the satellite data were reported

over water for at least eight months during at least two years of both the 1981–1986 and 1997–2003 periods. Tests show that values in most locations are extremely similar using thresholds of 9 or 10 months instead of 8, though coverage is reduced at higher latitudes. Values are shown for sampling according to where the NOAA AVHRR product has observations. Sampling based on GACP locations yields values that are within .006 in all cases, and within 0.002 for eastern North America, South and East Asia and the Great Lakes. The comparison shows that the models generally produce trends in fairly good agreement with the NOAA analysis of AVHRR (Table 5). The multi-model mean captures the near-Europe, near eastern North America and Great Lakes decreases in aerosols over time especially well in comparison with NOAA AVHRR, though trends are too small in comparison with GACP AVHRR.

The ACCMIP models show large increases in AOD in east Asia, south Asia and Indonesia between 1980 and 2000 (Fig. 9). Observed trends in nearby oceans show increases in the NOAA product, but decreases in the GACP analysis. The multi-model mean increases are fairly similar to those in the NOAA product averaged over a broad area of near-Asian oceans, but they are substantially smaller than those seen the Yellow/Eastern Sea region where observed trends maximize. The modeled increases, however, extend over a broader area of the Indian and western Pacific Oceans. In comparison with GACP AVHRR, the modeled trends are far too positive for both the broader Asia region and the Yellow/Eastern Sea. It seems counterintuitive that aerosol loading would show decreasing trends near the rapidly developing Asian countries during this period, and thus we favor the NOAA analysis. Though inclusion of AVHRR data from 1984 could have left a residual negative bias in trends due to lingering aerosol from El Chichon, using 1987 instead of 1984 data has generally small effects on trends. Though it does reduce the magnitude of GACP trends over Europe and North America, leading to better agreement with the NOAA analysis and the models, it has only modest effects on the GACP trends over Asia and little effect on trends from the NOAA analysis anywhere (Table 5). Although there are substantial limitations to the AVHRR data, as highlighted by the very large differences between the GACP and NOAA datasets,

Full Screen / Esc

Printer-friendly Version

Interactive Discussion

and many assumptions about clouds and aerosols are required to go from observed AVHRR radiances to AOD (Li et al., 2009), the comparison suggests that in general the modeled AOD trends are fairly plausible, especially in comparison with the seemingly more plausible NOAA AVHRR analysis.

5   We note that over water near Europe and eastern North America, the GISS-E2-R simulations show particularly small reductions in AOD during the 1980s and 1990s. Analysis of individual components reveals that the difference relative to other models stems from the large increase in nitrate aerosol AOD in that model in these areas. Nitrate does not contribute as much to AOD elsewhere, and hence that model does

10 not diverge from others so strongly in other areas (and in fact is one of the best in capturing near-Asia trends). This result suggests that the nitrate forcing in the GISS-E2-R model is likely too strong. For the trends near Asia, the GFDL-AM3 and CICERO-OsloCTM2 models come the closest to matching the very large increases in AOD seen in the NOAA AVHRR analysis over the Yellow/Eastern Sea, but these same models

15 overestimate trends by roughly a factor of two with respect to that same NOAA AVHRR analysis over the broader South & East Asian coastal region (Table 5).

5   Historical and future aerosol forcing

Radiative forcing is a useful metric both for evaluating the total contribution of a given factor to climate change over a particular time and for comparing the influence of mul-

20 tiple factors. RF is not a perfect indicator of the eventual global mean temperature response that would occur for a sustained value of a particular forcing, but it is generally reasonably close. Some noticeable exceptions occur with aerosols, however, especially in the case of BC albedo forcing (Forster et al., 2007; Koch et al., 2011b; Flanner et al., 2007). The RF is calculated as the difference between double calls to

25 the radiation code with reference aerosols in the first call and actual aerosols in the second. Changes in this flux difference over time are then provided as RF. This diagnoses the so-called "direct" RF due to aerosols, but does not capture the various effects of

aerosols on clouds. To diagnose those, we use results from the additional simulations in which climate and emissions were set to different times and the flux change due to all aerosol effects were isolated (see Sect. 5.2).

BC surface albedo forcings were calculated in an additional set of simulations. Those runs were all conducted using prescribed meteorology from 1994–2000, with spinup from 1994–1995 and analysis (averaging) over 1996–2000. Black carbon and dust deposition fields from each ACCMIP model were prescribed with monthly resolution (annually-repeating), and linearly interpolated to the model timestep. The land simulations applied the NCAR Community Land Model 4 (Lawrence et al., 2011), using bias-corrected atmospheric forcing data from (Qian et al., 2006), and run at $1.9 \times 2.5°$ resolution. A sensitivity test run at 0.9×1.25 degree resolution showed global mean values within 1 % of those obtained at the coarser resolution. The sea-ice temperature, wind, specific humidity, and surface pressure forcing data come from NCEP, radiation data are from GISS, and precipitation data from the GCGCS blended product. The land snow treatments of aerosol processes and radiative transfer are described by (Flanner et al., 2007) and (Lawrence et al., 2011), and the new sea-ice aerosol and radiation treatments are described by (Holland et al., 2012). The snow and sea-ice fields generated with these offline configurations agree better with observed conditions during this time period than those simulated with coupled land-ocean-atmosphere simulations, but the precipitation and aerosol deposition fluxes are less compatible with each other than in coupled aerosol-climate simulations. The influence of this incompatibility on simulated surface snow BC concentrations and radiative forcing is somewhat mitigated by the use of temporally-smoothed monthly aerosol deposition fields. Additional analyses of the BC deposition fields, including extensive comparisons with both recent snowpack measurements and historical trends from ice-cores, as well as further discussion of the BC albedo forcing can be found in Lee et al. (2012).

5.1 Aerosol radiative forcing

5.1.1 Global mean preindustrial to present-day RF

We first examine global mean annual average RF between 1850 and 2000 by component and for the total from all aerosols (Fig. 10). Values from individual models are presented in Table 6. As the sample size is small in some cases, we show individual model results rather than a 'best estimate' and range. Sulfate RF was reported in nine models (some have nearly identical values, so are not distinguishable in Fig. 10). The mean and standard deviation of these RFs is $-0.40 \pm 0.13 \, \mathrm{W\,m^{-2}}$, and this range encompasses 6 of the 9 models. The only models exhibiting sulfate RF with a larger magnitude than that encompassed by this range are CICERO-OsloCTM2 and CSIRO-Mk3.6. The CICERO model showed the largest positive AOD biases of any model in sulfate-rich regions in comparison with MODIS or MISR (Table 4; CSIRO did not provide speciated data). The only model having a sulfate RF with a smaller magnitude than in this range is NCAR-CAM5.1. That model's AOD was biased low in sulfate regions in comparison with MODIS or MISR, but did not stand out from the other models. Though biases in present-day AOD do not necessarily correlate with biases in forcing, we thus estimate that the most probable range for present versus preindustrial sulfate RF is -0.18 to $-0.44 \, \mathrm{W\,m^{-2}}$ (i.e. the range of all models other than CICERO and CSIRO). We certainly cannot rule out larger negative forcings given that there is substantial uncertainty in relating AOD biases to RF biases, however.

Turning to carbonaceous aerosols, forcing was diagnosed according to emission sources as BC from fossil and biofuel (ff + bf) sources, OA ff + bf, and biomass burning total carbonaceous forcing. This source apportionment has been used as OA is always co-emitted along with BC emissions, but the BC/OA ratio is typically much lower for biomass burning. Evaluation by emission source is consistent with AeroCom (Schulz et al., 2006), and follows many recent efforts to assess forcing by emissions sector rather than pollutant (e.g. Unger et al., 2010; Shindell et al., 2008; Fuglestvedt et al., 2008). Though it clearly leaves us with a mixture of pollutant-based and sector-based

Full Screen / Esc

Printer-friendly Version

Interactive Discussion

analysis, it does at least help avoid giving the impression that BC from biomass burning, for example, could be reduced on its own. When considering the effect of emission mitigation or attributing forcing to particular activities, it is important to account for the fact that BCff + bf and OAff + bf also cannot be altered independently, and indeed many
5   activities that create or control emissions affect multiple pollutants.

For BCff + bf, results are available from five models (two models reported total BC and OA rather than the requested sector-based partitioning). These show a mean and standard deviation of $0.24 \pm 0.09 \, \mathrm{W \, m^{-2}}$, with a full range from 0.14 to $0.38 \, \mathrm{W \, m^{-2}}$. As shown in section 3, the models show distinct underestimates of AAOD in compari-
10 son with both OMI and AeroNet observations. Quantitatively, the global mean AAOD bias in comparison with OMI is 52 %, while biases with respect to AeroNet are even larger in most parts of the world, although we acknowledge that there are substantial uncertainties regarding the AAOD measurements themselves. This suggests that the BCff + bf RF could similarly be substantially underestimated, though the magnitude of
15 the bias is difficult to ascertain as some of the bias may be related to BC from biomass burning or to dust, and it is not obvious that biases in BC's present-day climatology translate linearly into biases in time-dependent forcing. Note that comparisons of historical patterns of BC deposition as recorded in ice cores with modeled values also reveals substantial biases in models (Lee et al., 2012), though again these cannot be
20 clearly related to RF.

There are only a few model results available for the rest of the individual components. The mean RF from fossil + biofuel OA is $-0.04 \, \mathrm{W \, m^{-2}}$, with a range from -0.01 to $-0.08 \, \mathrm{W \, m^{-2}}$ across the four available models. CICERO-OsloCTM2 reported the largest magnitude negative forcing ($-0.08 \, \mathrm{W \, m^{-2}}$), while the smaller values came
25 from GISS-E2-R ($-0.04 \, \mathrm{W \, m^{-2}}$), NCAR-CAM3.5 ($-0.01 \, \mathrm{W \, m^{-2}}$) and NCAR-CAM5.1 ($-0.02 \, \mathrm{W \, m^{-2}}$). We note that the latter three models all underestimate AOD in OA rich regions, with the largest biases in the two NCAR models (Table 4). In contrast, the CICERO-OsloCTM2 model shows a small positive bias. This suggests that the larger negative OA RFs, from -0.04 to $-0.08 \, \mathrm{W \, m^{-2}}$, reported by the models with smaller OA

rich region biases might be more realistic, though again there are substantial uncertainties in going from AOD to RF due to incomplete knowledge of the optical properties of OA.

The mean RF for biomass burning BC + OA is $0.00\,\mathrm{W\,m^{-2}}$, with a range from -0.02 to $0.02\,\mathrm{W\,m^{-2}}$ across the four available models. The RF is thus quite small and the limited number of models show fairly similar results. We note that the mean total carbonaceous aerosol forcing in these four models is $0.21\,\mathrm{W\,m^{-2}}$, while in the three additional models reporting total carbonaceous aerosol RF (MIROC-CHEM, CSIRO-Mk3.6 and LMDzORINCA) values were 0.10 to $0.32\,\mathrm{W\,m^{-2}}$. The MIROC-CHEM model, which reported the $0.10\,\mathrm{W\,m^{-2}}$ RF, has the greatest negative bias with respect to OMI AAOD of any model (Table 7), so is likely substantially low. The LMDzORINCA value lies within the range of the other four models that reported the requested sector-specific partitioning. The CSIRO-Mk3.6 model's carbonaceous forcing is somewhat larger, but not greatly so. Thus we are fairly confident that the reported ranges for the fossil + biofuel OA and biomass burning BC+OA are reasonable, and that these forcings are in the global mean fairly small for this time period.

The remaining two components are nitrate and SOA. Results are again available from 4–5 models, and for both components the models show substantial spread. In particular, two models have very large negative nitrate forcings, and one model has very large positive SOA forcing. For SOA, the substantial positive forcing in MIROC-CHEM is quite different from the other models, which show small negative forcings. This is attributable to the inclusion of different processes in that model, in which emissions of SOA precursors from the biosphere are coupled to the vegetation and are influenced by the change in land-use from 1850 to 2000. While some other models also couple emissions to vegetation, they use fixed present-day vegetation distributions. Thus only the MIROC-ESM-CHEM model incorporates the decrease in forest area leading to reduced emissions of SOA precursors, and hence a positive SOA RF. Thus in this case, the "outlier" may in fact be the most realistic model. This highlights the role of "structural" uncertainties as to which physical processes are represented in models in

addition to the more commonly assessed "scientific uncertainties" that are represented by the range of results across models incorporating similar processes seen for most of the other quantities assessed here.

The total aerosol RF was reported in 10 models, and the mean, standard deviation, and range are -0.26, 0.14 and -0.06 to -0.49 W m^{-2}, respectively. We also examine the total aerosol RF accounting for missing components (nitrate and SOA) in some models, which we call Aer+. Mean values for missing components are taken from the other ACCMIP models (excluding MIROC-CHEM SOA, with different processes that have thus far been assessed in only a single model), and are -0.05 W m^{-2} for SOA and -0.16 W m^{-2} for nitrate (weighting GISS-E2-R nitrate by 0.5 due to the aforementioned biases against AVHRR trends in nitrate-rich areas; Sect. 4). The mean, standard deviation, and range for Aer+ are -0.39, 0.14 and -0.12 to -0.62 W m^{-2}, respectively. As our previous analysis showed that accounting for missing components improved the agreement between models and satellite AOD in nearly all cases (Sect. 3), we consider the missing component-adjusted values to be more realistic. In our opinion, these values thus provide the best estimate of the total aerosol RF for this time period, though as noted, they likely underestimate positive forcing from fossil + biofuel BC.

While it is useful to know the best estimate of historical forcing, it is also important to know the forcing that was actually used in driving the CMIP5 climate simulations. We show the subset of eight ACCMIP models that also participated in CMIP5, in this case leaving out the nitrate and SOA forcing in MIROC-CHEM as that was not used in their CMIP5 runs (Fig. 10). The CMIP5 subset of ACCMIP models has a mean and standard deviation of is -0.28 ± 0.13 W m^{-2}, indicating that these models tend to underestimate total negative aerosol RF in comparison with our best estimate (Aer+).

As mentioned previously, several models included changes in dust and sea-salt aerosols in their simulations, and nearly all models included the effect of climate change on aerosols via the imposed SST and sea-ice trends (except NCAR-CAM5.1, CICERO-OsloCTM2 and CSIRO-Mk3.6). Several, though not all, models diagnosed the effect of these changes. In particular, comparison of the simulation with 1850 climate and 2000

emissions against the simulation with all conditions at 1850 against the full 1850 to 2000 change separates out the total impact of climate change on all aerosols. The global mean annual average effect on the all aerosol RF is $-0.02\,\mathrm{W\,m^{-2}}$ in HadGEM2, $-0.07\,\mathrm{W\,m^{-2}}$ in GFDL-AM3, $-0.17\,\mathrm{W\,m^{-2}}$ in GISS-E2-R and $0.07\,\mathrm{W\,m^{-2}}$ in MIROC-CHEM. Note that HadGEM2 did not include dust changes in their forcing calculation, perhaps accounting in part for their smaller net aerosol RF due to climate change. However, the range in the other models is clearly quite large. In addition, models include a variety of processes influencing these aerosols. In GISS-E2-R, for example, sulfate and nitrate aerosols can form coatings on mineral dust and sea-salt particles, changing their lifetimes. In fact, emission changes of primarily anthropogenic aerosol precursors from 1850 to 2000 lead to positive dust and sea-salt forcings of 0.09 and $0.03\,\mathrm{W\,m^{-2}}$, respectively, in that model even when climate change is not included. When climate change is included, the dust and sea-salt forcings become 0.03 and $-0.01\,\mathrm{W\,m^{-2}}$, respectively, indicating that climate change is causing increases in these aerosols that offset part or all of the decrease caused by coatings by other aerosols. The result that together dust and sea-salt aerosol changes contribute $-0.10\,\mathrm{W\,m^{-2}}$ of the RF due to climate change implies that in that model, 14 % of the 1850 to 2000 all aerosol RF is attributable to the influence of climate feedbacks on primarily anthropogenic aerosols, and 35 % of the 1850 to 2000 all aerosol RF is attributable to the influence of climate feedbacks on all aerosols. Values in other models range from 17 % to −58 %. Thus a non-negligible portion of the 1850 to 2000 aerosol RF may be attributable to the effects of climate change rather than aerosol direct or precursor emissions, but there is as yet no consensus on its value.

5.1.2   Time-varying global mean RF

Using the ACCMIP timeslices, we examine the aerosol forcing during the historical period and under two of the RCPs. We selected RCP 2.6 and RCP 8.5 as scenarios spanning the range of RCP projections. We focus this analysis on the total aerosol RF,

then examine the largest negative and positive components, sulfate and BC, respectively.

The total aerosol RF becomes increasingly negative in all models from 1850 to 1930, and again from 1930 to 1980 (Fig. 11). From 1980 to 2000, however, the total aerosol negative RF becomes weaker in six of the nine models. This is due to pollution controls that limited emissions, especially of sulfur dioxide. Sulfate RF weakens or stays approximately constant from 1980 to 2000 in all models for which data is available, even in those showing a reduced magnitude of negative total aerosol RF. In contrast, fossil + biofuel BC RF grows steadily more positive throughout the 20th century in all models, contributing to the weakening of the all aerosol negative forcing between 1980 and 2000. Interestingly, BC albedo forcing follows a separate path from fossil + biofuel BC RF, with the former peaking in 1980. This is due to the regional shift in the location of BC emissions from higher latitudes, where they can more easily reach Arctic snow and ice covered areas, to lower latitude developing nations (further details are presented in Lee et al. (2012)).

Note that the BC albedo forcing estimates reported here are smaller than those reported in previous studies (e.g. Flanner et al., 2007, 2009) because of the offline configuration that was applied, which produces less snow cover (and hence less area over which the forcing can operate) in the Tibetan Plateau and other parts of Asia. Because the forcing was quantified using snow and ice states which are representative of 1996–2000, and likely diminished relative to previous periods, actual BC snow forcings in 1850 may have been slightly greater (Lawrence et al., 2012). Additionally, BC albedo forcing is sensitive to the methodology of the calculation, with values reported from calculations internal to three of the ACCMIP models showing substantial variations from these offline results in their magnitude, though their time-dependence is similar (Lee et al., 2012).

The three models in which all aerosol RF from 1980 to 2000 becomes more negative are GFDL-AM3, GISS-E2-R and GISS-E2-R-TOMAS. GFDL-AM3 and GISS-E2-R-TOMAS did not diagnose RF by aerosol component. In GISS-E2-R, the all aerosol RF

21131

change from 1980 to 2000 is $-0.10\,\mathrm{W\,m^{-2}}$, with sulfate contributing $0.01\,\mathrm{W\,m^{-2}}$, carbonaceous aerosols $0.05\,\mathrm{W\,m^{-2}}$, nitrate $-0.13\,\mathrm{W\,m^{-2}}$ and SOA $-0.01\,\mathrm{W\,m^{-2}}$. Hence the RF becoming more negative is primarily attributable to nitrate in that model. Note that this cannot be the cause in the other two models as they did not include nitrate.

5   Analysis of ocean heat uptake and the planetary energy budget suggests that aerosol forcing indeed became more negative in the late 1990s and early 2000s relative to the 1980s and early 1990s (Church et al., 2011).

In the RCP emission scenarios, all aerosol RF declines greatly in most models. There is little different between the two scenarios in the MIROC-CHEM model. The

10   CICERO-OsloCTM2 and LMDzORINCA models show substantially greater decreases in the magnitude of negative aerosol RF in 2030 under RCP2.6 than under RCP8.5, but the differences narrow further in the future. In contrast, differences between the two scenarios increase throughout the 21st century in the GFDL-AM3 model. In that model, all aerosol RF stays approximately constant under RCP8.5. All aerosol RF becomes

15   steadily more negative throughout the 21st century in the GISS-E2-R model. This results, as did that model's 1980 to 2000 trends, from a combination of increased nitrate negative RF and reduced BCff + bf positive RF which together outweigh the reduced negative RF from other scattering aerosols. Most of the increase is due to nitrate, for which the 2100 versus 2000 RF is $-0.36\,\mathrm{W\,m^{-2}}$ under RCP2.6 and $-0.49\,\mathrm{W\,m^{-2}}$ under

20   RCP8.5. In an analysis with the HadGEM2 model, Bellouin et al. (2011) report 2100 versus 2000 nitrate forcings of $-0.4\,\mathrm{W\,m^{-2}}$ and $-0.5\,\mathrm{W\,m^{-2}}$ for RCPs 2.6 and 8.5, respectively, including both direct and cloud albedo effects (the ratio of nitrate direct forcing to nitrate direct plus cloud albedo forcing for 2000 versus 1850 is 0.71 in their model, suggesting that the direct forcing is ∼30 % lower than these RCP RF values –

25   those estimates are shown in Fig. 11). Hence the HadGEM2 results seem fairly consistent with the GISS-E2-R nitrate projections, while diagnostics of future nitrate forcing were not available from any of the other models. Nitrate aerosols become increasingly important in the future both because sulfate aerosols are greatly reduced, affecting nitrate since sulfate and nitrate precursors compete for a limited supply of ammonium in

Full Screen / Esc

Printer-friendly Version

Interactive Discussion

the atmosphere, and because the emission scenarios assume that effective pollution controls are put in place on most aerosol precursors from industry, vehicles and power generation, but that ammonia emissions from agriculture continue to increase during the 21st century (van Vuuren et al., 2011). Note that in some models, dust and sea-salt forcing was included in RF (Table 1). While diagnostics were not available for these natural aerosols in most models, in the GISS-E2-R model they were remarkably stable, contributing less than $0.03\,\mathrm{W\,m^{-2}}$ to 2100 forcing.

Analysis of trends over the very recent past (2000 to 2010) shows small trends in aerosol RF. Across all four RCPs, results from five models (though not all models ran all scenarios) show aerosol RF from -0.013 to $0.033\,\mathrm{W\,m^{-2}}$, with mean and median values of $0.007\,\mathrm{W\,m^{-2}}$ and $-0.001\,\mathrm{W\,m^{-2}}$, respectively. For RCPs 4.5 and 6.0, with at least three model results available (Table 1), values are not consistent even in sign among the three models.

5.1.3 Geographic pattern of RF

While the analysis of global mean aerosol RF presented in the previous sections provides useful insight into the planetary-scale contribution of aerosols to climate change, the aerosol RF is of course highly inhomogeneously distributed over the Earth. This has important consequences for both global and especially for regional climate change, as climate feedbacks are non-uniform and aerosol impacts tend to be largest in areas with greatest forcing (e.g. Rotstayn and Lohmann, 2002; Ming and Ramaswamy, 2009; Boer and Yu, 2003; Shindell et al., 2010). We therefore analyze the spatial pattern of aerosol RF, beginning, as with the global mean analysis, by examining the 2000 versus 1850 RF.

The preindustrial to present-day forcing by sulfate is greatest over the most industrialized and heavily populated areas of the world, especially east and south Asia, Europe and eastern North America where negative forcing exceeds $-1\,\mathrm{W\,m^{-2}}$ (Fig. 12). The areas with greatest forcing extend past these regions, where the emissions of sulfur dioxide are largest, out over the nearby oceans and over the Middle East, due to

atmospheric transport. The variation across models is greatest in these same regions, and is fairly uniform across the regions.

fossil + biofuel BC RF is, like sulfate, very large over east and south Asia where it is more than $1\,W\,m^{-2}$, but is comparatively small over Europe and North America. The spatial distribution of fossil + biofuel OA RF is very similar to that for fossil + biofuel BC, unsurprisingly, but the RF has the opposite sign and a much smaller magnitude.

In contrast with the other aerosol components, which have the same sign throughout the globe, biomass burning aerosol RF and SOA RF show regions of both positive and negative forcing. For biomass burning, this is because of varying regional trends in fire frequency, which has decreased in areas such as the southeastern United States relative to 1850, while it has increased in tropical areas such as Indonesia. In the case of RF due to changes in SOA, the large areas of positive forcing over south and southeast Asia and the southeastern United States come from the MIROC-CHEM model's incorporation of changing land-use. As the other models do not include this factor, there is an extremely large standard deviation in this field. While the global mean masks regional patterns for all aerosols, the existence of areas of both positive and negative forcing means that the global mean can be particularly misleading for these two components.

Finally, forcing from nitrate aerosols shows local maxima over East Asia, Europe and eastern North America, and to a lesser extent over south Asia. This forcing is in many respects similar in distribution to that of sulfate. There is a broader distribution of small forcing values in the Southern Hemisphere for nitrate, however. This stems from both the MIROC-CHEM model and especially from the GISS-E2-R model, which efficiently lofts ammonia in convective plumes from areas near tropical sources to the upper troposphere, where it then spreads to both hemispheres. This leads to unexpectedly large nitrate aerosol abundances in the upper troposphere over much of the world, though given the paucity of in situ measurements it's difficult to evaluate this forcing. As noted previously, that model appears to underestimate AOD trends near North America and Europe, which seems linked to overly large increases in nitrate, so

Title Page

Abstract | Introduction

Conclusions | References

Tables | Figures

◄ | ►

◄ | ►

Back | Close

Full Screen / Esc

Printer-friendly Version

Interactive Discussion

the nitrate forcing over Southern Hemisphere mid-latitudes, coming as it does in large part from one model, may also be too large in the multi-model mean. As the standard deviation map shows, there is substantial divergence between models in this region. In comparison, standard deviations are of comparable magnitude over industrialized area, but forcing is much larger, indicating that forcing in those regions is relatively robust. A recent analysis of nitrate forcing in a model for which the nitrate distribution compared relatively well with available observations showed annual mean nitrate RF of $-0.95 \, \text{W m}^{-2}$ over China (relative to zero nitrate) (Zhang et al., 2012). The GISS-E2-R model finds nitrate forcing over China of $-1.08 \, \text{W m}^{-2}$ (relative to zero nitrate), in good agreement with that study. In the GISS-E2-R model, the 2000 versus zero nitrate RF is 59 % larger than the 1850 to 2000 nitrate forcing. Using that same factor to convert the others to 2000 forcing relative to zero nitrate, the CICERO-OsloCTM2 average over China would be $-0.56 \, \text{W m}^{-2}$ while the MIROC-CHEM value would be $-2.22 \, \text{W m}^{-2}$ over China. Thus the much smaller nitrate forcing in the CICERO-OsloCTM2 model seems too low relative to the Zhang et al study, while MIROC-CHEM is substantially larger. Especially given the small number of models having reported nitrate RF, it is clear that uncertainties are especially large for this aerosol component.

The geographic distribution of the all aerosol RF shows large negative values over most Northern Hemisphere land areas below 60° N. The only exceptions are the Pacific Northwest, where forcing is near zero, and the Sahara and the Tibetan plateau regions, where forcing is positive. These latter two regions have very high surface albedo, reducing the effect of scattering aerosols and increasing the effect of absorbing aerosols, leading to the net positive forcing. There is a substantial local maximum in negative forcing over the Amazon that is largely attributable to forcing from SOA, and large negative values over western Central Africa that are driven by SOA, biomass burning and nitrate. This suggests that forcing in these two regions may be underestimated (i.e. not negative enough), as many of the models contributing to the all aerosol forcing do not include one or both of these aerosols. Forcing in the Arctic is weakly positive, except over Greenland where it is a stronger positive value. As with other high albedo areas,

this results from a stronger local effect of absorbing BC than of the scattering aerosols. Substantial forcing also extends over much of the North Atlantic, the northern Indian Ocean, the Caribbean, and the eastern Pacific off of Central America.

Model-to-model variations in all aerosol RF are greatest over the Arabian Peninsula, west Africa, and Indonesia. The latter two appear to be associated with SOA and biomass burning aerosols, while the diversity over Arabia is likely due to it having a large magnitude of forcing that arises primarily from long-range transport which can vary substantially between models, with contributions from dust changes included in some models as well.

BC albedo forcing is positive everywhere for this period, with largest values in western Russia, the Karakoram and Manchuria. Substantial positive values are seen over most of the Arctic, though values are not as large as those at lower latitudes where sunlight is more plentiful.

We have also examined the geographic distribution of forcing through time. We focus on the largest components, namely sulfate and either the combined RF from fossil + biofuel BC and OA along with the biomass burning forcing (the carbonaceous aerosol RF) or the fossil + biofuel BC RF. The combined carbonaceous aerosol RF is simpler to display than all three components, and as shown previously the OA and BB forcings are comparatively small. We also examine BC albedo forcing, as this is not included in the standard RF.

The analysis shows that for both sulfate and carbonaceous aerosols, RF in 1930 was primarily concentrated over Europe and eastern North America (Fig. 13). Magnitudes increased substantially in those areas from 1930 to 1980, while large forcings also appeared over east Asia, and for sulfate, over western Central Africa and Southern Africa, Central and South America, and southeast Asia. From 1980 to 2000, negative all aerosol RF increased substantially over south Asia, Indonesia and to a lesser extent over east Asia and Mexico, but forcing decreased over other regions including Europe, eastern North America and western Africa (Fig. 14). Over Europe and eastern North America, the large positive forcing trend results from a decline in sulfate forcing due to

successful implementation of sulfur dioxide emission controls. In the case of Europe, the effect of sulfate reductions outweighed the effect of reductions in fossil + biofuel BC during this period. All aerosol RF over South Asia became increasingly negative during this time as increased sulfate outweighed increased BC. Note that these more nearly offset one another over East Asia, leading to very small trends in all aerosol RF. Trends during 1980 to 2000 over Indonesia and western Africa are attributable to changes in biomass burning (they are not apparent in the fossil + biofuel BC RF map in Fig. 14), which increased in Indonesia and decreased in western Africa. BC albedo forcing shows declines over North America from 1930 to 1980, while increasing markedly over Eurasia during this time. Values are especially large over western Russia, an area downwind of European BC sources and one with substantial biomass burning. Over the 1980 to 2000 period, BC albedo forcing decreases in most of Russia, though it remains large, while increasingly greatly over the Karakoram and Manchuria.

The all aerosol RF from 2000 to 2030 shows trends that are spatially similar in many respects those seen for 1980 to 2000 (Fig. 15). Under either RCP2.6 or RCP8.5 the magnitude of negative all aerosol RF over Europe and North America continues to decline, though more so under RCP2.6. Likewise the magnitude of negative all aerosol RF continues to increase over South Asia, especially under RCP8.5 where it grows by up to $0.5\,\mathrm{W\,m^{-2}}$. As with the recent past, trends in scattering and absorbing aerosols are more nearly balanced over east Asia, so that negative all aerosol RF in this regions increases slightly in RCP8.5 but decreases slightly in RCP2.6 (under which positive carbonaceous aerosol forcing decreases over east Asia). By 2100, aerosol forcing has declined sharply in magnitude virtually everywhere, with regions where present versus preindustrial RF was negative showing large positive 2100 versus 2000 trends and negative trends in regions such as the Arctic and Tibetan Plateau where present versus preindustrial RF was positive. As with the global mean, differences between the scenarios are larger at 2030 than at 2100.

5.1.4 Quality screening of models

Based on the evaluation against observed AOD, we now test if there is a relationship between model skill and aerosol RF. The models with the highest correlation (over 0.65) against the two satellite datasets or AeroNet do have a narrower range, RF of −0.16 to −0.49 W m^{-2}, than the full set of models (Fig. 16). Looking at the bias with respect to observations yields similar results, namely that all models with biases within 20 % of the observations have forcing −0.16 to −0.49 W m^{-2}. Using these same limits, screening the models by correlation with respect to MODIS fine-mode fraction over the oceans gives identical results, as does screening by bias with respect to MODIS fine-mode (though the latter excludes more models). In effect, the evaluation against observed AOD screens out the models with the lowest forcing values, but it cannot discriminate between models within the −0.16 to −0.49 W m^{-2} range. The range for that same subset of quality-screened models becomes −0.33 to −0.62 W m^{-2} when we account for missing components. Screening the models based on comparison of near-Europe and near-South and East Asia NOAA AVHRR AOD trends, leaving out the models with lowest and highest trends leads to a slightly reduced range of −0.16 to −0.40 W m^{-2}, or −0.33 to −0.50 W m^{-2} when we account for missing components. Note, however, that the CSIRO-Mk3.6, GISS-E2-R-TOMAS and MIROC-CHEM models are all absent from the AVHRR analysis, which may contribute to the reduced range seen there. Hence the full range of the "best" models based on all screening is encompassed by −0.42 ± .09 W m^{-2} (Aer+). This RF is almost identical to the multi-model mean of the full missing component-adjusted ACCMIP dataset, but has les than half the range in the full set of models. Thus although there are large differences in the radiative forcing per unit AOD in aerosol models, and thus screening by AOD would not obviously lead to a reduced range in RF, it appears that this is the case in this set of models. Note that the screening of models is not definitive as it does not take into account uncertainties in emissions. Thus those models which are in closest agreement

with this prescribed emission dataset would not necessarily be the same if the emissions were varied within the uncertainty in the emissions inventories.

We performed a similar analysis of fossil + biofuel BC forcing in comparison with model skill in representing AAOD. Unfortunately, the requisite data was available from only 5 models. The limited analysis we were thus able to carry out did not show robust relationships between skill and RF. The spatial correlation with OMI AAOD tended to be best for models with greatest BC RF (though correlations were comparatively low in all models), while surprisingly the bias in models was inversely correlated with BC RF (i.e. the more the model underestimated AAOD, the larger its forcing). These results were the same using either global OMI data or only OMI data below 60° N (for which the models show much higher spatial correlations; Table 7). We believe the lack of robust conclusions based on screening by AAOD is likely the result of BC being a proportionally smaller contributor to total AAOD than anthropogenic aerosols are to total AOD. In most ACCMIP models, BC contributes 3–17 % of the AAOD, while the primarily anthropogenic aerosols (sulfate, nitrate, BC and OA) contribute 26–80 % of AOD. Hence a model's ability to reproduce present-day climatological AAOD provides a poor test of its long-term BC RF.

5.2 Aerosol adjusted forcing

In addition to the standard RF from aerosols, we have calculated the "adjusted forcing" (AF), defined here as the top-of-the-atmosphere (TOA) net energy flux change with ocean conditions held fixed but all other processes allowed to respond to the aerosol changes. The AF thus includes aerosol indirect effects on clouds via microphysics (affecting cloud albedo and cloud lifetime) as well as responses of water vapor, lapse rate and clouds to aerosol thermodynamic impacts along with direct aerosol forcing. In half the models' ACCMIP runs, the effects of BC-induced albedo changes are also included (GISS-E2-R, GISS-E2-R-TOMAS, MIROC-CHEM and NCAR-CAM5.1). Prior studies have shown that AF is in general a better indicator of the eventual climate response than RF (Hansen et al., 2005). The AF values come from comparison of the 1850

D. T. Shindell et al.

Title Page

Abstract | Introduction

Conclusions | References

Tables | Figures

◄ | ►

◄ | ►

Back | Close

Full Screen / Esc

Printer-friendly Version

Interactive Discussion

simulations against simulations driven by a given year's emissions while maintaining 1850 climate and greenhouse gas concentrations. The experimental design for these simulations was that aerosols were allowed to interact with the models' radiation (and hence climate), while ozone changes were not. This permits us to diagnose aerosol AF
5 from the total flux changes, as aerosols were the only changes influencing radiation, while the inclusion of changes in gaseous emissions permits oxidant changes to affect aerosols and also allows examination of the effect of emissions alone on air quality in the ACCMIP models (changes in surface ozone and aerosols). The CMIP5 protocol included a pair of simulations with fixed ocean boundary conditions and only aerosols
10 changing between 1850 and 2000 that also allows diagnosis of aerosol AF for this time period. We make use of these simulations for three models: LMD (as ACCMIP results were not available), HadGEM2 (as ACCMIP simulations were performed with aerosols, ozone and methane changes all affecting climate), and CSIRO (as BC albedo did not affect radiation in their ACCMIP runs but did in their CMIP5 runs).
15   As with RF, we begin by examining the 1850 to 2000 aerosol AF (Fig. 17). The spatial pattern of aerosol AF is in many ways quite similar to the pattern of aerosol RF, with maxima in many of the same areas. The AF is relatively stronger over aerosol outflow regions in the North Pacific, the North Atlantic, and the Tasman Sea, however. This is likely because anthropogenic aerosols have an enhanced effect on clouds in these
20 remote areas where there are often few natural cloud condensation nuclei and high humidity. The AF is strongly positive in several regions, including the Sahara, parts of the Himalayas/Karakoram, and over both polar regions. Over much of the Arctic Ocean, values are more than $0.5\,\mathrm{W\,m^{-2}}$. Examining the seasonal AF, Arctic forcing is especially large in boreal spring and summer, with values exceeding $0.75\,\mathrm{W\,m^{-2}}$ over large
25 areas of the Arctic Ocean, the Canadian archipelago and Greenland during spring and values exceeding $1.75\,\mathrm{W\,m^{-2}}$ over large parts of Canada, Alaska, Siberia and the Arctic Ocean during summer (Fig. 18). This is attributable to both the enhanced direct effect of absorbing aerosols relative to scattering aerosols over highly reflective surfaces discussed previously, but also to the influence of clouds at high latitudes as with

Radiative forcing in the ACCMIP

D. T. Shindell et al.

comparatively little incoming solar radiation their ability to trap outgoing longwave radiation can outweigh the increase they induce in reflected solar flux. Part of the response over northern Canada may also be related to reduced snow cover due to BC. The very strong positive aerosol AF suggests that aerosols may have played a greater role in rapid climate change in the Arctic than has generally been appreciated.

The standard deviation of the AF values across models is large in many locations. When taking a global average over the standard deviation at all points, the value is $1.34\,\mathrm{W\,m^{-2}}$, far larger than the standard deviation of any individual aerosol component's RF. The value when computing the standard deviation across each model's global mean AF is only $0.23\,\mathrm{W\,m^{-2}}$, however, indicating that the models are in fact producing fairly similar total aerosol AFs but with the forcing location shifted between one model and the next. In fact, the standard deviation of the models' global mean AF values is 19% of the multi-model mean, which is less than the comparable standard deviation for all aerosol RF (50%) or for aerosol RF by component (35% for sulfate, 40% for BCff + bf, 80–95% for OAff+bf and nitrate, and more than 100% for biomass burning and SOA). The noisy pattern of AF, however, indicates that it could be difficult to calculate local AF values for small forcings, though these can be easily isolated in the RF methodology (which is not influenced by meterological variability). Over regions with substantial AF, standard deviation values are much larger than the corresponding RF standard deviations, but are proportional to the AF/RF ratios. In fact, the relative standard deviation of the AF is no larger than that of RF over most regions with substantial aerosol forcing (Fig. 19). Over some areas, such as parts of East Asia, the relative standard deviation of AF is actually substantially smaller.

Atmospheric forcing by aerosols (defined as TOA AF minus surface net flux change) shows strong absorption of energy in the atmosphere in regions where BCff + bf and biomass burning RF are large. There are also clear indications of dynamics changes, with an apparent shift in the jet stream over North America and a shift in cloud cover over Australia. As these latter effects may be related not only to aerosol induced changes in cloud cover but also to dynamical responses to the artificial temperature

Printer-friendly Version

Interactive Discussion

gradients caused by using fixed SSTs but allowing land temperatures to adjust they should be interpreted with caution. The 2000 versus 1850 reduction in shortwave flux reaching the surface due to aerosol (including their effects on clouds, water vapor, etc.) is $2.34 \pm 0.99\,\mathrm{W\,m^{-2}}$ in the six ACCMIP models providing this diagnostic. This value is

5 in excellent agreement with the most recent IPCC assessment of -2.3 with a range between -1.3 and $-3.3\,\mathrm{W\,m^{-2}}$ (Denman et al., 2007).

As aerosol AF includes both the so-called direct and indirect forcing, AF minus RF provides a rough estimate of the aerosol indirect effect on clouds (though it includes additional responses such as water vapor and lapse rate adjustments, as

10 noted previously). This yields a global mean value of $-0.90\,\mathrm{W\,m^{-2}}$. Either the indirect component or the aerosol AF can be compared with prior modeling, observationally-constrained estimates, and inverse studies. The IPCC AR4 provides a best estimate of the cloud albedo portion of the indirect effect of $-0.7\,\mathrm{W\,m^{-2}}$ with a range of -0.3 to $-1.8\,\mathrm{W\,m^{-2}}$ (95 % confidence) (Forster et al., 2007). AF estimates from models con-

15 strained by satellite data include estimates of -0.6 to $-1.2\,\mathrm{W\,m^{-2}}$ (Sekiguchi et al., 2003) and of $-1.2 \pm 0.4\,\mathrm{W\,m^{-2}}$ (Quaas et al., 2009). The latter study reports a clear-sky effect of $-0.4 \pm 0.2\,\mathrm{W\,m^{-2}}$ and a cloudy-sky effect of $-0.7 \pm 0.5\,\mathrm{W\,m^{-2}}$. These can be interpreted as approximately the direct and indirect forcings, respectively, and hence are in good agreement with our results. Inverse methods based on observa-

20 tions of temperature change, ocean heat uptake, and non-aerosol forcings find an AF of -0.18 to $-0.83\,\mathrm{W\,m^{-2}}$ (Libardoni and Forest, 2011), $-1.1 \pm 0.4\,\mathrm{W\,m^{-2}}$ averaged over 1970 to 2000 (relative to preindustrial) (Murphy et al., 2009), $-0.8 \pm 0.4\,\mathrm{W\,m^{-2}}$ for the 1980s and early 1990s (relative to preindustrial) (Church et al., 2011), $-1.6 \pm 0.3\,\mathrm{W\,m^{-2}}$ averaged over 2005–2010 (relative to preindustrial) (Hansen et al.,

25 2011), and $-1.3 \pm 0.5\,\mathrm{W\,m^{-2}}$ for 2007 versus 1890 (Shindell and Faluvegi, 2009). Hence the ACCMIP models' AF mean and approximate 5–95 % confidence interval (1.65-σ) of $-1.2 \pm 0.4\,\mathrm{W\,m^{-2}}$ seems to be quite consistent with both inverse estimates and satellite-constrained modeling.

As many more models provided AF results at 2000, we have more confidence in that value, and thus we evaluate AF at other times based on fractional differences relative to 2000 in models that diagnosed AF at both times. The temporal evolution of aerosol AF does not closely follow the temporal evolution of all aerosol RF (Fig. 20). Through 1980, the AF trends seem to follow the evolution of scattering aerosol RF, which increases from $-0.13\,\mathrm{W\,m^{-2}}$ in 1930 to $-0.49\,\mathrm{W\,m^{-2}}$ in 1980, for an increase of 377 %. During this same time, AF increases by $\sim$375 %, while all aerosol RF increases by more than 500 %. AF continues to increase from 1980 to 2000, however, although both all aerosol RF and scattering aerosol RF tend to decrease. Aerosol AF became more negative in all three models that calculated aerosol AF differences between 1980 and 2000, though aerosol RF also became more negative in two of those. In one of the models with increasingly negative RF and AF, the growth in the magnitude of AF during this time was much larger than that of RF. Together with the model showing increasingly negative AF despite a decline in the negative RF magnitude, this indicates that AF trends are not as closely coupled to RF during this period as they were earlier. This suggests that, unsurprisingly, AF may be quite sensitive to the background aerosol loading upon which perturbations are imposed, the geographic location of the aerosols, and the mixture of aerosol types. In particular, the increases in negative AF from 1980 to 2000 are largest over East and South Asia (Fig. 20), while increases in negative all aerosol RF are fairly small there during this time, especially over East Asia due to the offsetting effects of increasing fossil + biofuel BC and scattering aerosols (Fig. 14). Thus the weak RF changes over Asia leave the global mean RF trends dominated by decreasing aerosol over Europe and North America, but the AF is dominated by increasing negative forcing over Asia due to the overall increase in aerosol loading there which outweighs AF reductions over Europe and North America.

Diagnoses of future AF are only possible for RCP8.5. We analyze flux differences between the simulations RCP8.5_YYYY and Em2000ClYYYY where YYYY is the future year. Such simulations were requested for 2030 and 2100. This difference isolates the effects of emissions changes by removing the impact of climate change from the

RCP simulation. As ozone also changed in the RCP8.5 simulations (in most models), we subtract the ozone forcing to get the aerosol AF. Future AF shows large positive forcing for 2030 relative to 2000 over Europe and the eastern US and negative forcing over South Asia and the Himalayas. This spatial pattern is generally similar to the 2000 relative to 1980 AF distributions, with the primary exception being that AF has ceased becoming more negative over East Asia. Owing to both a larger area with positive AF in the NH middle latitudes and the smaller area with increasingly negative AF over Asia, the global mean AF trend changes direction during this time. By 2100, the AF has become positive nearly everywhere relative to 2000. The spatial pattern looks very much like the inverse of the 1980 or 2000 AF (relative to 1850), indicating that most of the historical aerosol forcing has been removed. The only large exceptions are the negative aerosol forcings over tropical Africa and South America related to biomass burning. The timeseries shows that the global mean AF is projected to become less negative from 2000 to 2030 under RCP8.5. By 2100, AF has become much less negative, nearly recovering to its 1850 value. Note that unlike RF, AF becomes less negative over time in all the models for which diagnostics are available, including the GFDL-AM3 and GISS-E2-R models that showed steady or even increasingly negative aerosol RF in the future. We expect that AF would be fairly similar at 2100 under all the RCPs since they all envision nearly complete removal of anthropogenic aerosol and aerosol precursor emissions, except for ammonia (Lamarque et al., 2012b). As seen in the analysis of aerosol RF, there are differences in the timing of RF reductions (Fig. 11), and given the divergence in modeled aerosol RF for 2000 to 2030 it is not clear that AF can be inferred for these times for other RCPs, nor for 2000 to 2010 when modeled aerosol RF is also not consistent in sign. Nonetheless, global mean RF changes during 2000 to 2010 are small in all models, suggesting that AF is unlikely to have decreased substantially during this period. It is even plausible that AF continued its apparent 1980 to 2000 increasingly negative trend.

To explore the role of specific aerosol types on AF, simulations to isolate the contribution of individual aerosol components to the 2000 versus 1850 AF were carried out

with the GISS-E2-R model. With all other conditions set at year 2000 values, sulfate, BC and OA were individually removed and their direct RF and AF were diagnosed in 50-year atmosphere simulations with fixed ocean conditions. At the same time, a cloud forcing diagnostic was saved that calculates the flux perturbation due to the model's clouds relative to zero clouds everywhere, so that the difference between the 2000 control run cloud forcing and the cloud forcing in the aerosol perturbation experiments yields the cloud forcing due to aerosols. The results of these calculations are presented in Table 8.

The simulations reveal that for OA and BC, cloud forcing is equivalent in magnitude to RF, and AF is statistically equivalent to a linear sum of the direct RF and the cloud forcing (though the mean AF estimated for OA is ∼20 % less than the direct plus cloud RF). In contrast, for sulfate the cloud forcing is larger than the direct RF, and the AF is clearly less (∼25–30 %) than the direct plus cloud forcings. This suggests that the greater solubility of sulfate causes it to have an enhanced cloud forcing relative to OA by more efficiently serving as cloud condensation nuclei, and that the overall effect of BC on clouds is dominated by thermodynamic effects of local heating rather than microphysical effects in this model. In the all aerosol case, cloud forcing is much greater than direct RF, which is likely due to the logarithmic dependence of cloud droplet number concentration on nucleation sites (Gultepe and Isaac, 1999) leading to a greater response at the low aerosol numbers reached when all aerosols are removed simultaneously. The all aerosol AF is, like sulfate (and perhaps OA), approximately 25–30 % less than the sum of the direct and cloud forcings. This suggests that other rapid responses, such as adjustment of the temperature lapse rate and water vapor concentration, compensate for some of the cloud response.

From these results, it appears that aerosol indirect effects could be roughly partitioned to individual species by assuming the sum of all BC's indirect effects (including so-called "semi-direct" effects) is equal to it's direct effect (and is of the same sign) and indirect effects of scattering aerosols add roughly and additional 75 % of their direct RF to their net impact. As the scattering components contribute −0.73 W m^{-2} in

the all aerosol case, this yields a scattering aerosol AF of $-1.28\,W\,m^{-2}$, and thus a total AF (including BC) of only $-0.82\,W\,m^{-2}$, however. The indirect effects of scattering aerosols thus might be better represented by an estimate that varied from $\sim 50\,\%$ of their direct effect for small changes to $100\,\%$ at large reductions. Though to the best of our knowledge the relative indirect effect of individual aerosol components has not previously been examined, several studies have investigated the indirect impact of BC alone. There is a large range seen in the literature, which shows values ranging from about $-0.35\,W\,m^{-2}$ to $+0.3\,W\,m^{-2}$ just for the effect of BC on mixed-phase or ice clouds (Penner et al., 2009; Liu et al., 2009). In addition, while many climate models find a substantial negative BC indirect forcing, observationally-constrained estimates often indicate this forcing is positive (Ruckstuhl et al., 2010; Kaufman and Koren, 2006). This has led recent assessments to conclude that the most likely range for BC's indirect forcing is -0.4 to $+0.4\,W\,m^{-2}$ (UNEP/WMO, 2011; Shindell et al., 2012a). Hence reliable quantification of aerosol AF due to individual components remains a substantial challenge for the community.

5.3 Comparison of Forcing with AOD and burden changes

As calculation of RF adds some computational expense, and calculation of AF adds a great deal, forcing is often not diagnosed. It is therefore of interest to test how well forcing can be estimated based on changes in AOD or aerosol burdens as those quantities are more typically saved from models. Analysis of aerosol burdens can also help us understand the relative importance of emissions and lifetime changes in driving aerosol forcing. Comparison of aerosol forcing with AOD changes shows that AOD changes are overall fairly highly correlated with calculated RF (Fig. 21). Overall, the correlation is $r^2 = 0.95$ and the RF per unit AOD change (RF/dAOD) is -8.5 (-9.8 to -7.5 95 % confidence interval (CI)). Grouping the points by time interval the correlation is better for the larger 1850 to 2000 RF ($r^2 = 0.88$) than for the RF over 1980 to 2000 ($r^2 = 0.72$). Even in the former case, however, AOD changes that differ by a factor of

two can lead to nearly the same RF. The RF/dAOD is -8.8 (-13.7 to -6.4 95 % CI) for the 1850 to 2000 values, and -11.2 (-40.0 to -6.6 95 % CI) for the 1980 to 2000 values. Hence for the 1980 to 2000 case, though there is a fairly strong correlation (i.e. linear regression explains most of the variance), the fit has a very large uncertainty so that inferred RF based on AOD changes would have a 95 % CI of $+257/-41$ %. Uncertainties on inferred RF would be about 30–50 % using the 1850 to 2000 regression, and only 12–15 % using the regression through all points. Hence it seems that AOD may provide a reasonable indicator of RF for large AOD changes, but is not reliable for smaller changes that generally occur over shorter time periods. Turning to AF we find that AOD changes provide a fairly poor indicator of AF. Based on all models and times, the correlation is $r^2 = 0.43$ and the AF/dAOD is -34.5 with a very large 95 % CI spanning -667 to -17.5. Note that a change in global mean AOD of zero can produce a substantial forcing in both the RF and AF cases.

One reason that AOD changes may not provide a better indicator of forcing is because AOD changes include both cooling and warming agents. To see if these might be separated, we also examined correlations between the 2000 versus 1850 RF from sulfate and the change in sulfate burden and between BC ff + bf forcing and BC burden changes (burden changes are presented in Table 9). Correlations between sulfate burden changes are sulfate RF are fairly weak at $r^2 = 0.44$, while correlations between BC burden changes and BC forcing are near zero. This suggests that variations in the optical properties of the aerosols are too large to allow burden changes alone to provide a good indicator of RF, as in prior studies (Schulz et al., 2006).

Examination of changes in sulfate removal and BC emissions shows large variations across models for sulfate removal, implying substantial differences in sulfur emissions probably due to varying dimethyl sulfide emissions response to climate change (Table 9). In contrast, BC emissions or removal changes are quite consistent across models. Both sulfate and BC burden changes show comparable spread, however, as do changes in lifetimes. Sulfate lifetimes typically decrease while BC lifetimes typically increase, however. The decrease in sulfate lifetime is consistent with increases in

Radiative forcing in the ACCMIP

D. T. Shindell et al.

Title Page

Abstract	Introduction
Conclusions	References
Tables	Figures

| ◀◀ | ▶▶ |
| ◀ | ▶ |

| Back | Close |

Full Screen / Esc

Printer-friendly Version

Interactive Discussion

precipitation seen in most models (Lamarque et al., 2012b). Changes in lifetime reflect both the influence of climate change and the shifting spatial distribution of emissions (as lifetimes vary regionally).

6 Total anthropogenic composition forcing

We have analyzed the total forcing due to anthropogenic composition changes. For this analysis, we evaluate forcing relative to 1850 as this was used in the CMIP5 models. However, the earlier year 1750 is more clearly "preindustrial", although emissions inventories prior to 1850 were not prepared in support of AR5. This primarily influences WMGHG forcing, though some other species are also affected. Forcings for 1850 relative to 1750 have been estimated as 0.05 W m^{-2} for ozone (Lamarque et al., 2011), 0.04 W m^{-2} for BC albedo (Skeie et al., 2011a), and −0.02, 0.06, −0.03, −0.01 and −0.02 W m^{-2} for sulfate, BCff + bf, OAff+bf, nitrate and SOA, respectively (Skeie et al., 2011b).

The ACCMIP activity characterized radiative forcing from ozone as well as from aerosols. Ozone RF was calculated offline using the NCAR Community Climate System Model 4 radiative transfer model (RTM) and allowing for stratospheric temperatures to adjust (Conley et al., 2012). We compute the net longwave and shortwave all-sky flux at the tropopause (based on a climatology of tropopause pressure from the NCAR/NCEP reanalyses) using the same conditions for all parameters except for the ozone distribution. Results presented here are for ozone changes throughout the atmosphere rather than separating forcing into that due to changes above and below the tropopause. More detail on the ozone in the models is presented in Stevenson et al. (2012). That analysis shows that use of a different RTM to analyze the tropospheric ozone RF yields values that are 10 % higher that using the NCAR RTM, providing a rough estimate of uncertainty associated with the radiative transfer calculation. In addition, Young et al. (2012) show that the ACCMIP models generally capture the observed 1980 to 2000 total ozone column trends relatively well. Here we analyze the ozone RF from most of

the same models that provided ACCMIP aerosol simulations (GFDL-AM3, GISS-E2-R, HadGEM2, LMDzORINCA, MIROC-CHEM, NCAR-CAM3.5). These six represent all but two of the ACCMIP models for which CMIP5 simulations were also performed (Table 1). Uncertainties are presented as the standard deviation across models, as for aerosols. A comparison of the radiative impact of the present-day tropospheric ozone distributions in these six models versus that of the ozone observations from the Tropospheric Emission Spectrometer shows that these models have very small global mean biases, with a mean and standard deviation of $-0.020 \pm 0.031 \, \mathrm{W \, m^{-2}}$ instantaneous forcing (Bowman et al., 2012). While present-day biases do not necessarily reflect biases in the long-term behavior of ozone, to the best of our ability to evaluate them the models appear to produce realistic ozone in terms of the radiative impact of tropospheric ozone and long-term trends in stratospheric ozone.

As we do not expect there to be much variation between models in the RF due to WMGHGs, we have examined this in only two models: NCAR-CAM3.5 and GISS-E2-R for 2000 relative to 1850. We find that indeed, the spatial patterns of RF are quite similar. Hence we take the mean field from these two models as representative of the geographic distribution of RF from WMGHGs for all times, and scale the values uniformly so that the global mean matches the total RF due to WMGHGs prescribed in the historical period and under the RCPs. Uncertainty is assigned as 10 % of the RF (Forster et al., 2007).

The forcing due to WMGHGs is relatively homogeneous, with slightly greater values at subtropical latitudes in both hemispheres where clouds are less prevalent (Fig. 22). WMGHG forcing increases continually with time in the past and in the future under RCP 8.5, where it becomes especially large (in RCP 2.6 the global mean value is $3.1 \, \mathrm{W \, m^{-2}}$, but this decreases to $2.8 \, \mathrm{W \, m^{-2}}$ at 2100). In contrast, ozone forcing is positive between $\sim 45°\mathrm{S}$ and $90°\mathrm{N}$, but is negative over and near Antarctica from the 1980 to the 2030 timeslices. These negative values are due to the Antarctic ozone hole, which was not yet present in 1930 and has recovered by 2100. The positive forcing due to ozone, a GHG itself, maximizes in the subtropics similarly to the WMGHGs. Forcing

increases from 1850 through 2000, after which the trends differ sharply between the RCPs. Ozone forcing continues to rise under RCP 8.5 while it decreases to nearly its 1930 value by 2100 under the optimistic scenario RCP 2.6. Relative uncertainties for ozone are substantially larger than for WMGHGs, but are somewhat smaller than those for aerosols (Fig. 12). Note that analysis of the full set of ACCMIP models that simulated ozone changes (see Young et al. (2012); Stevenson et al. (2012)) with the same methodology used here gives a very similar 1850 to 2000 whole atmosphere ozone forcing with a global mean of $0.29 \pm 0.16\,\mathrm{W\,m^{-2}}$ as opposed to the $0.33 \pm 0.14\,\mathrm{W\,m^{-2}}$ found here and a nearly identical spatial pattern. Stevenson et al. (2012) also show that their ozone forcing results are only very weakly sensitive to changes in the set of models included (analyzing sets ranging from 4 to 17 models). Thus analysis of the subset of models that simulated both aerosols and ozone seems to provide a good estimate of ozone forcing as determined by the larger set of models.

We then created composite fields of WMGHG, ozone and aerosol forcing, using AF for aerosols and RF for WMGHGs and ozone. Though clearly it would be preferable to use the same metric for all forcing agents, in practice RF and AF are likely quite similar for both WMGHGs and ozone. Studies to date suggest that AF from WMGHGs may be slightly larger than RF, but that for both WMGHGs and ozone values are probably within 5 % (Hansen et al., 2005; Andrews and Forster, 2008; Lohmann et al., 2010). Though aerosol AF was not calculated for RCPs other than RCP 8.5, as noted previously nearly all the aerosol precursor emissions (other than NH_3; Lamarque et al., 2012b) are decreased dramatically by 2100 in all scenarios, so we regard the 2100 RCP8.5 aerosol AF as a good approximation to aerosol AF under the other scenarios as well.

Total anthropogenic composition forcing relative to 1850 shows positive global mean values throughout the historical period, but distinct regional differences (Fig. 23). The net forcing is strongly negative over many industrialized areas in 1980 as negative aerosol AF outweighs positive GHG forcing. Forcing due to WMGHGs rises very sharply in the late 20th century and pollution controls reduce the negative aerosol

forcing over Europe and North America from 1980 to 2000, so that by 2000 the net anthropogenic composition forcing is near zero over Europe and positive over most of North America (especially the west), while remaining strongly negative only over parts of East and Southeast Asia. The negative aerosol forcing over central Africa and northwestern South America visible in 1980 is still present in 2000, but the increased WMGHG forcing has offset it by that time. Moving into the future, net anthropogenic composition forcing remains negative over a shrinking portion of Southeast Asia by 2030 under RCP 8.5, and remains small over parts of Africa and South America with large amounts of biomass burning, and over Antarctica. Nearly everywhere else, however, forcing exceeds $2 \, W \, m^{-2}$, and in many parts of the world forcing is greater than $4 \, W \, m^{-2}$. By 2100 under RCP 8.5, WMGHG forcing is so large and aerosol forcing so small that there is relatively little spatial variation in the net anthropogenic composition forcing, which is between 6 and $10 \, W \, m^{-2}$ over most of the planet. Forcing at 2100 is much lower under the RCP 2.6 scenario, but as in the RCP 8.5 case it is dominated by WMGHGs and so is relatively uniform spatially. Forcing is between 2 and $5 \, W \, m^{-2}$ nearly everywhere except in some biomass burning regions, where forcing is near zero.

While a full timeseries of aerosol AF is not available, and our analysis showed that it is difficult to approximate AF based on other aerosol-related proxies, the available aerosol AF analyses is still informative. The timeseries shows that early in the 20th century, forcing from aerosols and ozone offset one another, so that the net anthropogenic composition forcing followed the WMGHG forcing (Fig. 23). As aerosol forcing grew, aerosols began to mask a considerable portion of the GHG (WMGHG + ozone) forcing. Since aerosol AF grew increasingly negative through 2000, the maximum masking in the ACCMIP models is at 2000 despite aerosol RF decreasing from 1980 to 2000. In the 21st century, aerosol masking is reduced and the net anthropogenic composition forcing again approaches the WMGHG forcing. Uncertainties are heavily influenced by aerosol forcing, so that relative uncertainties maximize in 1980, and are far larger in 1980, 2000 and 2030 than in 2100 (Table 10). Owing to the dominance of the WMGHG

forcing at 2100, the net forcing is fairly close to the RCP target values for all four RCP scenarios (Fig. 23; Table 10).

7 Surface temperature response

In the previous generation of climate models, there was a distinct correlation between the magnitude of negative aerosol forcing and climate sensitivity (Kiehl, 2007). A similar analysis for the CMIP5 subset of ACCMIP models shows that in this generation of models there is still a correlation between historical aerosol RF and equilibrium climate sensitivity (ECS; taken from Andrews et al., 2012; Bitz et al., 2012) and GISS-E2-R simulations) (Fig. 24). However, ECS is not particularly correlated with aerosol AF, which is the more relevant quantity as it drives the overall climate response.

Simulations to examine the influence of aerosols and ozone on climate were part of CMIP5, but were relegated to a low priority while most core simulations focused on CO_2. Hence to look at the effects of aerosols and ozone, we examine CMIP5 historical all forcings simulations minus historical WMGHG and historical natural (Nat) forcing simulations, as little data is available for historical aerosol or ozone simulations. The residual of historical minus (historical WMGHG plus historical Nat) includes not only aerosols and ozone, but also land-use changes, and we refer to this hereafter as anthropogenic non-WMGHG forcing (ANWF). For this analysis, we compare temperatures averaged over 1996–2005 (nominal 2000) and 1976–1985 (nominal 1980) with those during 1850–1859 (nominal 1850, though for two models the 1860s are used instead as simulations began only in 1860). Averages are taken over up to five available ensemble members, which leads to 3–5 realizations being included for all models other than MIROC-ESM-CHEM for which only one realization was available (30 years were used at each time for GFDL and LMD, 40 for HadGEM2, and 50 for CSIRO and GISS). Though WMGHG forcing was not diagnosed in CMIP5 simulations, forcing from WMGHGs has generally been consistent in models to within about 10 % (Collins et al., 2006; Forster et al., 2007). Thus assuming all models have a WMGHG forcing of

Full Screen / Esc

Printer-friendly Version

Interactive Discussion

2.30 W m^{-2} in 2000 introduces only small errors. We also assume all models have a spatial pattern of WMGHG that is similar to that described in the previous section, which again should be a good approximation.

We find that there is a substantial correlation between aerosol AF plus ozone RF and the global mean surface air temperature response to ANWF (Fig. 25). Similarly, the aerosol AF plus ozone RF times the approximate normalized climate sensitivity (the ECS/3.75, where 3.75 is the approximate forcing due to doubled CO_2) is often a reasonably good predictor of the global mean climate response to ANWF. In both cases, however, there are some models for which the response to ANWF does not closely track the aerosol AF plus ozone RF (or that value times the normalized climate sensitivity).

Based on the assumed WMGHG forcing and the simulated historical responses we find that transient climate response (TCR) to WMGHGs in these models varies by nearly a factor of two (Table 11). This is consistent with the range seen in analysis of the equilibrium climate sensitivity (Andrews et al., 2012), however the models' TCR does not closely track their ECS (Table 11). While the GISS-E2-R model has the lowest value of both TCR and ECS, the CSIRO-Mk3.6 model has almost the same TCR as GISS-E2-R but a much larger ECS, while the TCR is greatest in the GFDL-CM3 model, which has an ECS that is at the low end among the rest of the models examined here, and MIROC-CHEM has the greatest ECS but a lower TCR. Different ocean response times are the likely cause of these differences between TCR and ECS. Note that the AF and TCR are not well correlated (as was the case for AF and ECS).

Though the number of models is limited, the results suggest that the spread in modeled global mean climate sensitivity to aerosols is greater than for WMGHGs. While the latter varies by nearly a factor of two, the global mean response to ANWF appears to vary by a factor of 5 across these models. The results also suggest that the climate sensitivity to aerosols may be larger than to WMGHGs. The mean sensitivity (TCR) to WMGHGs is 0.64 °C per W m^{-2} assuming WMGHG forcing of 2.30 W m^{-2} at 2000. For those same models, the sensitivity to ANWF is 0.96 °C per W m^{-2}. The

RCP database includes estimates of historical land-use and stratospheric water vapor RFs of −0.17 and 0.07 W m^{-2}, respectively (the former is quite consistent with recent reconstructions (Pongratz et al., 2011)). Including these estimates in the ANWF, the sensitivity is still 0.84 °C per W m^{-2}. Furthermore, the sensitivity is much lower in the GISS-E2-R model, perhaps due in part to the strongly enhanced response to BC albedo forcing seen in that model (Koch et al., 2011a). In the other five models, the global sensitivity to WMGHGs is 0.67 °C per W m^{-2}, while the sensitivity to ANWF (including the estimated land-use forcing) is 0.95 °C per W m^{-2}. Thus there appears to be roughly 30–50 % greater sensitivity in most models to ANWF (which is primarily due to aerosols). In 5 of the 6 models, negative aerosol plus ozone forcing was greater in the NH extratropics than in the tropics or SH extratropics, and forcing in that area has been shown to cause an enhanced surface temperature response: ∼45 % in the GISS-E model even for idealized CO_2 perturbations (Shindell and Faluvegi, 2009). Hence the greater response to aerosol forcing appears to be largely a function of the aerosols being located primarily in the NH, where snow/ice albedo feedbacks are more prevalent (though a portion of the difference might also reflect different efficacies for the aerosol, ozone or land-use forcings).

We have also examined the responses over land and ocean separately. For the response to WMGHGs, the land response is roughly 66 % greater in all models (range 52–85 %). For ANWF, the land/ocean response ratio is much more varied, ranging from 15 % weaker to 250 % stronger (the land/ocean response is within 15 % of 1.0 in half the models, and roughly 2–2.5 in the other half, with no models having land/ocean responses in the 1.5–1.8 range seen for WMGHGs). Thus again it appears that the uneven distribution of forcing can have a large impact on the regional scale temperature response, and that the regional response to aerosols varies much more strongly across models than the response to WMGHGs. Though the strongest aerosol forcing is clearly located much more over land in some models (GFDL, LMDz) and much more over oceans in others (HadGEM2), this does not clearly relate to the pattern of response as LMDz has a much stronger land response while GFDL and HadGEM2

have stronger ocean responses (Table 11). Similarly, while forcing is often greatest over East and Southeast Asia or Europe, these regions do not clearly show the greatest response to ANWF. Locally, however, there are indications of response patterns sometimes following forcing, as in the HadGEM2 temperature response to ANWF that

5 shows local maxima in regions with strong pollution outflow from North America and Asia (Fig. 26). There are indications of similar responses in one or both of these outflow regions in the other models as well. There is also a robust response of warming in the North Atlantic consistent with an increase in the oceanic meridional overturning circulation. This change is opposite to the response seen in the WMGHG simulations, as

10 one would expect, but in both the CSIRO-Mk3.6 model and especially in the GISS-E2-R model the response per unit negative aerosol forcing seems to be stronger than the response per unit positive WMGHG forcing. It is unclear without additional experiments if this is simply a non-linear ocean response or is a function of the spatial distribution of the aerosol forcing.

15 The precise relationship between the spatial pattern of forcing and that of response has not yet been clearly determined. Local climate sensitivity varies strongly due to the presence of different feedbacks (e.g. snow/ice albedo, ocean circulation) and hence there is strong spatial inhomogeneity even in the response to WMGHG forcing (Fig. 26). At the largest spatial scales, all the models have an enhanced transient response in

20 the NH relative to the SH for 20th century increasing WMGHGs, which is attributable to the greater land area in the NH, which responds more rapidly to forcing, and the greater area with strong snow/ice albedo feedbacks (Table 11). In all models for which results were available, the enhancement of the NH relative to SH response is greater in the case of ANWF (results are similar looking at the ratio of the two extratropical

25 zones). The hemispheric asymmetry is 9 to 29 % stronger, with a mean value over all 6 models of 16 %. Hence it appears that the asymmetric distribution of forcing does play a significant role in hemispheric-scale temperature responses (though the basic climate sensitivity distribution plays an even larger role, as the multi-model mean hemispheric asymmetry in the response to quasi-uniform WMGHGs is 53 %). Examining the

Pearson correlation coefficient between the spatial patterns of forcing and response, we find that the correlation is always negative for WMGHGs (multi-model mean –0.3). This reflects the greater response at higher latitudes, where snow/ice albedo feedback is important, as opposed to the greater forcing being in relatively cloud-free subtropi-
5   cal latitudes with warm surface temperatures (Fig. 26). The correlation coefficient for aerosol AF + ozone RF versus ANWF response is again negative in some models, but is positive in others (multi-model mean –0.1). Hence there is not a high spatial coherence between forcing and response in either case, although there is a clear difference between the two sets of forcings.
10   Further insight into the relationship between forcing and response can be obtained by analysis of the spatial autocorrelations in the forcing and response fields. Prior analysis demonstrated that the autocorrelation can be a sensitive indicator of spatial relationships and specifically of spatial smoothing by comparing response and driving fields such as concentrations compared with emissions or temperature compared with
15   forcing (Shindell et al., 2010). As in prior work, we use circular spatial autocorrelation in which each grid point value is related to the mean value on circles around this grid point (where the circles for a given distance are equal area circles on the sphere). Autocorrelations are calculated after removing the mean and normalizing the field by its standard deviation to better discern spatial variations. The multi-model mean autocor-
20   relation of the surface temperature response to WMGHGs exceeds that of the response to ANWF out to distances of about 4000 km (Fig. 27; top left) although for both forcings the response has an enhanced autocorrelation relative to the driving forcing over this range (Fig. 27; bottom left). The enhancement indicates that physical processes have smoothed out the response relative to the forcing, so that forcings have a strong im-
25   pact out to about 6000–7000 km after which the response appears to be less closely related to the distribution of forcing. This length scale for temperature response to forcing is consistent with that seen in CMIP3 models (Shindell et al., 2010). Despite this smoothing, the weaker autocorrelation in the response to ANWF relative to WMGHGs demonstrates that the inhomogeneous nature of aerosol, ozone and land-use forcing

leads to a distinctly less homogeneous surface temperature response within ~4000 km of the forcing. At long distances (>6000 km), the response to ANWF has a greater autocorrelation than the response to WMGHGs due to the large scale anti-correlation between high latitude maxima in temperature responses and low latitude maxima in

5   WMGHG RF discussed previously.

Examining the enhancement of the autocorrelation in the response relative to the forcing for ANWF over 30°S–60°N, where most of the forcing is applied, shows a sharper peak in the typical length scale with the ensemble mean result indicating that localized forcing has a strong impact out to about 3000–3500 km after which there is a

10   marked decline (Fig. 27; top right). Separating land and ocean areas reveals that the length scale is shorter for land areas, as also seen in the previous analysis of CMIP3 models. We note that small values for the enhancement at short distances simply reflect the high inherent autocorrelation of the input forcing and so do not indicate weaker influence at short distances (Shindell et al., 2010). To better characterize this, we also

15   examine the enhancement of the autocorrelation of the response versus the forcing normalized by 1 minus the autocorrelation of the forcing. This is essence shows the enhancement achieved taking into account the maximum potential enhancement at a given length. For this analysis, we require that the autocorrelation of the forcing, which by definition is 1.0 at zero length, has decreased to at least 0.75 to avoid division by

20   small values that might reflect noise (which is in practice ~1000 km). The normalized enhancement shows that there is a steady decrease in the relationship between the spatial pattern of response with the driving forcing, with the ensemble mean length scale for a 1/e decrease being about 4000 km (Fig. 27; lower right). There is considerable variation across models, however, with the length scale for greatest impact of

25   localized forcings being around 2000–2500 km in two models, three models having results that are fairly similar to the ensemble mean, and one model showing minimal enhancement at any distance. Hence some models seem to have a somewhat shorter typical length of influence than the ensemble mean, though most are similar.

In addition to examining surface temperature changes over the 2000 to 1850 period, we also investigated the response from 1850 to 1980, when aerosol forcing peaked over many NH industrialized areas. The coupled models show a mixture of responses in their spatial patterns (Fig. 28). Locally enhanced responses over Europe, eastern North America and East Asia, where forcing was greatest (Fig. 20), are most clearly seen in the HadGEM2, GFDL-AM3, and GISS-E2-R models. Responses in CSIRO-Mk3.6 and MIROC-CHEM are also somewhat enhanced over Europe and East Asia, but North American temperature changes are mostly in the west while the forcing was mostly in the east. The response in the LMDz model is somewhat smoother, and indeed all models show some evidence that responses are not confined solely to areas with large forcing. Hence the models as a whole suggest that the very large aerosol forcings prior to pollution controls in eastern North America and Europe likely did contribute to mitigating the local warming due to WMGHGs, consistent with some prior results (Leibensperger et al., 2012), but that responses were not highly localized but rather spread over considerable area, again consistent with prior results (Shindell et al., 2010).

8 Conclusions

Our evaluation of the ACCMIP aerosol models against observations of AOD climatology and trends shows that most of the models perform reasonably well. The analysis included 8 models that also participated in CMIP5, and demonstrates that for that subset of CMIP5 models, many are also in reasonable agreement with observations although some appear to have too little aerosol. As there are a large number of models in CMIP5, however, aerosol forcing remains uncharacterized in many CMIP5 models.

In many of the ACCMIP models, nitrate and SOA are not included. Accounting for these missing components generally improves the agreement between models and observations of AOD. Furthermore, there is evidence from one model that forcing by SOA induced by land-use changes may be large, and from 2 models that nitrate may become

the largest aerosol RF component in the latter part of the 21st century, highlighting the need for more models to represent these processes.

We have shown that adjusted forcing can be used to provide a metric of aerosol effects that includes all aerosol-induced changes in clouds as well as direct aerosol effects. The relative variation in this metric across models is approximately equal to, or even less than, that in traditional aerosol RF at both global and regional scales. Comparison of aerosol AF and RF shows that the majority of aerosol forcing is indirect, indicating that RF alone provides a very incomplete portrayal of aerosol impacts. In addition, trends in these forcing are in opposite directions for some periods. In particular, during 1980 to 2000, aerosol RF becomes less negative while aerosol AF continues its historical trend becoming more negative. This behavior appears to be largely driven by disparate regional emissions trends: decreases in European and American emissions of sulfate precursors lead to less negative RF but increases in Asian emissions of both sulfate precursors and BC largely offset one another's RF while causing AF to become more negative primarily over Asia as sulfate appears to have a stronger impact on clouds than BC. This is consistent with sulfate being a far more abundant aerosol than BC, as well as a more soluble one, and with results presented here from one model showing that the AF/RF ratio is greater for sulfate than for BC (or OC). However, much more work is needed to characterize the AF of individual aerosol species. Hence currently it is not practical to adjust AF to account for missing components, further stressing the need for complete representations of aerosol types in models.

Our results suggest that while pollution controls in North American and Europe have reduced aerosol forcing, increases in Asian emissions have more than compensated so that globally there has not yet been an unmasking of WMGHG forcing via aerosol reductions. Instead, the continued increase in negative aerosol AF may have contributed to relative slow rates of global warming during recent years. The apparent underestimate of aerosols in several CMIP5 models suggests that they may underestimate future warming by not including a large enough unmasking trend.

A disadvantage of the AF metric is that it requires dedicated simulations at each point in time and cannot be diagnosed in transient simulations with multiple forcings the way RF can. AF was diagnosed at 2030 and 2100, however, and the models show a large reduction in negative AF over that time. With the pollution controls envisioned under the RCPs, the combined aerosol AF and ozone RF becomes 5 % or less of the total anthropogenic composition forcing in the latter part of the century. Hence the projected pollution controls would lead to a nearly complete unmasking of the full forcing by WMGHGs. Such a complete reduction in pollutant emissions may be overly optimistic, however, as current legislation certainly does not set the world on such a track (Shindell et al., 2012a; Pozzer et al., 2012).

Discussion Paper | Discussion Paper | Discussion Paper | Discussion Paper |

[ACPD](#)

12, 21105–21210, 2012

Radiative forcing in the ACCMIP

D. T. Shindell et al.

Title Page

Abstract	Introduction
Conclusions	References
Tables	Figures

◀ ▶

◀ ▶

| Back | Close |

Full Screen / Esc

Printer-friendly Version

Interactive Discussion

provided by the CCRT/GENCI computer center of the CEA. The CICERO-OsloCTM2 simulations were done within the projects SLAC (Short Lived Atmospheric Components) and EarthClim funded by the Norwegian Research Council. ACCMIP is organized under the auspices of Atmospheric Chemistry and Climate (AC&C), a project of International Global Atmospheric Chemistry (IGAC) and Stratospheric Processes And their Role in Climate (SPARC) under the International Geosphere-Biosphere Project (IGBP) and World Climate Research Program (WCRP).

References

Andrews, T. and Forster, P. M.: CO_2 forcing induces semi-direct effects with consequences for climate feedback interpretations, Geophys. Res. Lett., 35, L04802, doi:10.1029/2007gl032273, 2008.

Andrews, T., Gregory, J., Webb, M., and Taylor, K.: Forcing, feedbacks and climate sensitivity in CMIP5 coupled atmosphere-ocean climate models, Geophys. Res. Lett., 39, L09712, doi:10.1029/2012GL051607, 2012.

Bellouin, N., Jones, A., Haywood, J., and Christopher, S. A.: Updated estimate of aerosol direct radiative forcing from satellite observations and comparison against the Hadley Centre climate model, J. Geophys. Res., 113, doi:10.1029/2007JD009385, 2008.

Bellouin, N., Rae, J., Jones, A., Johnson, C., Haywood, J., and Boucher, O.: Aerosol forcing in the Climate Model Intercomparison Project (CMIP5) simulations by HadGEM2-ES and the role of ammonium nitrate, J. Geophys. Res.-Atmos., 116, D20206, doi:10.1029/2011JD016074, 2011.

Bitz, C., Shell, K., Gent, P., Bailey, D., Danabasoglu, G., Armour, K., Holland, M., and Kiehl, J.: Climate Sensitivity of the Community Climate System Model, Version 4, J. Climate, 25, 3053–3070, doi:10.1175/JCLI-D-11-00290.1, 2012.

Boer, G. J. and Yu, B.: Climate sensitivity and response, Clim. Dynam., 20, 415–429, doi:10.1007/s00382-002-0283-3, 2003.

Bowman, K. W., Shindell, D. T., Lamarque, J.-F., Young, P. J., de la Torre, M., Worden, H., Bergmann, D., Stevenson, D., Cameron-Smith, P., Collins, W. J., Doherty, R., Dalsoren, S., Eyring, V., Faluvegi, G., Folberth, G., Ghan, S. J., Horowitz, L. W., Josse, B., Lee, Y., McKenzie, I., Nagashima, T., Naik, V., Plummer, D., Rumbold, S., Skeie, R., Stevenson D. S.,

S. Strode, K. Sudo, S. Szopa, A.Voulgarakis and G. Zeng, A. Aghedo, Observational Constraints on radiative forcing from the Atmospheric Chemistry Climate Model Intercomparison Project (ACCMIP), Atmos. Chem. Phys. Disc., accepted, 2012.

Church, J., White, N., Konikow, L., Domingues, C., Cogley, J., Rignot, E., Gregory, J., van den Broeke, M., Monaghan, A., and Velicogna, I.: Revisiting the Earth's sea-level and energy budgets from 1961 to 2008, Geophys. Res. Lett., 38, L18601, doi:10.1029/2011GL048794, 2011.

Collins, W. J., Bellouin, N., Doutriaux-Boucher, M., Gedney, N., Halloran, P., Hinton, T., Hughes, J., Jones, C. D., Joshi, M., Liddicoat, S., Martin, G., O'Connor, F., Rae, J., Senior, C., Sitch, S., Totterdell, I., Wiltshire, A., and Woodward, S.: Development and evaluation of an Earth-System model – HadGEM2, Geosci. Model Dev., 4, 1051–1075, doi:10.5194/gmd-4-1051-2011, 2011.

Collins, W. D., Ramaswamy, V., Schwarzkopf, M. D., Sun, Y., Portmann, R. W., Fu, Q., Casanova, S. E. B., Dufresne, J. L., Fillmore, D. W., Forster, P. M. D., Galin, V. Y., Gohar, L. K., Ingram, W. J., Kratz, D. P., Lefebvre, M. P., Li, J., Marquet, P., Oinas, V., Tsushima, Y., Uchiyama, T., and Zhong, W. Y.: Radiative forcing by well-mixed greenhouse gases: Estimates from climate models in the Intergovernmental Panel on Climate Change (IPCC) Fourth Assessment Report (AR4), J. Geophys. Res.-Atmos., 111, D14317, doi:10.1029/2005jd006713, 2006.

Denman, K. L., Brasseur, G., Chidthaisong, A., Ciais, P., Cox, P. M., Dickinson, R. E., Hauglustaine, D., Heinze, C., Holland, E., Jacob, D., Lohmann, U., Ramachandran, S., Dias, P. L. d. S., Wofsy, S. C., and Zhang, X.: Couplings Between Changes in the Climate System and Biogeochemistry, in: Climate Change 2007: The Physical Science Basis. Contribution of Working Group I to the Fourth Assessment Report of the Intergovernmental Panel on Climate Change, Cambridge University Press, Cambridge, United Kingdom and New York, NY, USA, 2007.

Donner, L., Wyman, B., Hemler, R., Horowitz, L., Ming, Y., Zhao, M., Golaz, J., Ginoux, P., Lin, S., Schwarzkopf, M., Austin, J., Alaka, G., Cooke, W., Delworth, T., Freidenreich, S., Gordon, C., Griffies, S., Held, I., Hurlin, W., Klein, S., Knutson, T., Langenhorst, A., Lee, H., Lin, Y., Magi, B., Malyshev, S., Milly, P., Naik, V., Nath, M., Pincus, R., Ploshay, J., Ramaswamy, V., Seman, C., Shevliakova, E., Sirutis, J., Stern, W., Stouffer, R., Wilson, R., Winton, M., Wittenberg, A., and Zeng, F.: The Dynamical Core, Physical Parameterizations, and Basic

Title Page

Abstract	Introduction
Conclusions	References
Tables	Figures

|◀ ▶|

◀ ▶

Back | Close

Full Screen / Esc

Printer-friendly Version

Interactive Discussion

Simulation Characteristics of the Atmospheric Component AM3 of the GFDL Global Coupled Model CM3, J. Climate, 24, 3484–3519, doi:10.1175/2011JCLI3955.1, 2011.

Flanner, M. G., Zender, C. S., Randerson, J. T., and Rasch, P. J.: Present-day climate forcing and response from black carbon in snow, J. Geophys. Res., 112, D11202, doi:10.1029/2006JD008003, 2007.

Flanner, M. G., Zender, C. S., Hess, P. G., Mahowald, N. M., Painter, T. H., Ramanathan, V., and Rasch, P. J.: Springtime warming and reduced snow cover from carbonaceous particles, Atmos. Chem. Phys., 9, 2481–2497, doi:10.5194/acp-9-2481-2009, 2009.

Forster, P., Ramaswamy, V., Artaxo, P., Berntsen, T., Betts, R., Fahey, D. W., Haywood, J. L., J., Lowe, D. C., Myhre, G., Nganga, J., Prinn, R., Raga, G., Schulz, M., and Van Dorland, R.: Changes in Atmospheric Constituents and in Radiative Forcing, in: Climate Change 2007: The Physical Science Basis, edited by: Solomon, S., Cambridge University Press, New York, USA, 2007.

Fuglestvedt, J., Berntsen, T., Myhre, G., Rypdal, K., and Skeie, R. B.: Climate forcing from the transport sectors, Proc. Natl. Acad. Sci., 105, 454–458, 2008.

Geogdzhayev, I., Mishchenko, M., Terez, E., Terez, G., and Gushchin, G.: Regional advanced very high resolution radiometer-derived climatology of aerosol optical thickness and size, J. Geophys. Res.-Atmos., 110, D23205, doi:10.1029/2005JD006170, 2005.

Ghan, S. J., Liu, X., Easter, R. C., Rasch, P., and Yoon, J.-H.: Toward a Minimal Representation of Aerosol Direct, Semi-Direct and Indirect Effects: Comparative Decomposition, J. Climate, in press, 2012.

Gultepe, I. and Isaac, G. A.: Scale effects on averaging cloud droplet and aerosol number concentrations: observations and models, J. Clim., 12, 1268–1279, 1999.

Hansen, J., Sato, M., Ruedy, R., Nazarenko, L., Lacis, A., Schmidt, G. A., Russell, G., Aleinov, I., Bauer, M., Bauer, S., Bell, N., Cairns, B., Canuto, V., Chandler, M., Cheng, Y., Del Genio, A., Faluvegi, G., Fleming, E., Friend, A., Hall, T., Jackman, C., Kelley, M., Kiang, N. Y., Koch, D., Lean, J., Lerner, J., Lo, K., Menon, S., Miller, R. L., Minnis, P., Novakov, T., Oinas, V., Perlwitz, J., Perlwitz, J., Rind, D., Romanou, A., Shindell, D., Stone, P., Sun, S., Tausnev, N., Thresher, D., Wielicki, B., Wong, T., Yao, M., and Zhang, S.: Efficacy of Climate Forcings, J. Geophys. Res., 110, D18104, doi:10.1029/2005JD005776, 2005.

Hansen, J., Sato, M., Kharecha, P., and von Schuckmann, K.: Earth's energy imbalance and implications, Atmos. Chem. Phys., 11, 13421–13449, doi:10.5194/acp-11-13421-2011, 2011.

Holland, M., Bailey, D., Briegleb, B., Light, B., and Hunke, E.: Improved Sea Ice Shortwave Radiation Physics in CCSM4: The Impact of Melt Ponds and Aerosols on Arctic Sea Ice, J. Climate, 25, 1413–1430, doi:10.1175/JCLI-D-11-00078.1, 2012.

Kaufman, Y. and Koren, I.: Smoke and pollution aerosol effect on cloud cover, Science, 313, 655–658, doi:10.1126/science.1126232, 2006.

Kiehl, J.: Twentieth century climate model response and climate sensitivity, Geophys. Res. Lett., 34, doi:10.1029/2007GL031383, 2007.

Koch, D., Schulz, M., Kinne, S., McNaughton, C., Spackman, J. R., Balkanski, Y., Bauer, S., Berntsen, T., Bond, T. C., Boucher, O., Chin, M., Clarke, A., De Luca, N., Dentener, F., Diehl, T., Dubovik, O., Easter, R., Fahey, D. W., Feichter, J., Fillmore, D., Freitag, S., Ghan, S., Ginoux, P., Gong, S., Horowitz, L., Iversen, T., Kirkevåg, A., Klimont, Z., Kondo, Y., Krol, M., Liu, X., Miller, R., Montanaro, V., Moteki, N., Myhre, G., Penner, J. E., Perlwitz, J., Pitari, G., Reddy, S., Sahu, L., Sakamoto, H., Schuster, G., Schwarz, J. P., Seland, Ø., Stier, P., Takegawa, N., Takemura, T., Textor, C., van Aardenne, J. A., and Zhao, Y.: Evaluation of black carbon estimations in global aerosol models, Atmos. Chem. Phys., 9, 9001–9026, doi:10.5194/acp-9-9001-2009, 2009.

Koch, D., Bauer, S., Del Genio, A., Faluvegi, G., McConnell, J., Menon, S., Miller, R., Rind, D., Ruedy, R., Schmidt, G., and Shindell, D.: Coupled Aerosol-Chemistry-Climate Twentieth-Century Transient Model Investigation: Trends in Short-Lived Species and Climate Responses, J. Climate, 24, 2693–2714, doi:10.1175/2011JCLI3582.1, 2011a.

Koch, D., Bauer, S. E., Del Genio, A., Faluvegi, G., McConnell, J. R., Menon, S., Miller, R. L., Rind, D., Ruedy, R., Schmidt, G. A., and Shindell, D.: Coupled Aerosol-Chemistry-Climate Twentieth-Century Transient Model Investigation: Trends in Short-Lived Species and Climate Responses, J. Climate, 24, 2693–2714, doi:10.1175/2011JCLI3582.1, 2011b.

Lamarque, J., Kyle, G., Meinshausen, M., Riahi, K., Smith, S., van Vuuren, D., Conley, A., and Vitt, F.: Global and regional evolution of short-lived radiatively-active gases and aerosols in the Representative Concentration Pathways, Climatic Change, 109, 191–212, doi:10.1007/s10584-011-0155-0, 2011.

Lamarque, J.-F., Bond, T. C., Eyring, V., Granier, C., Heil, A., Klimont, Z., Lee, D., Liousse, C., Mieville, A., Owen, B., Schultz, M. G., Shindell, D., Smith, S. J., Stehfest, E., Van Aardenne, J., Cooper, O. R., Kainuma, M., Mahowald, N., McConnell, J. R., Naik, V., Riahi, K., and van Vuuren, D. P.: Historical (1850–2000) gridded anthropogenic and biomass burning emissions

of reactive gases and aerosols: methodology and application, Atmos. Chem. Phys., 10, 7017–7039, doi:10.5194/acp-10-7017-2010, 2010.

Lamarque, J.-F., Emmons, L. K., Hess, P. G., Kinnison, D. E., Tilmes, S., Vitt, F., Heald, C. L., Holland, E. A., Lauritzen, P. H., Neu, J., Orlando, J. J., Rasch, P. J., and Tyndall, G. K.: CAM-chem: description and evaluation of interactive atmospheric chemistry in the Community Earth System Model, Geosci. Model Dev., 5, 369–411, doi:10.5194/gmd-5-369-2012, 2012.

Lamarque, J.-F., Shindell, D. T., Josse, B., Eyring, V., Young, P. J., Cionni, I., Bergmann, D., Cameron-Smith, P., Collins, W. J., Doherty, R., Dalsoren, S., Faluvegi, G., Folberth, G., Ghan, S. J., Horowitz, L. W., Lee, Y., McKenzie, I., Nagashima, T., Naik, V., Plummer, D., Rumbold, A., Skeie, R., Stevenson, D. S., Strode, S., Sudo, K., Szopa, S., Voulgarakis, A., and Zeng, G.: The Atmospheric Chemistry and Climate Model Intercomparison Project (AC-CMIP): Overview and description of models, simulations and climate diagnostics, Atmos. Chem. Phys. Disc., 2012b.

Lawrence, D., Oleson, K., Flanner, M., Thornton, P., Swenson, S., Lawrence, P., Zeng, X., Yang, Z., Levis, S., Sakaguchi, K., Bonan, G., and Slater, A.: Parameterization Improvements and Functional and Structural Advances in Version 4 of the Community Land Model, Journal of Advances in Modeling Earth Systems, 3, M03001, doi:10.1029/2011MS000045, 2011.

Lawrence, D., Oleson, K., Flanner, M., Fletcher, C., Lawrence, P., Levis, S., Swenson, S., and Bonan, G.: The CCSM4 Land Simulation, 1850–2005: Assessment of Surface Climate and New Capabilities, J. Climate, 25, 2240–2260, doi:10.1175/JCLI-D-11-00103.1, 2012.

Lee, Y. H. and Adams, P. J.: Evaluation of aerosol distributions in the GISS-TOMAS global aerosol microphysics model with remote sensing observations, Atmos. Chem. Phys., 10, 2129–2144, doi:10.5194/acp-10-2129-2010, 2010.

Lee, Y., J.-F. Lamarque, M. Flanner, C. Jiao, D. T. Shindell, W. J. Collins, St. Dalsoren, S. J. Ghan, L. Horowitz, G. Myhre, T. Nagashima, V. Naik, S. Rumbold, R. Skeie, K. Sudo, T. Takemura, J. McConnell, M. Bisiaux, R. Edwards, J. J. Cao, F. Thevenon, Evaluation of preindustrial to present-day black carbon and its albedo forcing from ACCMIP (Atmospheric Chemistry and Climate Model Intercomparison Project), Atmos. Chem. Phys. Disc., accepted, 2012.

Leibensperger, E. M., Mickley, L. J., Jacob, D. J., Chen, W.-T., Seinfeld, J. H., Nenes, A., Adams, P. J., Streets, D. G., Kumar, N., and Rind, D.: Climatic effects of 1950–2050 changes in US anthropogenic aerosols – Part 2: Climate response, Atmos. Chem. Phys., 12, 3349–3362, doi:10.5194/acp-12-3349-2012, 2012.

Radiative forcing in the ACCMIP

D. T. Shindell et al.

Title Page

Abstract	Introduction
Conclusions	References
Tables	Figures

|◀   ▶|

◀   ▶

Back   Close

Full Screen / Esc

Printer-friendly Version

Interactive Discussion

Li, Z., Zhao, X., Kahn, R., Mishchenko, M., Remer, L., Lee, K.-H., Wang, M., Laszlo, I., Naka-jima, T., and Maring, H.: Uncertainties in satellite remote sensing of aerosols and impact on monitoring its long-term trend: a review and perspective, Ann. Geophys., 27, 2755–2770, doi:10.5194/angeo-27-2755-2009, 2009.

Libardoni, A. and Forest, C.: Sensitivity of distributions of climate system properties to the surface temperature dataset, Geophys. Res. Lett., 38, D03204, doi:10.1029/2011GL049431, 2011.

Liu, X., Penner, J., and Wang, M.: Influence of anthropogenic sulfate and black carbon on upper tropospheric clouds in the NCAR CAM3 model coupled to the IMPACT global aerosol model, J. Geophys. Res.-Atmos., 114, D04204, doi:10.1029/2008JD010492, 2009.

Liu, X., Easter, R. C., Ghan, S. J., Zaveri, R., Rasch, P., Shi, X., Lamarque, J.-F., Gettel-man, A., Morrison, H., Vitt, F., Conley, A., Park, S., Neale, R., Hannay, C., Ekman, A. M. L., Hess, P., Mahowald, N., Collins, W., Iacono, M. J., Bretherton, C. S., Flanner, M. G., and Mitchell, D.: Toward a minimal representation of aerosols in climate models: description and evaluation in the Community Atmosphere Model CAM5, Geosci. Model Dev., 5, 709–739, doi:10.5194/gmd-5-709-2012, 2012.

Lohmann, U., Rotstayn, L., Storelvmo, T., Jones, A., Menon, S., Quaas, J., Ekman, A. M. L., Koch, D., and Ruedy, R.: Total aerosol effect: radiative forcing or radiative flux perturbation?, Atmos. Chem. Phys., 10, 3235–3246, doi:10.5194/acp-10-3235-2010, 2010.

Meinshausen, M., Raper, S. C. B., and Wigley, T. M. L.: Emulating coupled atmosphere-ocean and carbon cycle models with a simpler model, MAGICC6 – Part 1: Model description and calibration, Atmos. Chem. Phys., 11, 1417–1456, doi:10.5194/acp-11-1417-2011, 2011.

Ming, Y. and Ramaswamy, V.: Nonlinear Climate and Hydrological Responses to Aerosol Ef-fects, J. Climate, 22, 1329–1339, doi:10.1175/2008jcli2362.1, 2009.

Murphy, D. M., Solomon, S., Portmann, R. W., Rosenlof, K. H., Forster, P. M., and Wong, T.: An observationally based energy balance for the Earth since 1950, J. Geophys. Res., 114, D17107, doi:10.1029/2009JD012105, 2009.

Penner, J. E., Chen, Y., Wang, M., and Liu, X.: Possible influence of anthropogenic aerosols on cirrus clouds and anthropogenic forcing, Atmos. Chem. Phys., 9, 879–896, doi:10.5194/acp-9-879-2009, 2009.

Pongratz, J., Raddatz, T., Reick, C. H., Esch, M., and Claussen, M.: Radiative forcing from anthropogenic land cover change since AD 800, Geophys. Res. Lett., 36, L02709, doi:10.1029/2008GL036394, 2009.

Title Page

Abstract | Introduction

Conclusions | References

Tables | Figures

◀ | ▶

◀ | ▶

Back | Close

Full Screen / Esc

Printer-friendly Version

Interactive Discussion

Pozzer, A., Zimmermann, P., Doering, U.M., van Aardenne, J., Tost, H., Dentener, F., Janssens-Maenhout, G., and Lelieveld, J.: Effects of business-as-usual anthropogenic emissions on air quality, Atmos. Chem. Phys., 12, 6915–6937, doi:10.5194/acp-12-6915-2012, 2012.

Qian, T., Dai, A., Trenberth, K., and Oleson, K.: Simulation of global land surface conditions from 1948 to 2004. Part I: Forcing data and evaluations, J. Hydrometeorol., 7, 953–975, doi:10.1175/JHM540.1, 2006.

Quaas, J., Ming, Y., Menon, S., Takemura, T., Wang, M., Penner, J. E., Gettelman, A., Lohmann, U., Bellouin, N., Boucher, O., Sayer, A. M., Thomas, G. E., McComiskey, A., Feingold, G., Hoose, C., Kristjánsson, J. E., Liu, X., Balkanski, Y., Donner, L. J., Ginoux, P. A., Stier, P., Grandey, B., Feichter, J., Sednev, I., Bauer, S. E., Koch, D., Grainger, R. G., Kirkevåg, A., Iversen, T., Seland, Ø., Easter, R., Ghan, S. J., Rasch, P. J., Morrison, H., Lamarque, J.-F., Iacono, M. J., Kinne, S., and Schulz, M.: Aerosol indirect effects – general circulation model intercomparison and evaluation with satellite data, Atmos. Chem. Phys., 9, 8697–8717, doi:10.5194/acp-9-8697-2009, 2009.

Remer, L., Kaufman, Y., Tanre, D., Mattoo, S., Chu, D., Martins, J., Li, R., Ichoku, C., Levy, R., Kleidman, R., Eck, T., Vermote, E., and Holben, B.: The MODIS aerosol algorithm, products, and validation, J. Atmos. Sci., 62, 947–973, doi:10.1175/JAS3385.1, 2005.

Rotstayn, L. D. and Lohmann, U.: Tropical rainfall trends and the indirect aerosol effect, J. Climate, 15, 2103–2116, doi:10.1175/1520-0442(2002)015<2103:trtati>2.0.co;2, 2002.

Rotstayn, L. D., Jeffrey, S. J., Collier, M. A., Dravitzki, S. M., Hirst, A. C., Syktus, J. I., and Wong, K. K.: Aerosol-induced changes in summer rainfall and circulation in the Australasian region: a study using single-forcing climate simulations, Atmos. Chem. Phys. Discuss., 12, 5107–5188, doi:10.5194/acpd-12-5107-2012, 2012.

Ruckstuhl, C., Norris, J., and Philipona, R.: Is there evidence for an aerosol indirect effect during the recent aerosol optical depth decline in Europe?, J. Geophys. Res.-Atmos., 115, 4699, doi:10.1029/2009JD012867, 2010.

Schulz, M., Textor, C., Kinne, S., Balkanski, Y., Bauer, S., Berntsen, T., Berglen, T., Boucher, O., Dentener, F., Guibert, S., Isaksen, I. S. A., Iversen, T., Koch, D., Kirkevåg, A., Liu, X., Montanaro, V., Myhre, G., Penner, J. E., Pitari, G., Reddy, S., Seland, Ø., Stier, P., and Takemura, T.: Radiative forcing by aerosols as derived from the AeroCom present-day and pre-industrial simulations, Atmos. Chem. Phys., 6, 5225-5246, doi:10.5194/acp-6-5225-2006, 2006.

Sekiguchi, M., Nakajima, T., Suzuki, K., Kawamoto, K., Higurashi, A., Rosenfeld, D., Sano, I., and Mukai, S.: A study of the direct and indirect effects of aerosols using global

Title Page

Abstract | Introduction

Conclusions | References

Tables | Figures

◄ | ►

◄ | ►

Back | Close

Full Screen / Esc

Printer-friendly Version

Interactive Discussion

satellite data sets of aerosol and cloud parameters, J. Geophys. Res.-Atmos., 108, 4699, doi:10.1029/2002JD003359, 2003.

Shindell, D. and Faluvegi, G.: Climate response to regional radiative forcing during the 20th century, Nature Geosci., 2, 294–300, 2009.

5 Shindell, D., Lamarque, J.-F., Unger, N., Koch, D., Faluveg, G., Bauer, S., and Teich, H.: Climate forcing and air quality change due to regional emissions reductions by economic sector, Atmos. Chem. Phys. Discuss., 8, 11609–11642, doi:10.5194/acpd-8-11609-2008, 2008.

Shindell, D., Schulz, M., Ming, Y., Takemura, T., Faluvegi, G., and Ramaswamy, V.: Spatial scales of climate response to inhomogeneous radiative forcing, J. Geophys. Res., 115, D19110, doi:10.1029/2010JD014108, 2010.

Shindell, D., Kuylenstierna, J. C. I., Vignati, E., van Dingenen, R., Amann, M., Klimont, Z., Anenberg, S. C., Muller, N., Janssens-Maenhout, G., Raes, F., Schwartz, J., Faluvegi, G., Pozzoli, L., Kupiainen, K., Hoeglund-Isaksson, L., Emberson, L., Streets, D., Ramanathan, V., Hicks, K., Oanh, N. T. K., Milly, G., Williams, M., Demkine, V., and Fowler, D.: Simultaneously Mitigating Near-Term Climate Change and Improving Human Health and Food Security, Science, 335, 183–189, doi:10.1126/science.1210026, 2012a.

Shindell, D. T., Pechony, O., Voulgarakis, A., Faluvegi, G., Nazarenko, L., Lamarque, J.-F., Bowman, K., Milly, G., Kovari, B., Ruedy, R., and Schmidt, G.: Interactive ozone and methane chemistry in GISS-E2 historical and future climate simulations, Atmos. Chem. Phys., in review, 2012b.

Skeie, R. B., Berntsen, T., Myhre, G., Pedersen, C. A., Ström, J., Gerland, S., and Ogren, J. A.: Black carbon in the atmosphere and snow, from pre-industrial times until present, Atmos. Chem. Phys., 11, 6809–6836, doi:10.5194/acp-11-6809-2011, 2011a.

Skeie, R. B., Berntsen, T. K., Myhre, G., Tanaka, K., Kvalevåg, M. M., and Hoyle, C. R.: Anthropogenic radiative forcing time series from pre-industrial times until 2010, Atmos. Chem. Phys., 11, 11827–11857, doi:10.5194/acp-11-11827-2011, 2011b.

Stevenson, D. S., P. J. Young, V. Naik, J.-F. Lamarque, D. T. Shindell, R. Skeie, S. Dalsoren, G. Myhre, T. Berntsen, G. Folberth, S. Rumbold, W. J. Collins, I. A. MacKenzie, R. M. Doherty, G. Zeng, T. van Noije, A. Strunk, D. Bergmann, P. Cameron-Smith, D. Plummer, S. A. Strode, L. Horowitz, Y. Lee, S. Szopa, K. Sudo, T. Nagashima, B. Josse, I. Cionni, M. Righi, V. Eyring, O. Wild, K. W. Bowman, Tropospheric ozone changes and radiative forcing 1850-2100 in the Atmospheric Chemistry and Climate Model Inter-comparison Project (ACCMIP), Atmos. Chem. Phys. Disc., 2012.

Title Page

Abstract	Introduction
Conclusions	References
Tables	Figures

◄◄ ►►

◄ ►

| Back | Close |

Full Screen / Esc

Printer-friendly Version

Interactive Discussion

Taylor, K. E., Stouffer, R. J., and Meehl, G. A.: An Overview of CMIP5 and the experiment design, B. Am. Meteorol. Soc., 93, 485–498, doi:10.1175/BAMS-D-11-00094.1, 2012.

Textor, C., Schulz, M., Guibert, S., Kinne, S., Balkanski, Y., Bauer, S., Berntsen, T., Berglen, T., Boucher, O., Chin, M., Dentener, F., Diehl, T., Easter, R., Feichter, H., Fillmore, D., Ghan, S., Ginoux, P., Gong, S., Grini, A., Hendricks, J., Horowitz, L., Huang, P., Isaksen, I., Iversen, I., Kloster, S., Koch, D., Kirkevåg, A., Kristjansson, J. E., Krol, M., Lauer, A., Lamarque, J. F., Liu, X., Montanaro, V., Myhre, G., Penner, J., Pitari, G., Reddy, S., Seland, Ø., Stier, P., Takemura, T., and Tie, X.: Analysis and quantification of the diversities of aerosol life cycles within AeroCom, Atmos. Chem. Phys., 6, 1777–1813, doi:10.5194/acp-6-1777-2006, 2006.

Torres, O., Tanskanen, A., Veihelmann, B., Ahn, C., Braak, R., Bhartia, P., Veefkind, P., and Levelt, P.: Aerosols and surface UV products from Ozone Monitoring Instrument observations: An overview, J. Geophys. Res.-Atmos., 112, D24S47, doi:10.1029/2007JD008809, 2007.

Unger, N., Bond, T. C., Wang, J. S., Koch, D. M., Menon, S., Shindell, D. T., and Bauer, S.: Attribution of climate forcing to economic sectors, Proc. Natl. Acad. Sci., 107, 3382–3387, 2010.

UNEP/WMO (United Nations Environment Programme and World Meterological Organization): Integrated Assessment of Black Carbon and Tropospheric Ozone, Nairobi, Kenya, 2011.

van Vuuren, D. P., Edmonds, J., Kainuma, M., Riahi, K., Thomson, A., Hibbard, K., Hurtt, G. C., Kram, T., Krey, V., Lamarque, J. F., Masui, T., Meinshausen, M., Nakicenovic, N., Smith, S. J., and Rose, S. K.: The representative concentration pathways: an overview, Climatic Change, 109, 5–31, 2011.

Watanabe, S., Hajima, T., Sudo, K., Nagashima, T., Takemura, T., Okajima, H., Nozawa, T., Kawase, H., Abe, M., Yokohata, T., Ise, T., Sato, H., Kato, E., Takata, K., Emori, S., and Kawamiya, M.: MIROC-ESM 2010: model description and basic results of CMIP5-20c3m experiments, Geosci. Model Dev., 4, 845–872, doi:10.5194/gmd-4-845-2011, 2011.

Young, P. J., A. T. Archibald, K. Bowman, V. Eyring, B. Josse, J.-F. Lamarque, V. Naik, D. S. Stevenson, S. Tilmes, A. Voulgarikis, O. Wild, D. Bergmann, P. Cameron-Smith, I. Cionni, W. J. Collins, R. Doherty, S. Dalsoren, G. Faluvegi, G. Folberth, L. W. Horowitz, Y. Lee, I. McKenzie, T. Nagashima, D. Plummer, S. Rumbold, R. Skeie, D. T. Shindell, S. Strode, K. Sudo, S.

21169

Szopa, S., Balkanski, Y., Schulz, M., Bekki, S., Cugnet, D., Fortems-Cheiney, A., Turquety, S., Cozic, A., Deandreis, C., Hauglustaine, D., Idelkadi, A., Lathiere, J., Lefevre, F., Marchand, M., Vuolo, R., Yan, N., and Dufresne, J. L., Aerosol and Ozone changes as forcing for Climate Evolution between 1850 and 2100, Clim. Dyn., in press, 2012.

5   Taylor, K. E., Stouffer, R. J., and Meehl, G. A.: An Overview of CMIP5 and the experiment design, B. Am. Meteorol. Soc., 93, 485–498, doi:10.1175/BAMS-D-11-00094.1, 2012.

Textor, C., Schulz, M., Guibert, S., Kinne, S., Balkanski, Y., Bauer, S., Berntsen, T., Berglen, T., Boucher, O., Chin, M., Dentener, F., Diehl, T., Easter, R., Feichter, H., Fillmore, D., Ghan, S., Ginoux, P., Gong, S., Grini, A., Hendricks, J., Horowitz, L., Huang, P., Isaksen, I., Iversen,

10   I., Kloster, S., Koch, D., Kirkevåg, A., Kristjansson, J. E., Krol, M., Lauer, A., Lamarque, J. F., Liu, X., Montanaro, V., Myhre, G., Penner, J., Pitari, G., Reddy, S., Seland, Ø., Stier, P., Takemura, T., and Tie, X.: Analysis and quantification of the diversities of aerosol life cycles within AeroCom, Atmos. Chem. Phys., 6, 1777–1813, doi:10.5194/acp-6-1777-2006, 2006.

Torres, O., Tanskanen, A., Veihelmann, B., Ahn, C., Braak, R., Bhartia, P., Veefkind, P., and Lev-

15   elt, P.: Aerosols and surface UV products from Ozone Monitoring Instrument observations: An overview, J. Geophys. Res.-Atmos., 112, D24S47, doi:10.1029/2007JD008809, 2007.

Unger, N., Bond, T. C., Wang, J. S., Koch, D. M., Menon, S., Shindell, D. T., and Bauer, S.: Attribution of climate forcing to economic sectors, Proc. Natl. Acad. Sci., 107, 3382–3387, 2010.

20   UNEP/WMO (United Nations Environment Programme and World Meterological Organization): Integrated Assessment of Black Carbon and Tropospheric Ozone, Nairobi, Kenya, 2011.

van Vuuren, D. P., Edmonds, J., Kainuma, M., Riahi, K., Thomson, A., Hibbard, K., Hurtt, G. C., Kram, T., Krey, V., Lamarque, J. F., Masui, T., Meinshausen, M., Nakicenovic, N., Smith, S. J., and Rose, S. K.: The representative concentration pathways: an overview, Climatic Change,

25   109, 5–31, 2011.

Watanabe, S., Hajima, T., Sudo, K., Nagashima, T., Takemura, T., Okajima, H., Nozawa, T., Kawase, H., Abe, M., Yokohata, T., Ise, T., Sato, H., Kato, E., Takata, K., Emori, S., and Kawamiya, M.: MIROC-ESM 2010: model description and basic results of CMIP5-20c3m experiments, Geosci. Model Dev., 4, 845–872, doi:10.5194/gmd-4-845-2011, 2011.

30   Young, P. J., A. T. Archibald, K. Bowman, V. Eyring, B. Josse, J.-F. Lamarque, V. Naik, D. S. Stevenson, S. Tilmes, A. Voulgarikis, O. Wild, D. Bergmann, P. Cameron-Smith, I. Cionni, W. J. Collins, R. Doherty, S. Dalsoren, G. Faluvegi, G. Folberth, L. W. Horowitz, Y. Lee, I. McKenzie, T. Nagashima, D. Plummer, S. Rumbold, R. Skeie, D. T. Shindell, S. Strode, K. Sudo, S.

Title Page

Abstract | Introduction

Conclusions | References

Tables | Figures

◄ | ►

◄ | ►

Back | Close

Full Screen / Esc

Printer-friendly Version

Interactive Discussion

Szopa and G. Zeng, Pre-industrial to end 21st century projections of tropospheric ozone from the Atmospheric Chemistry and Climate Model Intercomparison Project (ACCMIP), Atmos. Chem. Phys. Disc., 2012.

Yu, H., Chin, M., Remer, L., Kleidman, R., Bellouin, N., Bian, H., and Diehl, T.: Variability of marine aerosol fine-mode fraction and estimates of anthropogenic aerosol component over cloud-free oceans from the Moderate Resolution Imaging Spectroradiometer (MODIS), J. Geophys. Res.-Atmos., 114, D10206, doi:10.1029/2008JD010648, 2009.

Zhang, H., Shen, Z., Wei, X., Zhang, M., and Li, Z.: Comparison of optical properties of nitrate and sulfate aerosol and the direct radiative forcing due to nitrate in China, Atmos. Res., 113, 113–125, 2012.

Zhao, T., Laszlo, I., Guo, W., Heidinger, A., Cao, C., Jelenak, A., Tarpley, D., and Sullivan, J.: Study of long-term trend in aerosol optical thickness observed from operational AVHRR satellite instrument, J. Geophys. Res.-Atmos., 113, 10.1029/2007JD009061, 2008.

Printer-friendly Version

Interactive Discussion

Table 1. Aerosol components included and simulations performed by the ACCMIP models.

Model	Aerosol components included[1]							Used in O_3 RF	CMIP5 runs similar model	Historical				RCP 2.6		RCP 4.5/6.0	RCP 8.5		Primary references
	BC	OC	dust	nitrate	sulfate	SOA	Sea-salt			1850	1930	1980	2000	2030	2100	2010	2030	2100	
CICERO-OsloCTM2	x	x	a	x	x	x	a		None	♦	♦	♦	♦	♦	♦	♦	♦	♦	(Skeie et al., 2011b)
CSIRO-Mk3.6	x	x	a		x	x	a		CSIRO-Mk3.6	♦	♦	♦	♦					♦	(Rotstayn et al., 2012)
GFDL-AM3	x	x	x		x		x	♦	GFDL-CM3	♦		♦	♦	♦	♦	♦	♦	♦	(Donner et al., 2011)(Naik et al., in preparation)
GISS-E2-R	x	x	x	x	x	x	x	♦	GISS-E2-R	♦	♦	♦	♦	♦	♦	♦	♦	♦	(Shindell et al., 2012b)
GISS-E2-R-TOMAS	x	x	x		x		a	♦	None	♦	♦	♦	♦						(Lee and Adams, 2010)
HadGEM2	x	x	a	x[2]	x	x	x	♦	HadGEM2-ES	♦		♦	♦		♦			♦	(Collins et al., 2011)
LMDzORINCA	x	x	a		x		a	♦	IPSL-CM5A-LR	♦	♦	♦	♦	♦	♦	♦	♦	♦	(Szopa et al, 2012)
MIROC-CHEM	x	x	x	x[3]	x	x[3]	x	♦	MIROC-ESM-CHEM	♦	♦	♦	♦	♦	♦	♦	♦	♦	(Watanabe et al., 2011)
NCAR-CAM3.5	x	x	a		x		a	♦	NCAR-CCSM4	♦	♦	♦	♦	♦	♦		♦	♦	(Lamarque et al., 2012a)
NCAR-CAM5.1	x	x	x		x	x	x		CESM1-CAM5.1-FV2	♦	♦	♦	♦						(Liu et al., 2012); (Ghan et al., 2012)

Biases are the normalized mean bias (in percent).

[1] x indicates included in AOD and forcing, a indicates included in AOD but not in forcing.

[2] HadGEM2 simulations for ACCMIP (&CMIP5) did not include dust or nitrate forcing, but nitrate was calculated in Bellouin et al., 2011, and those results have been included here when available (AOD and forcing).

[3] MIROC-CHEM nitrate and SOA were calculated, but not used for their CMIP5 simulations. AOD diagnostics for these two components were not available, but forcings were.

Table 2. Annual average AOD (550 nm) compared with observations.

Model	R vs. MODIS	R vs. MISR	R vs. SurfObs	Bias vs. MODIS	Bias vs. MISR	Bias vs. SurfObs
CICERO-OsloCTM2	0.71	0.76	0.69	12	6	25
CSIRO-Mk3.6	0.71	0.71	N/A	7	4	N/A
CSIRO-Mk3.6-cs	0.68	0.68	N/A	17	13	N/A
GFDL-AM3	0.69	0.73	0.51	2	−5	15
GISS-E2-R	0.56	0.63	0.56	53	46	77
GISS-E2-R-cs	0.62	0.71	0.61	−14	−17	−8
GISS-E2-R-TOMAS*	0.59	0.71	0.56	−21	−20	19
HadGEM2	0.66	0.69	0.65	−3	−9	−2
LMDzORINCA	0.70	0.68	0.54	−20	−23	−5
MIROC-CHEM	0.55	0.63	0.44	−30	−33	−22
NCAR-CAM3.5	0.70	0.71	0.58	−28	−31	−13
NCAR-CAM5.1	0.50	0.54	0.56	−24	−24	−22
10 Model mean	0.64	0.68	0.57	−11	−14	−1
Absolute biases				24	26	16

The suffix cs indicates clear-sky. Averages in the bottom two rows use only the clear-sky versions of model diagnostics (and exclude all-sky from those models). GISS-E2-R-TOMAS results were virtually identical for all-sky and clear-sky. Biases are the normalized mean bias (in percent), and absolute biases are the average absolute value of the area-weighted biases.

Table 3. Comparison of models with MODIS fine mode AOD over all areas and over ocean areas.

Model	R	Bias	R ocean	Bias ocean
CICERO-OsloCTM2	0.52	28	0.71	−1
GFDL-AM3	0.56	50	0.72	17
GISS-E2-R-cs	0.50	4	0.68	−15
GISS-E2-RTOMAS	0.57	−52	0.73	−65
HadGEM2	0.48	−43	0.70	−57
LMDzORINCA	0.48	6	0.77	−19
MIROC-CHEM	0.38	−60	0.53	−66
NCAR-CAM3.5	0.52	−20	0.70	−33
NCAR-CAM5.1	0.39	74	0.41	58

Biases are the normalized mean bias (in percent).

Table 4. Evaluation of model AOD in comparison with satellite observations sorted by locations dominated by sulfate, OA, dust and sea-salt.

top decile of sulfate mass density

	Versus MISR			Versus MODIS			Global mean AOD
Model	bias	lmnb	lmne	bias	lmnb	lmne	
CICERO-OsloCTM2	0.09	0.14	0.15	0.07	0.12	0.16	0.058
GFDL-AM3	0.05	0.10	0.15	0.06	0.11	0.17	0.065
GISS-E2-R-cs	−0.01	−0.02	0.11	−0.04	−0.05	0.14	0.023
GISS-E2-R-TOMAS-cs	0.05	−0.02	0.18	0.01	−0.08	0.20	0.020
HadGEM2	0.00	−0.01	0.11	−0.01	−0.01	0.12	0.024
MIROC-CHEM	−0.06	−0.12	0.18	−0.07	−0.14	0.20	0.026
NCAR-CAM3.5	−0.02	−0.03	0.11	−0.04	−0.04	0.13	0.047
NCAR-CAM5.1	0.00	−0.04	0.16	−0.06	−0.12	0.20	0.014

top decile of OA mass density

Model	bias	lmnb	lmne	bias	lmnb	lmne	AOD
CICERO-OsloCTM2	0.03	0.04	0.11	0.03	0.06	0.13	0.013
GFDL-AM3	0.05	0.07	0.12	0.05	0.09	0.14	0.031
GISS-E2-R-cs	−0.05	−0.11	0.16	−0.05	−0.09	0.18	0.009
GISS-E2-R-TOMAS-cs	0.00	−0.17	0.29	0.00	−0.15	0.28	0.010
HadGEM2	0.02	0.00	0.12	0.01	−0.01	0.14	0.002
MIROC-CHEM	−0.12	−0.28	0.29	−0.12	−0.26	0.28	0.014
NCAR-CAM3.5	−0.10	−0.23	0.26	−0.10	−0.23	0.25	0.004
NCAR-CAM5.1	−0.07	−0.17	0.22	−0.08	−0.16	0.24	0.019

Table 4. Continued.

top decile of dust mass density							
	Versus MISR			Versus MODIS			Global mean AOD
Model	bias	lmnb	lmne	bias	lmnb	lmne	
GFDL-AM3	−0.02	−0.03	0.10	−0.02	−0.02	0.13	0.014
GISS-E2-R-cs	−0.01	−0.02	0.12	−0.05	−0.07	0.18	0.018
GISS-E2-R-TOMAS-cs	0.13	0.10	0.16	0.05	0.01	0.20	0.039
MIROC-CHEM	−0.05	−0.10	0.13	−0.08	−0.14	0.18	0.021
NCAR-CAM3.5	−0.03	−0.05	0.11	−0.06	−0.08	0.14	0.026
NCAR-CAM5.1	0.03	0.03	0.15	−0.03	−0.05	0.20	0.018
top decile of sea-salt mass density							
CICERO-OsloCTM2	0.04	0.09	0.10	0.05	0.13	0.13	0.061
GFDL-AM3	−0.02	−0.05	0.06	0.00	0.00	0.04	0.043
GISS-E2-R-cs	−0.02	−0.06	0.07	0.00	−0.01	0.05	0.045
GISS-E2-R-TOMAS-cs	−0.01	−0.04	0.06	0.00	0.00	0.04	0.051
HadGEM2	−0.03	−0.08	0.10	−0.01	−0.03	0.06	0.056
MIROC-CHEM	0.01	0.03	0.06	0.03	0.07	0.08	0.046
NCAR-CAM3.5	−0.04	−0.14	0.14	−0.03	−0.12	0.12	0.033
NCAR-CAM5.1	0.05	0.13	0.18	0.05	0.14	0.18	0.062

lmnb is log-mean normalized bias, lmne is log-mean normalized error. Global mean values are given for AOD where MODIS data is available (values where MISR is available are within 0.001 for sulfate, OA and sea-salt, but can differ substantially for dust).

Table 5. Comparison of regional trends in AOD (550 nm) from ~1980 to ~2000 with AVHRR observations over water.

Model	Europe	Eastern North America	Great Lakes	South and East Asia	Yellow/Eastern Sea
CICERO-OsloCTM2	−0.060	−0.031	−0.041	0.073	0.101
e GFDL-AM3	−0.073	−0.029	−0.055	0.097	0.099
GISS-E2-R-cs	−0.016	−0.004	−0.005	0.035	0.053
HadGEM2	−0.048	−0.013	−0.020	0.037	0.030
LMDzORINCA	−0.040	−0.011	−0.031	0.048	0.065
NCAR-CAM3.5	−0.051	−0.027	−0.037	0.044	0.036
NCAR-CAM5.1	−0.027	−0.013	−0.018	0.012	0.005
7-model average	−0.045	−0.018	−0.030	0.050	0.056
Observations					
NOAA AVHRR	−0.046	−0.025	−0.035	0.038	0.114
GACP AVHRR	−0.062	−0.062	−0.094	−0.029	0.003
NOAA AVHRR*	−0.042	−0.023	−0.047	0.039	0.104
GACP AVHRR*	−0.045	−0.046	−0.053	−0.010	0.009

Regions are defined as Europe (35–70° N; 20–40° E); eastern North America (25-50° N; 100–60° W); the Great Lakes (40–52° N; 76–92° W); South and East Asia (10–30° N; 70–110° E plus 20–40° N; 110–130° E); and the Yellow/Eastern Sea (30–42° N; 118–124° E). The main analysis uses 1981—Feb 1982 and 1984–1986 for the ~1980 AVHRR. The *analysis substitutes 1987 for 1984.

ACPD

12, 21105–21210, 2012

Radiative forcing in the ACCMIP

D. T. Shindell et al.

Title Page

Abstract | Introduction

Conclusions | References

Tables | Figures

◀◀ | ▶▶

◀ | ▶

Back | Close

Full Screen / Esc

Printer-friendly Version

Interactive Discussion

Table 6. Evaluation of 1850 to 2000 RF by component in each model.

Model	SO_4	BCff and bf	OAff and bf	BB	Carb. sum	NO_3	SOA	Aer direct	Aer direct plus missing	Aer AF	O_3
CICERO-OsloCTM2	−0.58	0.38	−0.08	−0.02	0.27	−0.03	−0.07	−0.40	−0.40	–	–
CSIRO-Mk3.6	−0.58	–	–	–	0.32	*n*	*n*	−0.25	−0.42	−1.41	–
GFDL-AM3	–	–	–	–	–	*n*	*n*	−0.41	−0.62	−1.44	0.41
GISS-E2-R	−0.31	0.28	−0.04	0.00	0.24	−0.41	−0.03	−0.49	−0.49	−1.10	0.17
GISS-E2-R-TOMAS	−0.30	–	–	–	–	*n*	*n*	−0.16	−0.37	−0.76	–
HadGEM2	−0.35	0.19	–	–	–	−0.12	*n*	−0.16	−0.33	−1.22	0.23
LMDzORINCA	−0.44	–	–	–	0.16	*n*	*n*	−0.28	−0.50	−0.71	0.35
MIROC-CHEM	−0.39	–	–	–	0.10	−0.35	0.32	−0.12	−0.12	−1.24	0.39
NCAR–CAM3.5	−0.44	0.14	−0.01	0.02	0.15	−0.03	*n*	−0.29	−0.37	*n*	0.44
NCAR-CAM5.1	−0.18	0.20	−0.02	0.01	0.19	*n*	−0.01	−0.06	−0.22	−1.09	–
Mean	−0.40	0.24	−0.04	0.00	0.21	−0.19	0.05	−0.26	−0.39	−1.12	0.33
Std dev	0.13	0.09	0.03	0.02	0.08	0.18	0.18	0.14	0.14	0.27	0.10
Median	−0.39	0.20	−0.03	0.01	0.19	−0.12	−0.02	−0.27	−0.39	−1.16	0.37

Note that HadGEM2 nitrate results are from Bellouin et al. (2011) and are included in the HadGEM2 Aer+ but not the Aer values. MIROC-CHEM nitrate and SOA are included in their Aer values (for this model, a slightly different setup was used for calculations of forcing by individual components, so the total cannot be compared with the sum of individual components). Carb stands for carbonaceous. A – indicates value not available, *n* indicates component not included.

Table 7. Correlation and bias of modeled AAOD with respect to OMI observations.

Model	R vs. OMI global	NMB vs. OMI global	R vs. OMI 90° S to 60° N	NMB vs. OMI 90° S to 60° N
CICERO-OsloCTM2	0.35	−55	0.60	−49
CSIRO-Mk3.6	0.35	−52	0.58	−47
GFDL-AM3	0.31	−29	0.57	−19
GISS-E2-R	0.39	−45	0.63	−41
GISS-E2-R-TOMAS	0.41	−72	0.64	−69
LMDzORINCA	0.31	−33	0.55	−25
MIROC-CHEM	0.31	−85	0.54	−83
NCAR-CAM3.5	0.29	−37	0.50	−28
NCAR-CAM5.1	0.30	−37	0.51	−29
Average 9 models	0.34	−50	0.57	−43

NMB is normalized mean bias (in percent).

Table 8. Direct RF, cloud forcing and AF caused by individual aerosol components and all aerosols in the GISS-E2-R model.

	Direct RF	Cloud forcing	AF
Sulfate	-0.37 ± 0.03	-0.45 ± 0.03	-0.61 ± 0.05
OC	-0.14 ± 0.03	-0.17 ± 0.03	-0.25 ± 0.05
BC	0.24 ± 0.03	0.23 ± 0.03	0.46 ± 0.04
Aerosols	-0.49 ± 0.03	-1.13 ± 0.03	-1.10 ± 0.05

Table 9. Emissions, burden and lifetime for sulfate and BC.

	SO_4 removal $Tg\,yr^{-1}$	BC emissions $Tg\,yr^{-1}$	SO_4 burden Tg	BC burden Tg	SO_4 lifetime days	BC lifetime days
1850						
CICERO-OsloCTM2	61	3.1	1.4	0.07	8.6	8.0
GFDL-AM3	35	3.1	0.7	0.05	7.4	6.2
GISS-E2-R	74	4.0	0.7	0.05	3.5	5.0
GISS-E2-R-TOMAS	81	3.1	1.3	0.07	5.9	8.0
HadGEM2	60	3.1	0.6	0.10	3.8	12.3
MIROC-CHEM	62	3.1	1.1	0.04	6.4	4.4
NCAR-CAM3.5	58	3.1	0.6	0.05	3.7	5.9
NCAR-CAM5.1		3.1		0.03		4.0
Average	61	3.2	0.9	0.06	5.6	6.8
Std dev	13	0.4	0.3	0.02	2.0	2.7
2000						
CICERO-OsloCTM2	132	7.8	2.8	0.17	7.6	7.9
GFDL-AM3	104	7.7	2.3	0.13	7.9	6.2
GISS-E2-R	153	8.8	1.3	0.14	3.0	5.7
GISS-E2-R-TOMAS	167	7.8	2.4	0.17	5.2	8.3
HadGEM2	164	7.7	1.5	0.32	3.4	15.2
MIROC-CHEM	198	7.8	2.2	0.11	4.1	5.2
NCAR-CAM3.5	163	7.7	1.7	0.13	3.9	5.9
NCAR-CAM5.1		7.8		0.08		3.9
Average	155	7.9	2.0	0.16	5.0	7.4
Std dev	27	0.4	0.5	0.07	2.0	3.4
2000–1850						
CICERO-OsloCTM2	71	4.7	1.3	0.10	−0.9	−0.1
GFDL-AM3	69	4.7	1.5	0.08	0.5	−0.1
GISS-E2-R	80	4.8	0.5	0.08	−0.5	0.7
GISS-E2-R-TOMAS	85	5.7	1.1	0.13	−0.7	0.4
HadGEM2	104	4.6	0.9	0.16	−0.5	0.3
MIROC-CHEM	136	4.7	1.1	0.07	-2.3	0.8
NCAR-CAM3.5	105	4.7	1.1	0.08	0.2	0.0
NCAR-CAM5.1		4.7		0.05		−0.1
2000–1850 mean total	93	4.8	1.1	0.09	−0.6	0.2
std dev total	24	0.4	0.3	0.04	0.9	0.4
2000–1850 mean % change	157	152	130	165	−10	4
std dev % change	46	17	56	21	14	8

Radiative forcing in the ACCMIP

D. T. Shindell et al.

Title Page

Abstract | Introduction

Conclusions | References

Tables | Figures

◄◄ | ►►

◄ | ►

Back | Close

Full Screen / Esc

Printer-friendly Version

Interactive Discussion

Table 10. Global mean annual average anthropogenic composition forcings and uncertainties.

	WMGHG RF	Ozone RF	Aerosol AF	Net
1930	0.58 ± 0.06	0.09 ± 0.05	−0.23 ± 0.09	0.44 ± 0.12
1980	1.56 ± 0.16	0.30 ± 0.18	−0.86 ± 0.35	1.00 ± 0.42
2000	2.30 ± 0.23	0.33 ± 0.23	-1.12 ± 0.45	1.51 ± 0.55
2030 RCP 8.5	3.64 ± 0.36	0.43 ± 0.20	−0.87 ± 0.35	3.20 ± 0.54
2100 RCP 2.6	2.83 ± 0.28	0.14 ± 0.17	−0.11 ± 0.10*	2.86 ± 0.34
2100 RCP 4.5	4.33 ± 0.43	0.23 ± 0.12	−0.11 ± 0.10*	4.44 ± 0.48
2100 RCP 6.0	5.60 ± 0.56	0.25 ± 0.12	−0.11 ± 0.10*	5.74 ± 0.61
2100 RCP 8.5	8.27 ± 0.83	0.55 ± 0.30	−0.11 ± 0.05	8.71 ± 0.88

All values are relative to 1850. Uncertainties are 5-95 % confidence intervals, assigned as 10 % for WMGHG RF (Forster et al., 2007), as 1.65 times the standard deviation across models for ozone RF, and as 40 % for aerosol AF, which is 1.65 times the year 2000 standard deviation. *For 2100 AF, calculated AF under RCP8.5 was used for all scenarios, with uncertainty doubled for other scenarios to account for potential differences relative to RCP 8.5.

Discussion Paper | Discussion Paper | Discussion Paper | Discussion Paper | Discussion Paper

ACPD

12, 21105–21210, 2012

Radiative forcing in the ACCMIP

D. T. Shindell et al.

Title Page	
Abstract	Introduction
Conclusions	References
Tables	Figures
I◄	►I
◄	►
Back	Close

Full Screen / Esc

Printer-friendly Version

Interactive Discussion

Table 11. Radiative forcing and climate response for 2000 versus 1850 from ACCMIP and CMIP5 simulations.

Forcing andResponse	Region or Forcing	CSIRO-Mk3.6	GISS-E2-R	GFDL-AM3	HadGEM2	LMD/IPSL-CM5A-LR	MIROC-CHEM
dT(WMGHGs)	Global	1.19	1.13	1.88	1.56	1.72	1.40
	Land	1.52	1.59	2.58	2.11	2.21	1.75
	Sea	1.05	0.94	1.60	1.34	1.52	1.25
dT(ANWF)	Global	−0.75	−0.28	−1.47	−0.97	−0.55	−0.74
	Land	−0.95	−0.49	−2.09	−1.35	−0.73	−0.91
	Sea	−0.66	−0.19	−1.22	−0.82	−0.48	−0.67
WMGHG RF	Global	2.30	2.30	2.30	2.30	2.30	2.30
	Land	2.16	2.16	2.16	2.16	2.16	2.16
	Sea	2.35	2.35	2.35	2.35	2.35	2.35
Aerosol AF + O_3 RF	Global	−1.10	−0.92	−1.04	−1.00	−0.36	−0.85
	Land	−0.71	−1.02	−1.62	−0.89	−0.46	−1.00
	Sea	−1.26	−0.88	−0.80	−1.04	−0.32	−0.79
dT(WMGHG)/ (WMGHG RF)	Global	0.52	0.49	0.82	0.68	0.75	0.61
	Land	0.70	0.74	1.19	0.97	1.02	0.81
	Sea	0.45	0.40	0.68	0.57	0.65	0.53
dT(ANWF)/ (aerosol AF+O_3 RF)	Global	0.68	0.30	1.42	0.97	1.52	0.87
	Land	1.34	0.48	1.29	1.51	1.58	0.91
	Sea	0.52	0.22	1.52	0.79	1.49	0.85
ECS (C per W m^{-2}) NH/SH dT ratio	Global	4.08	2.40	3.97	4.59	4.13	4.67
	WMGHG	1.10	1.67	1.88	1.66	1.61	1.25
	ANWF	1.22	1.84	2.15	1.81	2.07	1.50

dT values are changes in surface air temperature. ANWF refers to anthropogenic non-WMGHG forcing and is the difference between simulations driven by all forcing and the sum of the response to WMGHG and natural forcings (this residual roughly represents the response to aerosols, ozone and land-use forcings). WMGHG forcing is assumed to be 2.30 W m^{-2} in all models.
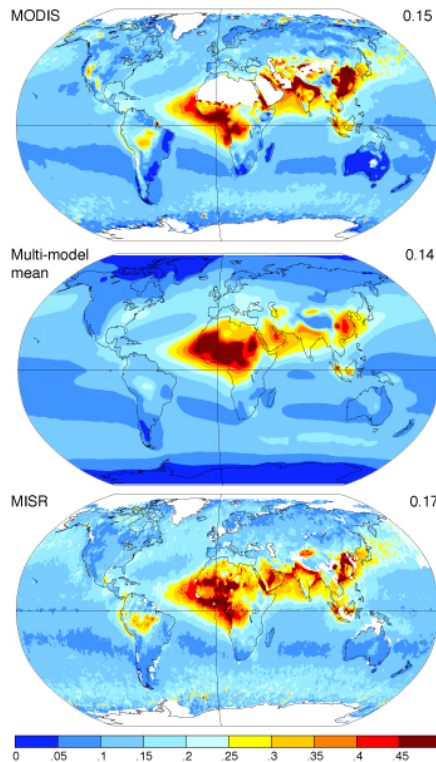
Fig. 1. Annual average aerosol optical depth (550 nm) seen by the MODIS (top) and MISR (bottom) instruments and the ACCMIP multi-model mean (10 models) for the simulations of conditions representative of ~2000 (center). Global mean values are given in the upper right corner of each map. White indicates no data in the satellite measurements.

Printer-friendly Version

Interactive Discussion

Fig. 2. Global mean area-weighted annual average AOD (550 nm) seen by the MODIS and MISR instruments and in the indicated models sampling where MODIS and MISR provide observations. Solid bars show model total AOD values while light shaded areas show the multi-model mean contribution from nitrate or nitrate and SOA in those models that do not include those species.
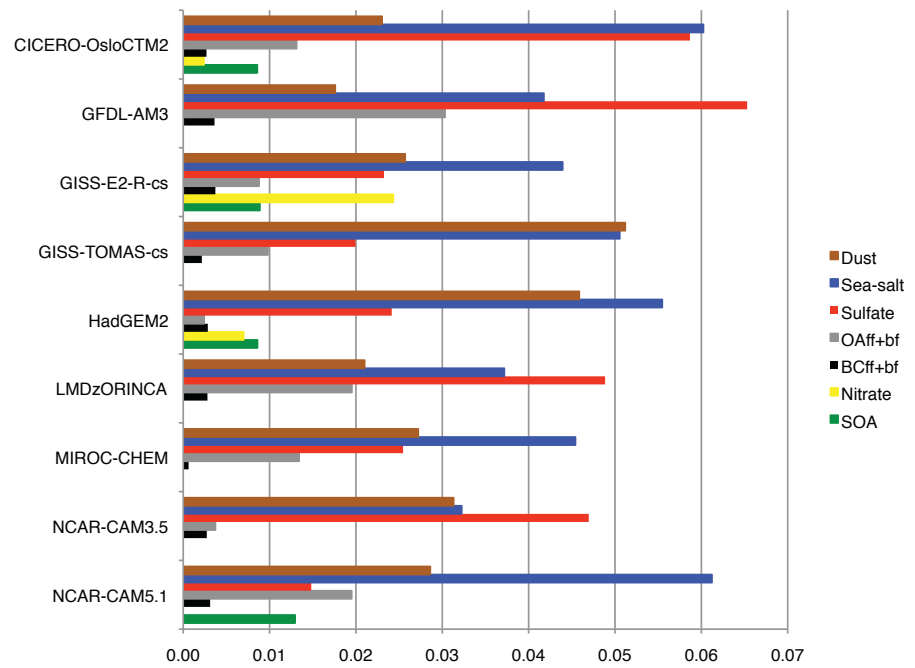
Fig. 3. Global mean annual average AOD (550 nm) by component. Additional AOD of 0.06 is classified as aerosol water in CAM5.1. Clear-sky AOD is used for the GISS-E2-R model.
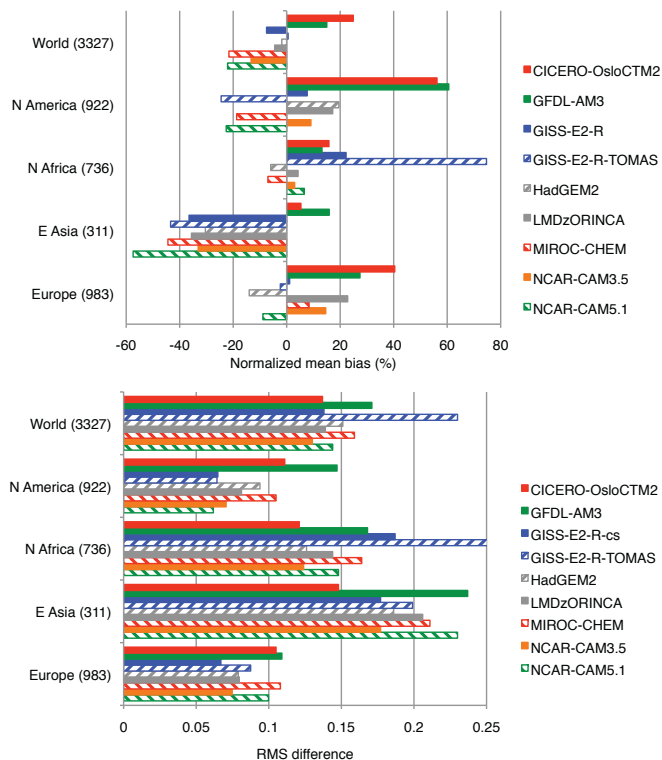
Fig. 4. Regional normalized mean biases (%; top) and root-mean-square differences (bottom) in AOD compared with AeroNet. The value in parentheses after each region's name is the number of valid monthly observations within the region. The GISS-E2-R-TOMAS RMS value for North Africa goes off the scale to 0.41.
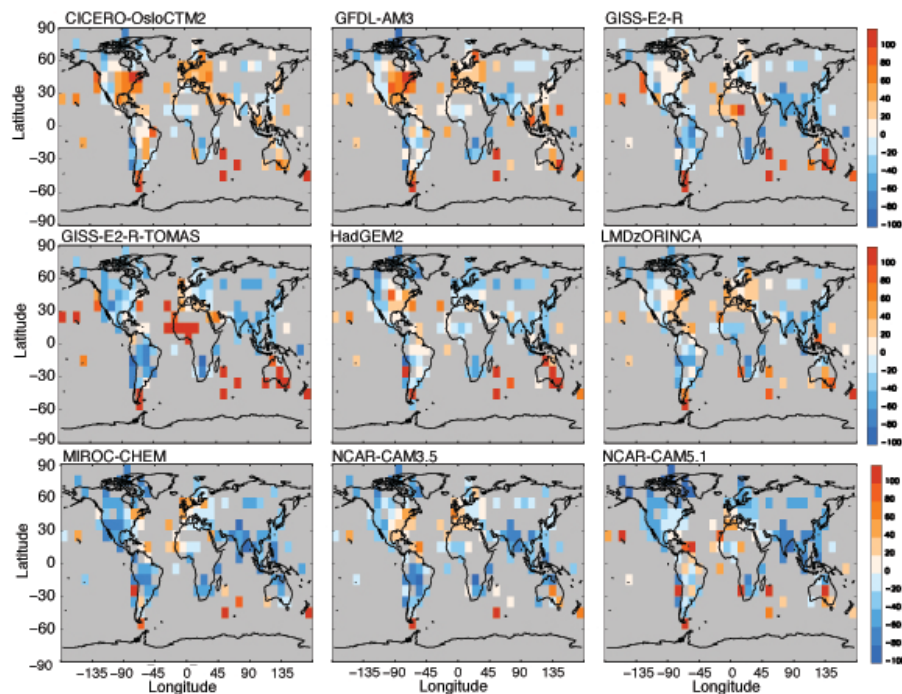
Fig. 5. Bias (%) in models for present-day annual average AOD relative to AeroNet for locations with AeroNet observations. Clear-sky AOD is used for the GISS-E2-R model.
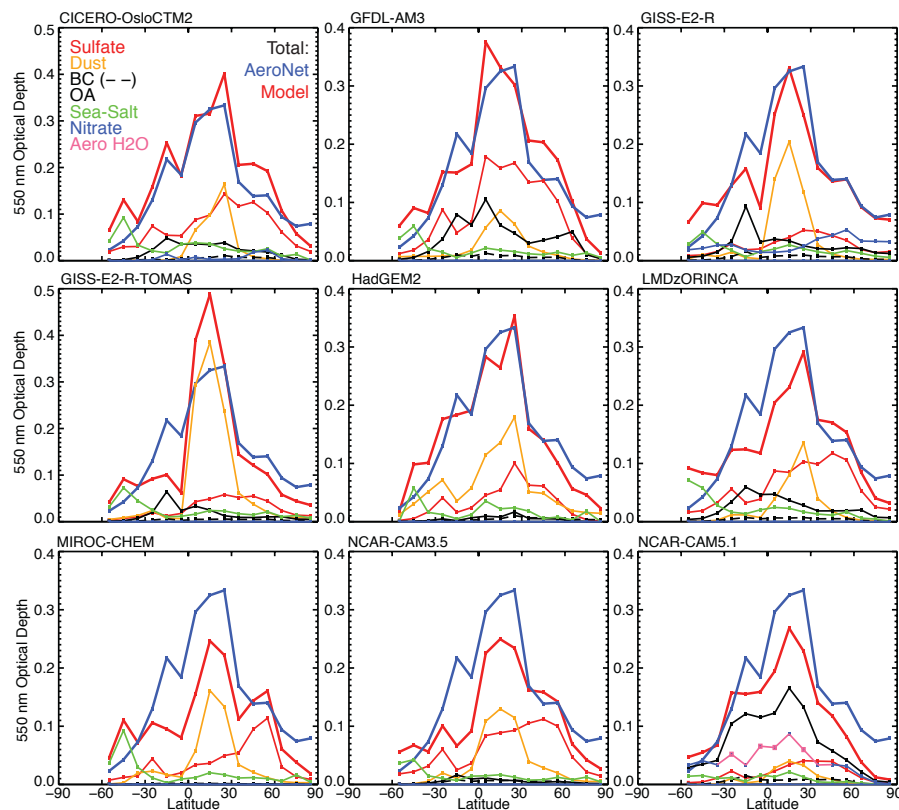
Fig. 6. Zonal mean annual average total AOD in AeroNet observations and models along with AOD by aerosol component. Aero H2O is aerosol water in NCAR-CAM5.1. Clear-sky AOD is used for the GISS-E2-R model.

Full Screen / Esc

Printer-friendly Version

Interactive Discussion
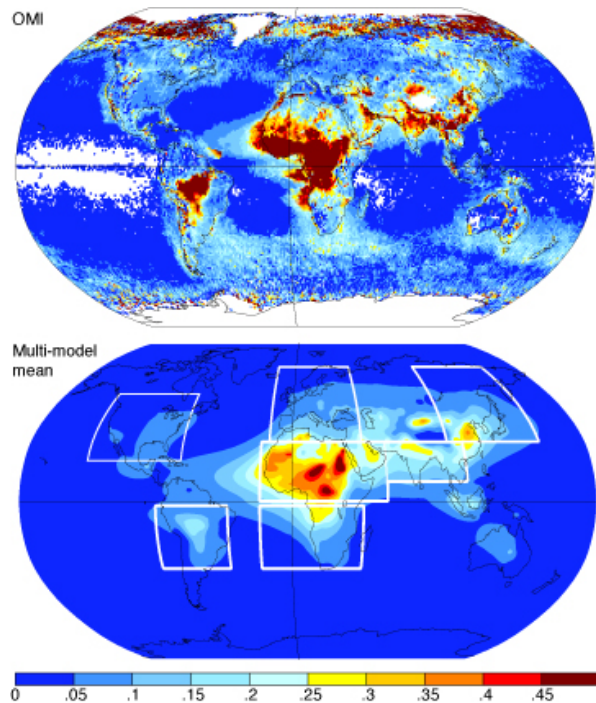
Fig. 7. Annual average AAOD in measurements from the OMI instrument (top) and in the ACCMIP multi-model mean (bottom). The multi-model mean is from 9 models, with HadGEM2 excluded. OMI retrieval is based on OMAERUVd.003 daily products from 2005–2007 that were obtained through and averaged using GIOVANNI (Acker and Leptoukh, 2007). White indicates no data in the satellite record. White borders in the lower panel show areas included in regional AAOD analyses.
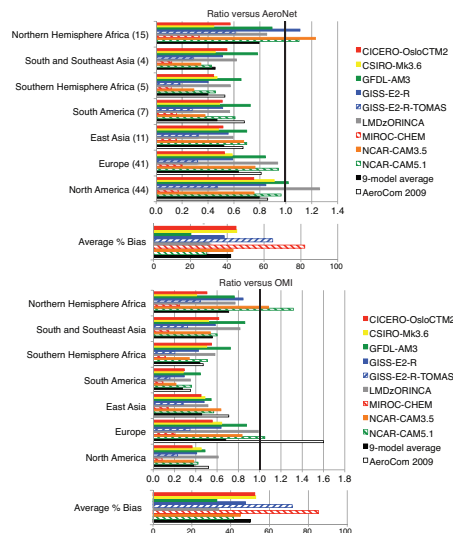
Fig. 8. Ratio of regional average model to retrieved AERONET (top) and OMI land-area (bottom) clear-sky AAOD at 550 nm for the ACCMIP models. Number of measurement sites is given for AERONET for each region. The AERONET data are for 1996–2006, v2 level 2, annual averages for each year were used if more than eight months were present, and monthly averages for more than 10 days of measurements. The values at 550 nm were determined using the 0.44 and 0.87 µm Angstrom parameters. Regions are shown in Fig. 7 and are defined as North America (130° W to 70° W; 20° N to 55° N), Europe (15° W to 45° E; 30° N to 70° N), East Asia (100° E to 160° E; 30° N to 70° N), South America (85° W to 40° W; 34° S to 2° S), Southern Hemisphere Africa (20° W to 45° E; 34S to 2° S), South and Southeast Asia (60° E to 110° E; 10° N to 30° N) and Northern Hemisphere Africa (20° W to 60° E; 0 to 30° N; which includes the Arabian Peninsula). Also shown are the average of 14 AeroCom models from the analysis of Koch et al., 2009 (except for NH Africa and S/SE Asia, which were not calculated for AeroCom). Average % biases shown at the bottom of each analysis are average absolute values over the 7 regions for a given ACCMIP model.
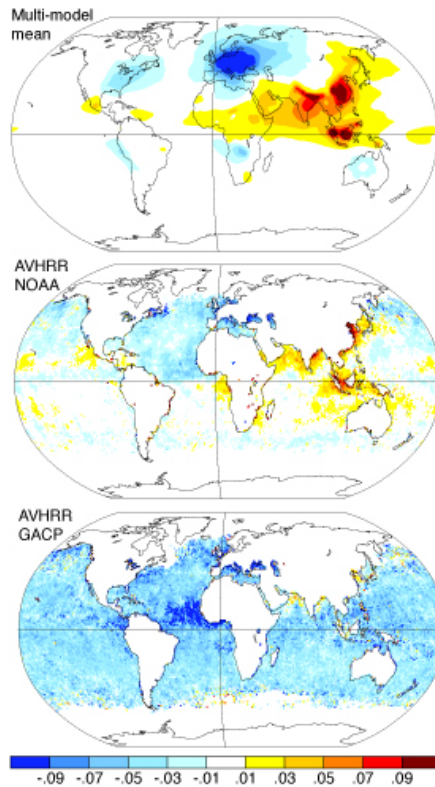
Fig. 9. Modeled and observed annual average AOD trends from ~1980 to ~2000. The multi-model mean (top) compares the 2000 and 1980 timeslice simulations. Observations are based on AVHRR data and show the difference between the 1997–2003 and 1981–1985 averages based on the NOAA product (center) and the GACP product (bottom).
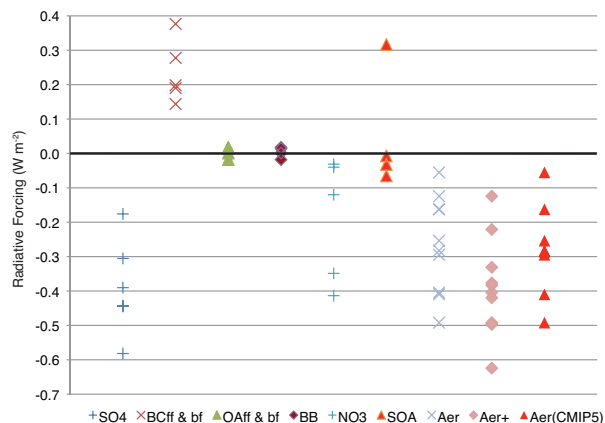
Fig. 10. Global mean aerosol RF (direct) by component and total. Individual points are from different models. Aer are totals. Aer+ are totals including adjustment by adding in forcing due to missing nitrate and SOA (see text). Aer(CMIP5) is the subset of ACCMIP models that also participated in CMIP5. The number of models for each component is: sulfate 9, BCff + bf 5, OAff+bf 4, BB 4, nitrate 5, SOA 4, Aer 10, Aer+ 10, and Aer(CMIP5) 8. Note that HadGEM2 nitrate (Bellouin et al., 2011) and NCAR-CAM3.5 nitrate are included in those models' Aer+ but not the Aer or Aer(CMIP) values. MIROC-CHEM nitrate and SOA are included in their Aer and Aer+ values, but not in their Aer(CMIP) values.
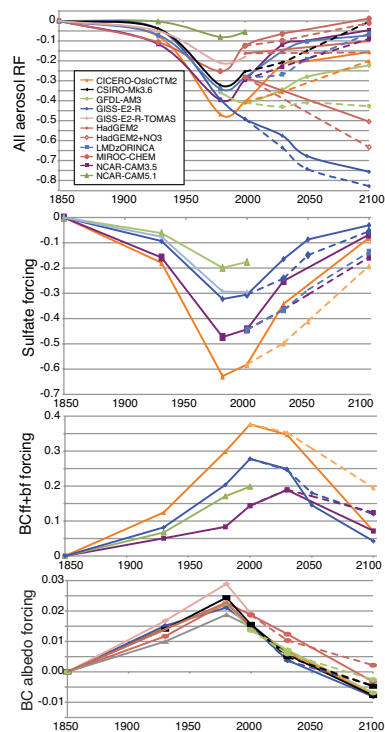
Fig. 11. Timeseries of global mean annual average RF from all aerosols (top), sulfate (2nd row), fossil+bio fuel BC (third row) and BC albedo (bottom) in the indicated models for the indicated times. Symbols are shown for years when RF was calculated. Open symbols for HadGEM2 show the results incorporating nitrate aerosols as described in Bellouin et al. (2011). RCP8.5 is shown as dashed lines, RCP2.6 as solid lines.

Full Screen / Esc

Printer-friendly Version

Interactive Discussion
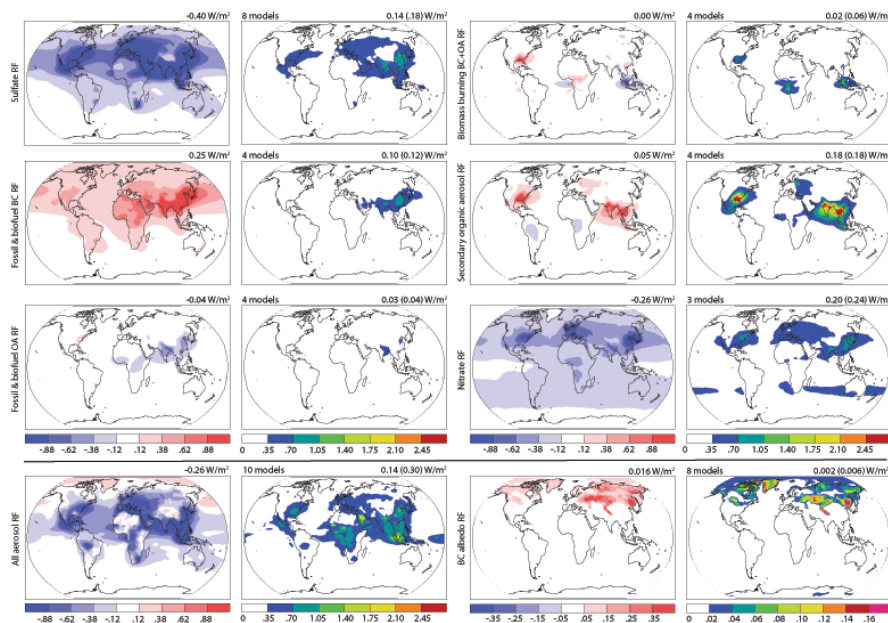
Fig. 12. Spatial pattern of ACCMIP models preindustrial to present-day forcings (W m^{-2}), mean values (left columns) and standard deviation (right columns) for each aerosol component (top three rows), for all aerosol RF (lower left) and BC albedo RF (lower right; note change in scale). Values in the upper right corner give the global means, with standard deviation of the global mean values from each model given first followed by the global mean of the standard deviation at each point.
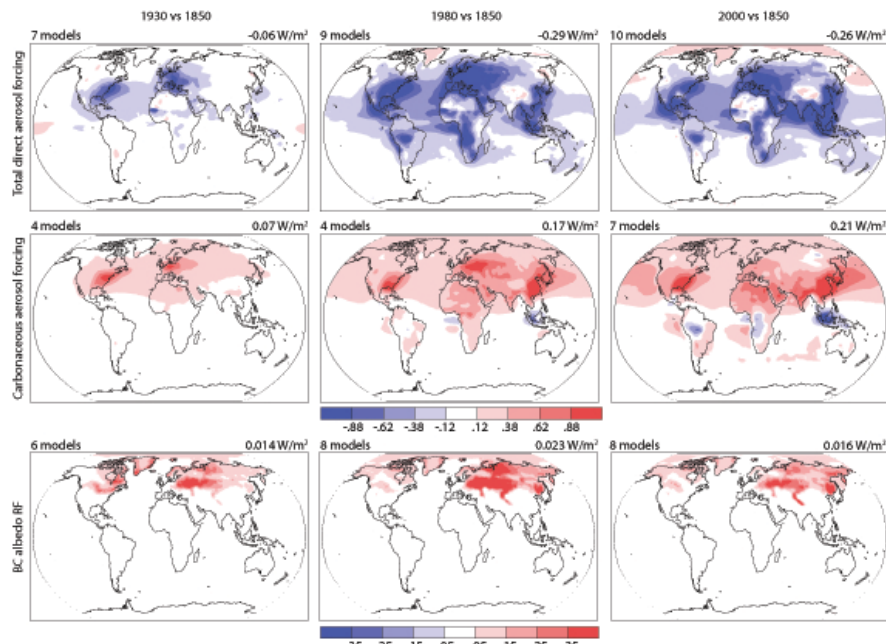
Fig. 13. Multi-model mean all aerosol RF, carbonaceous aerosol RF and BC albedo RF for 1930, 1980 and 2000 (all relative to 1850; $W\,m^{-2}$). The mean 2000 carbonaceous forcing in the 4 models with results at earlier times is also $0.21\,W\,m^{-2}$. Mean total 2000 direct forcing in the 7 models with results for 1930 and in the 9 models with results for 1980 is also $-0.26\,W\,m^{-2}$.

All aerosol RF

Fossil+biofuel BC RF

-.88 -.62 -.38 -.12 .12 .38 .62 .88
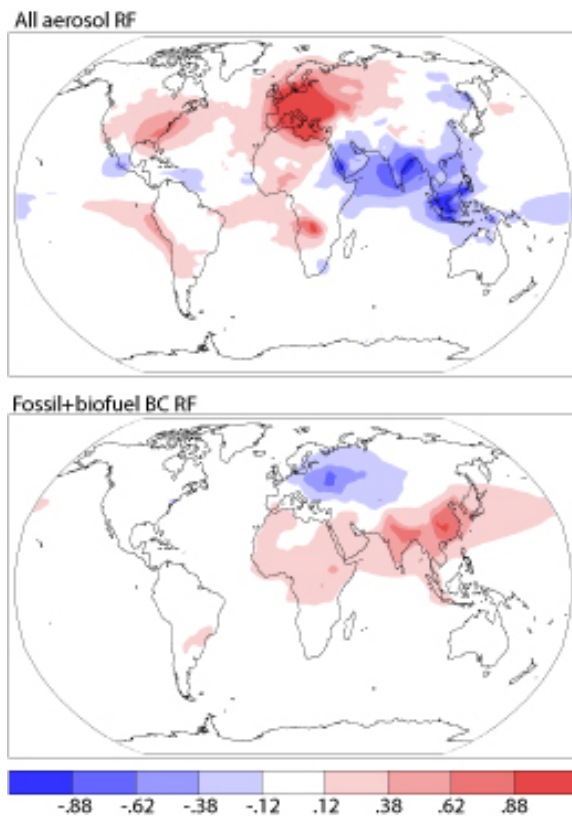
Fig. 14. Multi-model mean difference in all aerosol RF and in fossil + biofuel BC RF between 2000 and 1980 for models with results available at both times (W m^{-2}).
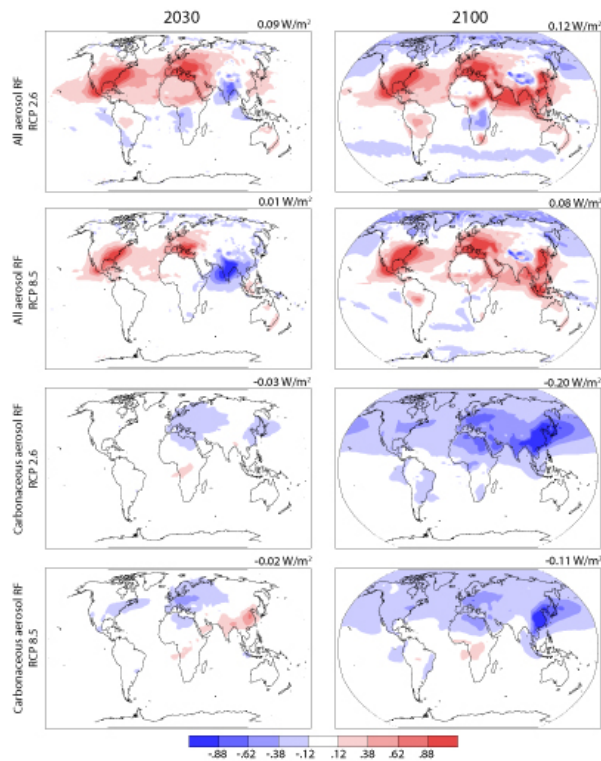
Fig. 15. All aerosol RF and carbonaceous aerosol RF for 2030 and 2100 relative to 2000 under RCP 2.6 and RCP 8.5 ($W\,m^{-2}$).
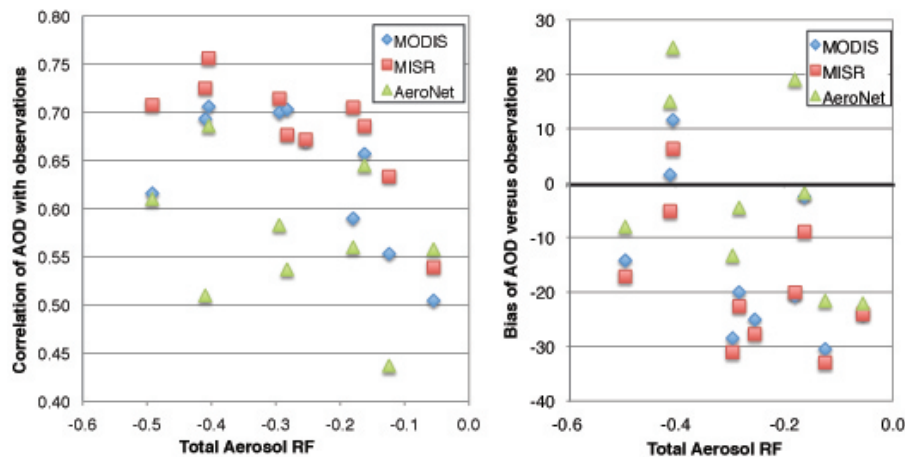
Fig. 16. Comparison of model skill in capturing the spatial pattern (left) or magnitude (right) of annual average AOD observations with modeled RF due to all aerosols.
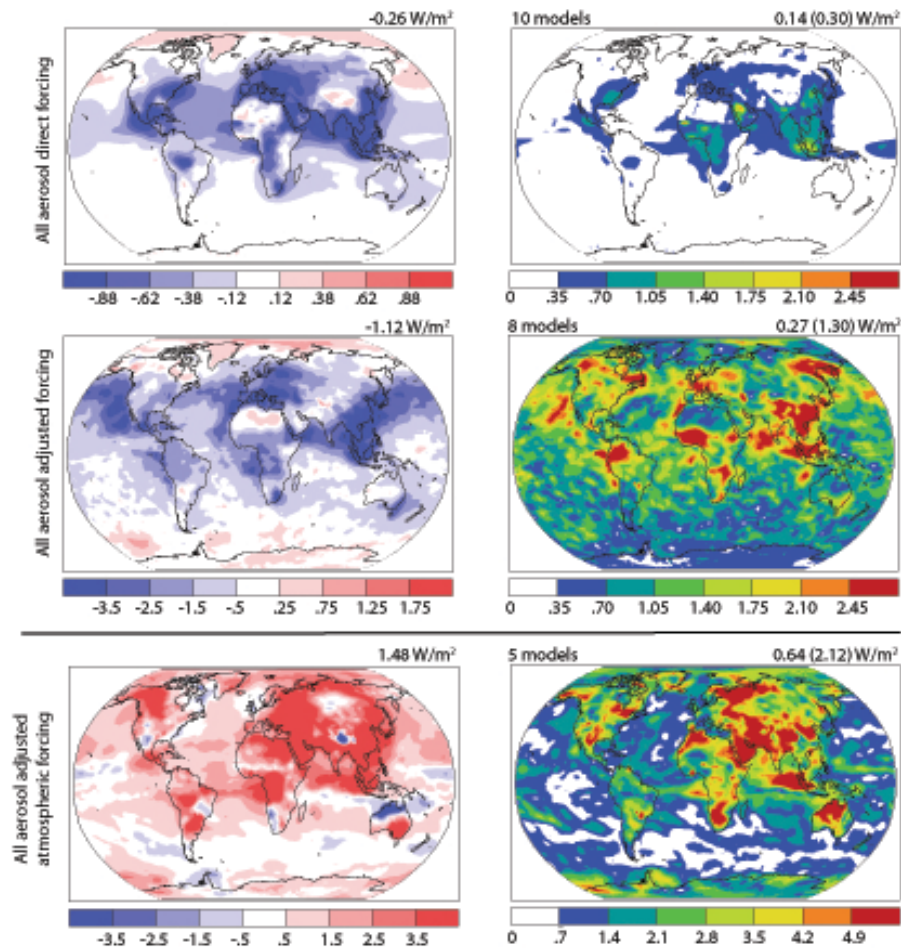
Fig. 17. Direct aerosol RF, aerosol AF, and atmospheric forcing (all in W m^{-2}).

Title Page

Abstract | Introduction

Conclusions | References

Tables | Figures

◄◄ | ►►

◄ | ►

Back | Close

Full Screen / Esc

Printer-friendly Version

Interactive Discussion
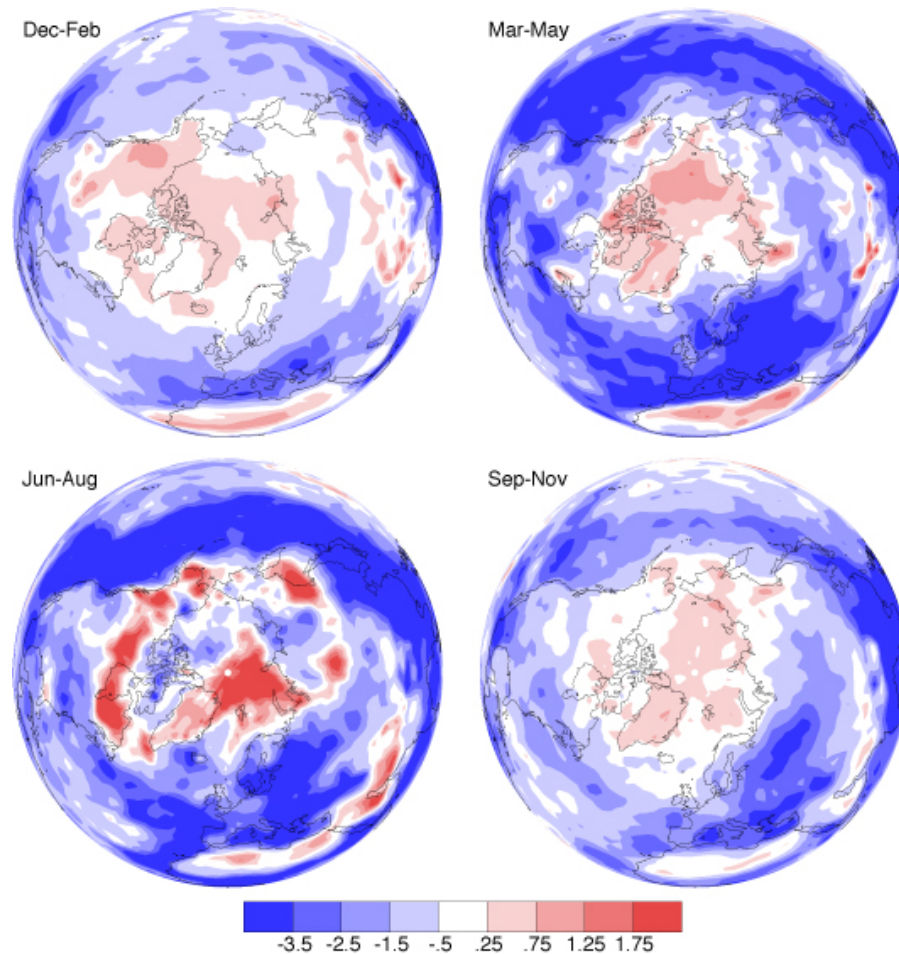
Fig. 18. Multi-model mean Northern Hemisphere aerosol AF for 2000 relative to 1850 for the indicated seasons (W m^{-2}).

Full Screen / Esc

Printer-friendly Version

Interactive Discussion
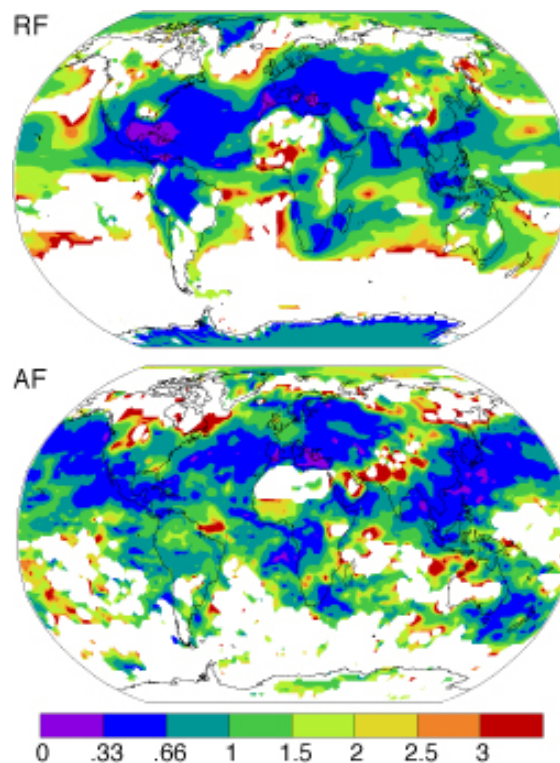
Fig. 19. The ratio of the standard deviation to the mean value for RF and AF. Absolute values of the 1850 to 2000 forcings are used in these ratios. Areas with forcing less than 1/4 of the global mean are blank to avoid division by small values. Both analyses use the same 8 models.
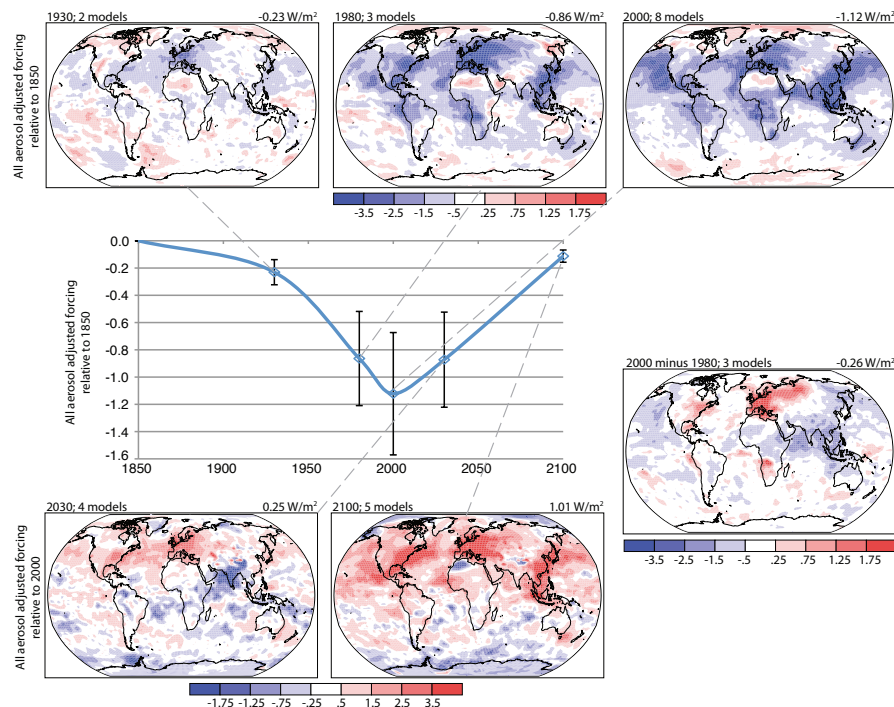
Fig. 20. Spatial patterns of all aerosol AF for 1930, 1980 and 2000 relative to 1850, for 2030 and 2100 under RCP 8.5 relative to 2000 and for 2000 relative to 1980 (W m^{-2}). The timeseries shows global mean values all relative to 1850. All AF values are based on fractional changes relative to 2000 in models with data available at both times, and uncertainty is assigned as the relative uncertainty at 2000 (1.65 standard deviation as 5–95 % confidence interval).
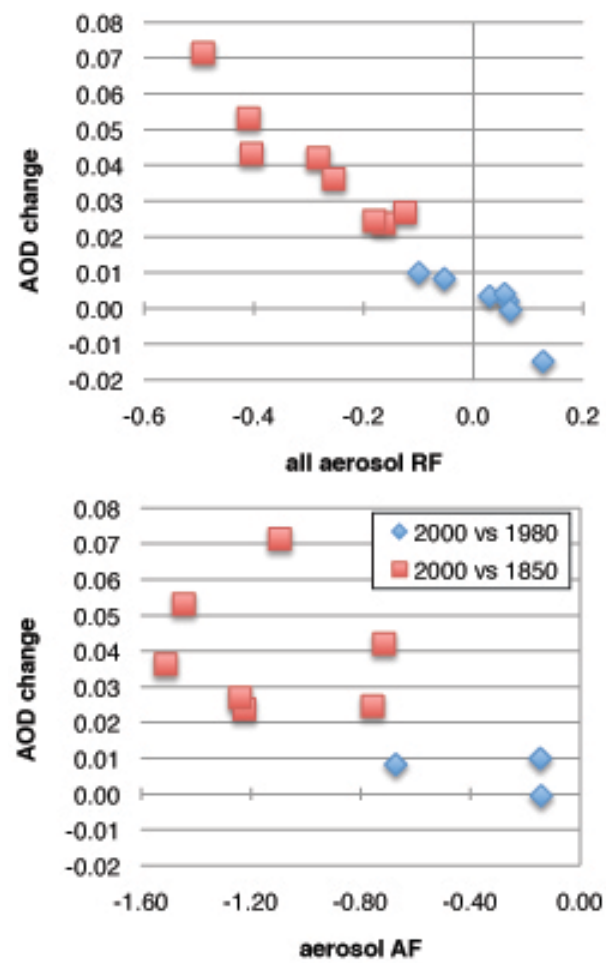
Fig. 21. AOD versus RF (top) and AOD vs AF (bottom) from individual ACCMIP models for the indicated periods.

Title Page

Abstract | Introduction

Conclusions | References

Tables | Figures

◄ | ►►

◄ | ►

Back | Close

Full Screen / Esc

Printer-friendly Version

Interactive Discussion
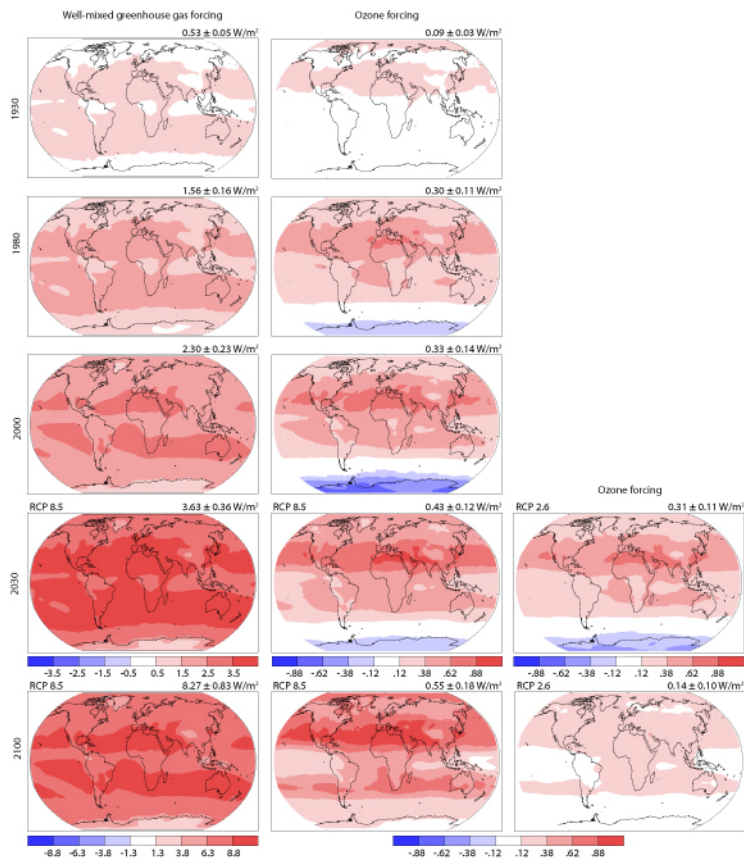
Fig. 22. Maps of WMGHG and ozone RF $(W m^{-2})$ for various historical and future times/scenarios. Note change in scale for WMGHGs in 2100.

Radiative forcing in the ACCMIP

D. T. Shindell et al.

Title Page

Abstract	Introduction
Conclusions	References
Tables	Figures

| I◀ | ▶I |
| ◀ | ▶ |

| Back | Close |

Full Screen / Esc

Printer-friendly Version

Interactive Discussion
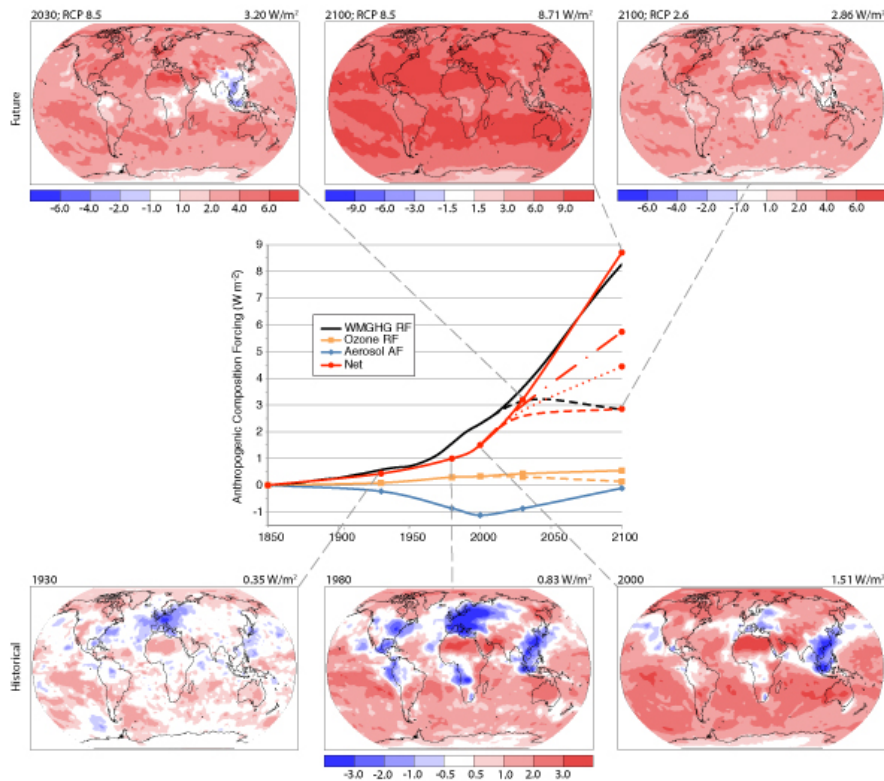
Fig. 23. Maps of total anthropogenic composition forcing and timeseries of global mean by component (W m^{-2}). Top row: maps of 2030 and 2100; bottom row: maps of 1930, 1980 and 2000 (note change in scale relative to top row); center panel: timeseries of global mean forcing with symbols indicating the times at which ACCMIP simulations were performed (solid lines are RCP8.5, dashed lines RCP2.6, dash-dot RCP 6.0, and dotted RCP 4.5). RCPs 2.6, 4.5 and 6.0 net forcings at 2100 are approximate values using aerosol AF projected for RCP8.5. Uncertainty ranges for the global means are given in Table 10.
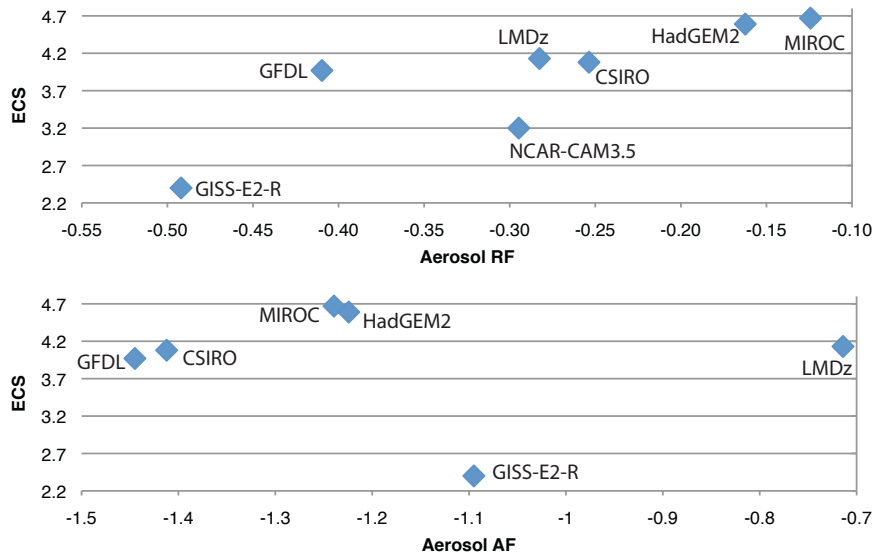
Fig. 24. Relationship between 1850-2000 aerosol forcing and ECS in the indicated AC-CMIP/CMIP5 models.

ACPD

12, 21105–21210, 2012

Radiative forcing in the ACCMIP

D. T. Shindell et al.

Title Page

Abstract | Introduction

Conclusions | References

Tables | Figures

◄ | ►

◄ | ►

Back | Close

Full Screen / Esc

Printer-friendly Version

Interactive Discussion
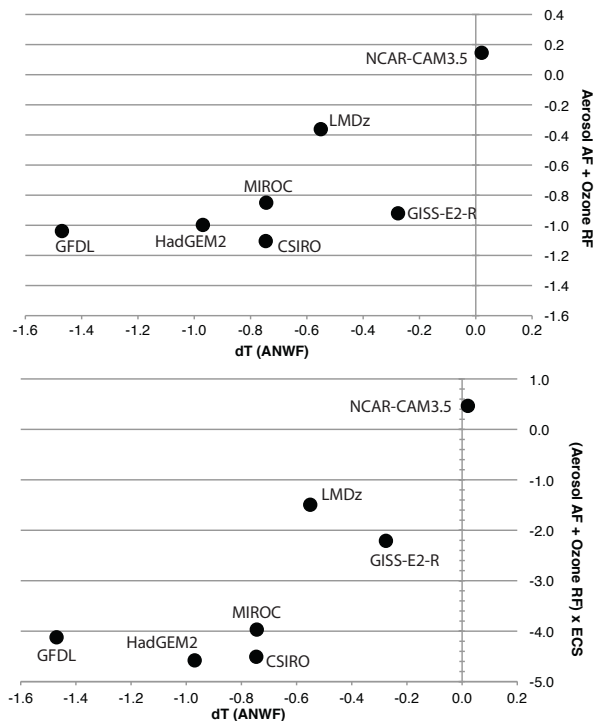
Fig. 25. Global mean surface air temperature change (°C) in CMIP5 20th century historical simulations in response to anthropogenic non-WMGHG forcing (ANWF; calculated as all forcings minus (historical WMGHG + historical natural) forced simulations) versus aerosol AF plus ozone RF (top) and (aerosol AF plus ozone RF) times ECS/3.75 (bottom). Note that aerosol RF is used for NCAR-CAM3.5 as that model did not include indirect aerosol effects.

Title Page

Abstract | Introduction

Conclusions | References

Tables | Figures

◄ | ►I

◄ | ►

Back | Close

Full Screen / Esc

Printer-friendly Version

Interactive Discussion
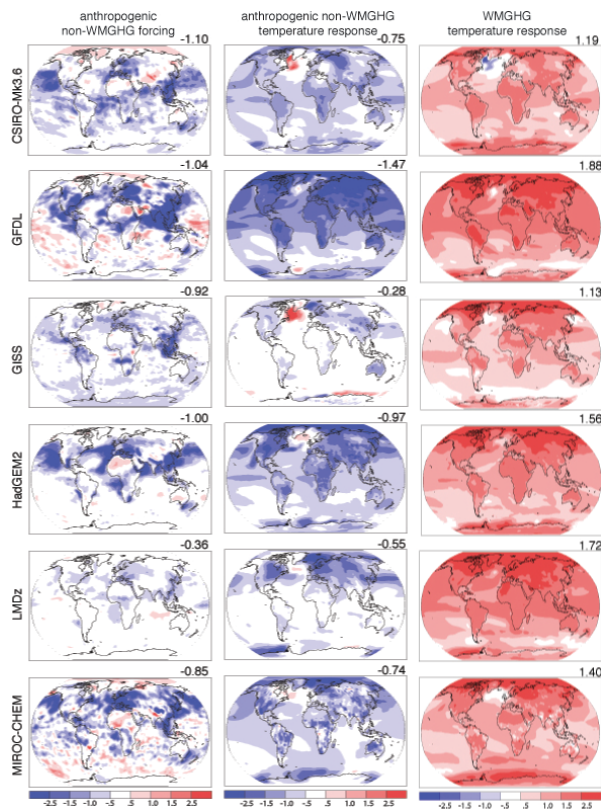
Fig. 26. Spatial distributions of anthropogenic non-WMGHG forcing (left column, W m^{-2}), surface temperature response to anthropogenic non-WMGHG forcing (center column, °C) and surface temperature response to WMGHG forcing (right column, °C). Values are 2000 relative to 1850 with forcing based on ACCMIP analyses and response based on fully coupled transient climate simulations under CMIP5.

Radiative forcing in the ACCMIP

D. T. Shindell et al.

Title Page

Abstract | Introduction

Conclusions | References

Tables | Figures

◀ | ▶

◀ | ▶

Back | Close

Full Screen / Esc

Printer-friendly Version

Interactive Discussion
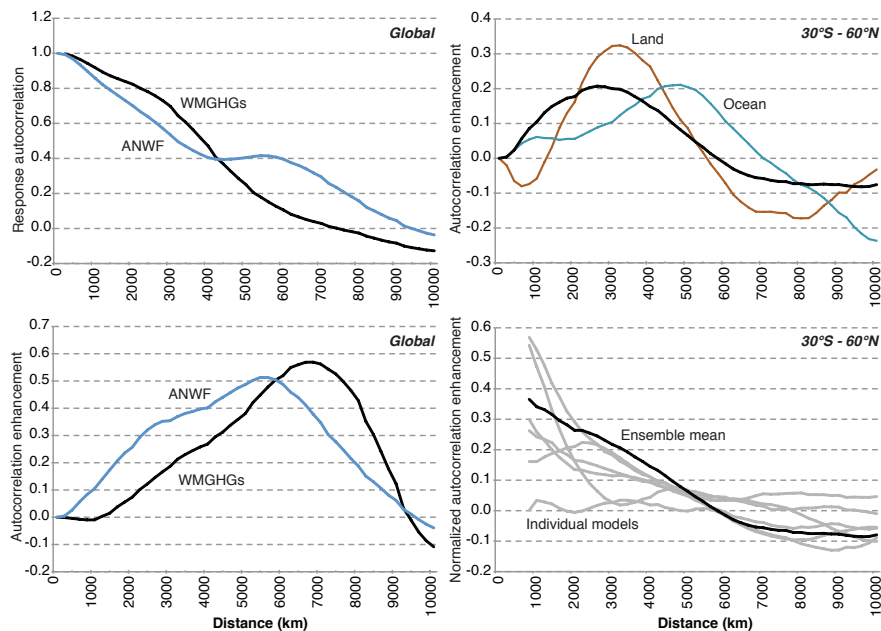
Fig. 27. Analysis of autocorrelations (top left), and of the autocorrelation enhancement in response relative to forcing for WMGHG and ANWF (bottom left), for ANWF from 30° S–60° N (top right), and the autocorrelation enhancement normalized by 1 minus the forcing autocorrelation (bottom right). Values are the mean of the six models used in the forcing/response analysis except for the thin lines in the lower right.
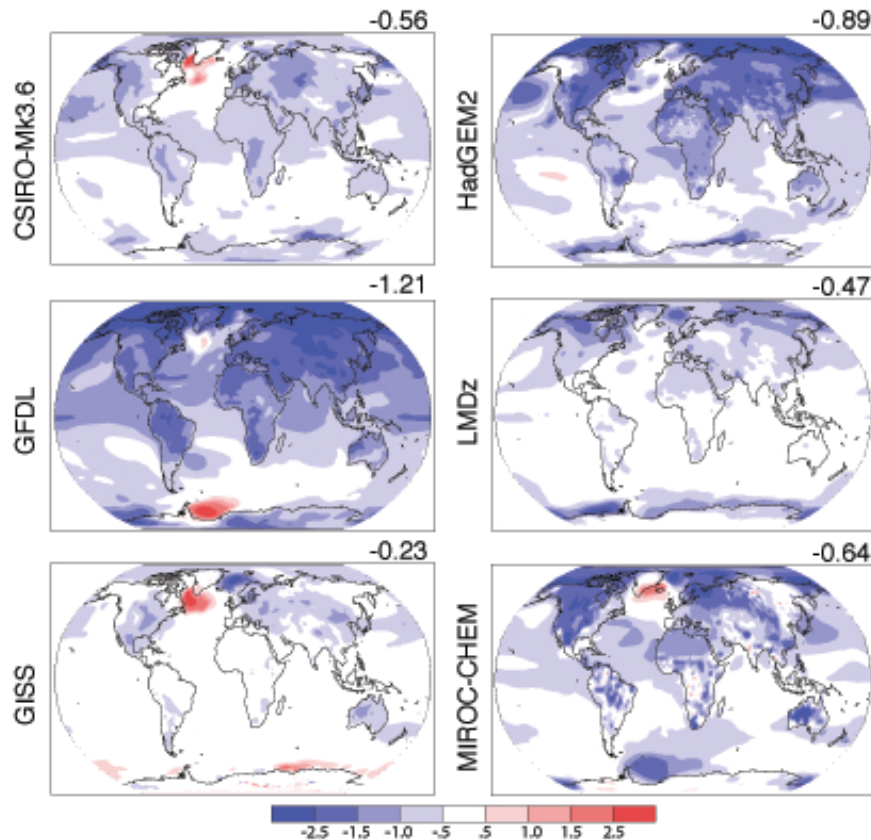
Fig. 28. Spatial distributions of surface temperature response to anthropogenic non-WMGHG forcing (°C) as in Fig. 26 but for 1980 relative to 1850.